

UNIVERSITY OF SPLIT
FACULTY OF ELECTRICAL ENGINEERING, MECHANICAL ENGINEERING
AND NAVAL ARCHITECTURE

Martina Bašić

**DEVELOPMENT OF LAGRANGE METHOD
FOR SIMULATING NON-NEWTONIAN FLOWS**

DOCTORAL DISSERTATION

Split, 2025.

UNIVERSITY OF SPLIT
FACULTY OF ELECTRICAL ENGINEERING, MECHANICAL ENGINEERING
AND NAVAL ARCHITECTURE

Martina Bašić

*Development of Lagrange method
for simulating non-Newtonian flows*

DOCTORAL DISSERTATION

Split, 2025.

The research reported in this thesis was carried out at Department of Mechanical Engineering and Naval Architecture, Faculty of Electrical Engineering, Mechanical Engineering and Naval Architecture, University of Split.

Supervisors: prof. dr. sc. Branko Blagojević, prof. dr. sc. Branko Klarin

Disertation number:

BIBLIOGRAPHIC INFORMATION

Keywords: rheology, non-Newtonian fluids, variable viscosity, Lagrangian flow, meshless method, viscoelasticity, viscoplasticity

Scientific area: Technical sciences

Scientific field: 2.11 Mechanical engineering, 2.15 Basic technical sciences

Scientific branch: 2.11.02 Process energy engineering, 2.15.04 Fluid mechanics

Institution of PhD completion: University of Split, Faculty of Electrical Engineering, Mechanical Engineering and Naval Architecture

Supervisors of the thesis: prof. dr. sc. Branko Blagojević, prof. dr. sc. Branko Klarin

Number of pages: 141

Number of figures: 46

Number of tables: 2

Number of references: 150

Committee for assessment of doctoral dissertation:

1. izv. prof. dr. sc. Igor Peh nec, Faculty of Electrical Engineering, Mechanical Engineering and Naval Architecture, University of Split, Split
2. prof. dr. sc. Hrvoje Kozmar, Faculty of Mechanical Engineering and Naval Architecture, University of Zagreb, Zagreb
3. izv. prof. dr. sc. Ivan Tolj, Faculty of Electrical Engineering, Mechanical Engineering and Naval Architecture, University of Split, Split
4. prof. dr. sc. Chong Peng, Southeast University, Nanjing, China
5. doc. dr. sc. Željko Penga, Faculty of Electrical Engineering, Mechanical Engineering and Naval Architecture, University of Split, Split

Committee for defence of doctoral dissertation:

1. izv. prof. dr. sc. Igor Peh nec, Faculty of Electrical Engineering, Mechanical Engineering and Naval Architecture, University of Split, Split
2. prof. dr. sc. Hrvoje Kozmar, Faculty of Mechanical Engineering and Naval Architecture, University of Zagreb, Zagreb
3. izv. prof. dr. sc. Ivan Tolj, Faculty of Electrical Engineering, Mechanical Engineering and Naval Architecture, University of Split, Split
4. prof. dr. sc. Chong Peng, Southeast University, Nanjing, China
5. doc. dr. sc. Željko Penga, Faculty of Electrical Engineering, Mechanical Engineering and Naval Architecture, University of Split, Split

Dissertation defended on: XX September 2025

Razvoj Lagrangeove metode za simulaciju nenjutnovskih fluida

Sažetak

Ova disertacija predstavlja razvoj nove bezmrežne i Lagrangeove numeričke metodologije, temeljene na metodi Lagrangeove diferencijalne dinamike (LDD), za simulaciju nenjutnovskih fluida. Nenjutnovski fluidi, karakterizirani viskoznošću koja varira s brzinom deformacije, pokazuju složena ponašanja strujanja ključna za širok raspon industrijskih i prirodnih procesa. Točna numerička simulacija ovih strujanja bitna je za projektiranje i optimizaciju procesa. Kao temelj uzeta je LDD metoda, koja koristi Lagrangeov bezmrežni pristup uz prostorne operatore drugog reda točnosti izvedene iz konačnih razlika, te je proširena i primijenjena za modeliranje dinamike nenjutnovskih fluida. Ova metoda nudi prednosti pri rukovanju sa složenim geometrijama, velikim deformacijama i slobodnim površinama, koje su uobičajene u simulacijama nenjutnovskih fluida, zahvaljujući svojoj Lagrangeovoj prirodi i bezmrežnoj diskretizaciji. Formulacija Navier-Stokesovih jednadžbi diskretizirana je pomoću odvajanja jednadžbi tlakova i brzina, gdje se tlak dobiva rješavanjem Poissonove jednadžbe, a brzina se rješava na implicitan način kako bi se prilagodila promjenjivoj viskoznosti svojstvenoj nenjutnovskim fluidima. LDD metoda izbjegava potrebu za računalnom mrežom i koristi konzervativnu Lagrangeovu advekciju. Nadalje, metoda pokazuje točnost drugog reda i nudi robusnu alternativu drugim bezmrežnim metodama poput Smoothed Particle Hydrodynamics (SPH) pružajući točnije polje tlaka i izbjegavajući probleme s vlačnom nestabilnošću. Ova disertacija predstavlja matematičku formulaciju proširene LDD metode za nenjutnovske fluide i validira njezinu točnost i učinkovitost kroz niz referentnih primjera relevantnih za scenarije industrijske obrade polimera i druge primjene, koje uključuju složeno ponašanje fluida. Rezultantna metoda i njena implementacija predstavlja moćan alat za simulaciju različitih fenomena u procesiranju polimera, biomedicinskom inženjerstvu i drugim područjima koja uključuju složenu dinamiku fluida.

Ključne riječi

reologija, ne-Newtonovski fluidi, varijabilna viskoznost, Lagrangeov tok, bezmrežne metode, viskoelastičnost, viskoplastičnost

Development of Lagrange Method for Simulating non-Newtonian Flows

Abstract

This thesis presents the development of a novel meshless and Lagrangian numerical methodology, based on the Lagrangian Differencing Dynamics (LDD) method, for simulating non-Newtonian flows. Non-Newtonian fluids, characterised by their viscosity varying with strain rate, exhibit complex flow behaviours crucial to a wide range of industrial and natural processes. Accurate numerical simulation of these flows is essential for process design and optimisation. The LDD method, a fully Lagrangian and meshless approach utilising second-order consistent spatial operators derived from finite differences, is extended and applied to model non-Newtonian fluid dynamics. This method offers advantages in handling complex geometries, large deformations, and free surfaces, which are common in non-Newtonian flows, by virtue of its Lagrangian nature and mesh-free discretisation. The pressure-velocity formulation of the Navier-Stokes equations is solved using a split-step scheme, where the pressure is obtained by solving a Poisson equation, and the velocity is solved in an implicit manner to accommodate variable viscosities inherent to non-Newtonian fluids. The LDD method avoids the need for a computational mesh and uses a volume-conservative Lagrangian advection. Furthermore, the method demonstrates second-order accuracy and offers a robust alternative to other meshless methods like Smoothed Particle Hydrodynamics (SPH) by providing a more accurate pressure field and avoiding tensile instability issues. The thesis presents the mathematical formulation of the extended LDD method for non-Newtonian flows and validates its accuracy and efficiency through a series of benchmark problems relevant to industrial polymer processing scenarios and other applications involving complex fluid behaviour. Consequently, this work offers a powerful tool for simulating diverse phenomena in polymer processing, biomedical engineering, and other fields involving complex fluid dynamics.

Keywords

rheology, non-Newtonian fluids, variable viscosity, Lagrangian flow, meshless method, viscoelasticity, viscoplasticity

Acknowledgements

I would like to express my deepest gratitude to my mentors and colleagues from the Department for their invaluable support throughout my academic journey. Their guidance, encouragement, and expertise have been essential to my learning and professional growth.

I am also sincerely thankful to my husband and my parents for their unconditional support at home, which enabled me to dedicate myself fully to this endeavor.

This dissertation is dedicated to my children, Zvonimir and Petar. May it serve as a source of inspiration and a reminder that with dedication and hard work, success is always within reach.

Contents

Sažetak	iii
Abstract	iv
List of Tables	ix
List of Figures	xii
Nomenclature	xiii
1 Introduction	1
1.1 Rheology	1
1.1.1 Viscoplasticity	4
1.1.2 Viscoelasticity	5
1.2 Numerical methods	6
1.2.1 Mesh-based methods	6
1.2.2 Meshless Methods	9
1.3 Past research overview	12
1.4 Motivation and open challenges	20
1.4.1 Motivational prior research	21
1.4.2 Complex and large deformations	22
1.4.3 Variability of rheological properties	23
1.4.4 High–Weissenberg number challenges	24
1.4.5 Rationale	25
2 Non-Newtonian fluids	29
2.1 Time-independent fluids	32
2.2 Time-dependent fluids	34
2.3 Viscoelastic fluids	35
2.4 Magnetorheological Fluids	37
2.5 Applications of non-Newtonian rheology	37
2.5.1 Coatings and paints	38
2.5.2 Civil engineering	38
2.5.3 Food processing and personal-care products	39

Contents

2.5.4	Drilling and extraction	39
2.5.5	Additive manufacturing	40
2.5.6	Biological Systems	41
2.5.7	Other applications	41
3	Mathematical modelling	43
3.1	Introduction on modelling	43
3.2	Stresses in the material	45
3.3	Constitutive laws	48
3.3.1	Linear elasticity	48
3.3.2	Equilibrium in general	49
3.3.3	Stress tensor in fluids	50
3.3.4	Equilibrium for fluids	52
3.4	Shear stress in fluids	53
3.5	Dimensionless numbers	57
3.5.1	Reynolds number	57
3.5.2	Deborah number	58
3.5.3	Weissenberg number	58
3.5.4	Bingham number	59
3.6	Navier–Stokes equations	60
3.6.1	Diffusion of constant-viscosity flows	61
3.6.2	Diffusion of variable-viscosity flows	62
3.6.3	Acceleration due to polymeric stress	63
4	Models of non-Newtonian fluids	65
4.1	Material responses	67
4.2	Constitutive equations of linear viscoelasticity	68
4.3	History independent models	70
4.3.1	Bingham model	70
4.3.2	Power Law model	71
4.3.3	Cross Power Law model	71
4.3.4	Bird–Carreau model	72
4.3.5	Herschel–Bulkley model	72
4.3.6	Casson model	72
4.4	History dependent models	73
4.4.1	Linear Maxwell model	73
4.4.2	Oldroyd-B model	76
4.4.3	eXtended Pom-Pom (XPP) model	78

Contents

5	Numerical methodology	79
5.1	The splitting scheme	79
5.1.1	Pressure equation	79
5.1.2	Velocity equation	84
5.1.3	Advection step	85
5.2	Lagrangian differencing	87
5.3	Algorithm overview	89
6	Verification and validation	91
6.1	Viscoplastic fluids	92
6.1.1	Square lid-driven cavity flow	92
6.1.2	Skewed lid-driven cavity flow	94
6.1.3	Dam break of a Bingham fluid	96
6.1.4	Fresh concrete slump test	98
6.1.5	Dam break with elastic gate	99
6.2	Viscoelastic fluids	103
6.2.1	Lid-driven cavity flow	103
6.2.2	Droplet impact	107
6.2.3	4:1 Planar contraction	108
6.2.4	Die swelling	113
7	Conclusions and Future Work	117
7.1	Conclusions	117
7.2	Future work	119
	Bibliography	122

List of Tables

6.1	Dam-break mass-front position determined through numerical and experimental methods at six distinct time instances.	98
6.2	The data of the Abram's slump test.	98

List of Figures

1.1	An example of an unstructured volume mesh prepared for a FVM simulation.	6
1.2	An example of an unstructured volume mesh prepared for a FVM simulation.	7
1.3	A representation of meshless discretization as a point cloud.	9
1.4	Meshless discretization.	10
1.5	Gravitational hopper discharge using spherical particles solved by the DEM.	21
2.1	Non-Newtonian fluid classification and rheological models.	29
2.2	Representation of a non-Newtonian fluid moving around an impeller. Red dots represent the stagnant fluid area around the cavern. The size of the cavern is determined by the impeller type and torque.	30
3.1	Terminology connecting classifications within continuum mechanics and rheology.	44
3.2	Normal stress definition.	45
3.3	Schematic for defining the normal strain in a console.	46
3.4	Shear stress definition.	46
3.5	Infinitesimal stress–element definition in two and three dimensions.	47
3.6	Hooke’s law states that the force F necessary to generate an elongation Δx in a spring with a mechanical constant k	48
3.7	Equilibrium of forces in direction x	51
3.8	An arbitrary fluid volume V enclosed by a surface S that is represented by its normal vectors, \mathbf{n}	52
3.9	Schematic for defining the viscosity, show in a simple shear flow.	53
3.10	The change in fluid element in short period of time defines shear strain.	54
3.11	The viscosity relationship for a Newtonian fluid.	56
4.1	Pipkin diagram.	67
4.2	The Maxwell model that consists of a completely viscous damper and a strictly elastic spring arranged in series.	74
4.3	Stress response to a step strain.	75

List of Figures

5.1	Comparison of the mesh-free (left) vs mesh (right) discretisations of the fluid. The central node i is red, while neighbour nodes $j \in \mathcal{N}$ are blue. For meshless discretisation, the neighbour nodes are in sphere of radius h .	86
5.2	Plot of equation 5.31, showing how distance between points influences interaction contribution. The scale is unimportant, as all interactions are renormalised.	87
6.1	Velocity contour plot and streamlines plotted for the flow of Casson fluid in a square cavity, at $Re = 100$ and $Bn = 0.01$.	93
6.2	The velocity distribution along the horizontal and vertical centerlines of the square lid-driven cavity test.	94
6.3	Velocity contour plot and streamlines plotted for the flow of Power law fluid in a skewed cavity, for $Re = 500$ and $n = 1.5$.	95
6.4	The velocity distribution along the horizontal and vertical centerlines of the skewed lid-driven cavity test.	95
6.5	Dam break snapshots for time instances $t = 0.1, 0.3, 0.6, 1.0$ s, with the plotted velocity magnitude.	96
6.6	Results of dam-breaking front position; comparison of numerical simulations with experimental data.	96
6.7	The evolution of mass front position for simulations with two points counts and time step sizes for the dam break test, compared to the experimental data.	97
6.8	The progression of diameter in the Abram slump test; a comparison of numerical simulations with experimental data.	99
6.9	Simulation snapshots for three time instances $t = 0.5, 5.0, 40.0$ s with plotted velocity magnitudes.	100
6.10	Peer-to-peer coupling with automatic temporal and spatial interpolation, for participant solvers <i>Rhoxyz</i> and <i>CalculiX</i> .	101
6.11	Simulation of a dam break for a rubber gate and water, where the numerical results are compared to the experiment photographs.	103
6.12	Simulation of a dam break for a rubber gate and Power Law fluid with $n = 2$ and $\mu_0 = 10$ Pa-s, where the numerical results show the pressure field and corresponding effective-viscosity field.	104
6.13	Contour plot of the instantaneous velocity magnitude with streamlines (left image) and the trace of the extra-stress tensor (right image), for the lid-driven cavity flow simulation, $Wi = 3$ and $Re = 5 \cdot 10^{-4}$.	105
6.14	The horizontal velocity profile along $x = 0.5$, and vertical velocity profile along $y = 0.75$, for the lid-driven cavity flow simulation, $Wi = 3$ and $Re = 5 \cdot 10^{-4}$.	106

List of Figures

6.15	Evolution of droplet deformation during impact, illustrated with velocity magnitude. The simulation with point spacing $\Delta = 0.4$ mm demonstrates the solver’s ability to replicate viscoelastic effects at coarser point cloud resolutions.	108
6.16	Analysis of the simulated evolution of viscoelastic–droplet diameter upon the impact.	109
6.17	The geometry of the 4:1 planar contraction and the positions of the recirculation vortices are shown. XR is the corner vortex’s reattachment length.	110
6.18	Contour plot of the velocity magnitude and streamlines for the 4:1 planar contraction, for $Wi = 5$ (top image) and $Wi = 10$ (bottom image).	111
6.19	Contours of the principal stress difference (PSD) around the 4:1 planar contraction, simulated for $Wi = 5$	112
6.20	A contour plot illustrating the velocity magnitude (top left image) and the components of the extra-stress tensor for the 4:1 planar contraction simulation, $Wi = 14$ and $Re = 0.01$	113
6.21	Schematic depiction of the computational domain and arrangement of the die-swell experiment.	114
6.22	Images of the free surface from the die-swell simulation, using $Wi = 0.5$ and $Re = 0.5$. The progression of the free-surface (one contour per one simulation second) is juxtaposed with the swell ratio in [1].	115
6.23	Comparison of the evolution of the die swelling, for several Weissenberg numbers ranging from 0.333 to 0.833.	115
6.24	Contour plot of the instantaneous values of the trace of the extra–stress tensor, for the simulated die–swell experiment, using $Wi = 0.5$ and $Re = 0.5$. The points are also plotted to demonstrated convergence of the point–cloud incompressibility.	116

Nomenclature

Latin

\mathbf{a}	an acceleration
\mathbf{a}_{ext}	external acceleration
b	a source term
\mathbf{B}	renormalisation tensor
C_{acc}	coefficient for suppressing velocity divergence, based on particle acceleration
C_{visc}	coefficient for suppressing velocity divergence, based on viscosity
C_{elast}	coefficient for suppressing velocity divergence, based on elasticity component
C_{wall}	coefficient for suppressing velocity divergence at the walls
C_{clean}	coefficient for cleaning divergence of the velocity field
C_{n-1}	BDF2 coefficient for the previous time step, $C_{n-1} = -r_t^2 / (1 + 2r_t)$
C_n	BDF2 coefficient for current time step, $C_n = (1 + r_t)^2 / (1 + 2r_t)$
C_{n+1}	BDF2 coefficient for the time step to be solved, $C_{n+1} = \delta t (1 + r_t) / (1 + 2r_t)$
d	number of dimensions of the flow problem, 2 or 3
d	total derivative
D	Lagrangian derivative
De	Deborah number
E	Young's modulus
\mathbf{E}	symmetrised velocity–gradient tensor
f	general scalar function
F	force
\mathbf{F}_{ext}	external acceleration vector, usually gravitational acceleration

List of Figures

\mathbf{g}	Earth gravity acceleration vector
G	elastic modulus
\mathbf{I}	identity tensor
J	creep compliance
k	spring stiffness
m	regularization parameter
\mathbf{n}	vector of normal direction (at wall, at free surface, etc.)
n	known current time step
$n - 1$	known previous time step
$n + 1$	unknown future time step
S	surface area
p	pressure
Re	Reynolds number
r_t	ratio of the current and previous time-step sizes, $r_t = t_n/t_{n-1}$
t	time instant
tr	trace of the matrix, i.e. sum of diagonal elements
\mathbf{u}	velocity vector
\mathbf{U}	imposed velocity vector (at wall or inlet)
V	a volume
Wi	Weissenberg number
\mathbf{x}	particle position
x	x dimension
y	y dimension
z	z dimension

Greek

$\Delta\alpha$	angle
Δ	initial spacing between neighbours
δx	displacement of fluid volume in the x direction
ε	strain

List of Figures

η	apparent viscosity
λ_1	relaxation time for elasticity, to reach equilibrium state
λ_2	retardation time
μ	dynamic viscosity
μ_s	dynamic viscosity of the solvent part of fluid
μ_p	dynamic viscosity of the polymeric part of fluid
μ_0	fluid dynamic viscosity at zero shear rate
μ_∞	fluid dynamic viscosity at infinite shear rate
ρ	fluid density
$\boldsymbol{\sigma}$	Cauchy stress tensor
σ	a normal stress
$\boldsymbol{\tau}$	a stress tensor
$\boldsymbol{\tau}_s$	diffusion–stress tensor for the solvent fluid
$\boldsymbol{\tau}_p$	extra–stress tensor for the polymer part of the fluid
τ_0	yield shear stress
ν	fluid kinematic viscosity
δt	time–step size
$\dot{\gamma}$	shear rate
\square^\top	transpose operation
∇	gradient operator
$\nabla \cdot$	divergence operator
∇^2	Laplace operator or Laplacian, $\nabla^2 \equiv \Delta$
$\nabla \times$	curl operator
$ \square $	magnitude of a vector
$\overset{\nabla}{\square}$	upper Convected operator

Abbreviations

BEM	Boundary Element Method
BC	Boundary condition
BDF2	Backward differencing formula of the second order
BEM	Boundary Element Method
CFL	Courant–Friederich–Lewy
CFD	Computational Fluid Dynamics
DEM	Discrete Element Method
DEVSS	Discrete elastic-viscous stress splitting
DNS	Direct Numerical Simulation
EVSS	Elastic-viscous-split-stress
FDM	Finite Differences Method
FEM	Finite Element Method
FENE-P	Finitely Extensible Nonlinear Elastic-Peterlin
FIB	Flow Induced Birefringence
FSI	Fluid–Structure Interaction
FVM	Finite Volume Method
FPM	Finite Pointset Method
GNS	Generalized Navier-Stokes
GFDM	Generalized Finite Difference Method
HWNP	High Weissenberg number problem
IB	Immersed Boundary
IBM	Immersed Boundary Method
ISPH	Incompressible Smoothed Particle Hydrodynamics
LDD	Lagrangian Differencing Dynamics

List of Figures

LST	Linear Stability Theory
MHD	Magnetohydrodynamics
ML	Machine Learning
MLS	Moving Least Squares
MPM	Material Point Method
MPS	Moving Particle Semi-Implicit method
NS	Navier-Stokes
NSE	Navier-Stokes Equations
ODE	Ordinary Differential Equation
PDE	Partial Differential Equation
PFEM	Particle Finite Element Method
PSD	Principal Stress Difference
SPH	Smoothed Particle Hydrodynamics
TVP	Thixotropic viscoplastic
UCM	Upper-convected Maxwell
VOF	Volume of Fluid

1 Introduction

1.1 Rheology

Professor Eugene Bingham coined the term “rheology” in 1920, which means the science of material deformation and flow [2]. Since then, rheology has grown into a complex, multidisciplinary, and rapidly expanding research field. It focuses on the movement of matter, including liquids, gases, and soft solids. Soft solids are those that deform plastically when a force is applied to them. The liquid and gas states investigated in this branch of physics differ from other fluids and gases in that they lack a single coefficient of viscosity for a given temperature, i.e. they do not follow Newton’s viscosity experiment law.

Non-Newtonian states are being studied, particularly because they are used in industry. To manipulate fluids and soft solids, they must be evaluated at the microscopic and/or molecular levels to determine the critical properties and mechanisms that these material systems possess. Then, it is needed to examine specific material system applications and provide an answer to industrial services regarding the material system’s rheological behavior in the application. Material systems used in industry are divided into several categories. They are broadly classified into three types: macromolecular systems, multiphase systems, and macromolecular–multiphase systems. These classes include polymer solutions, polymer melts, particle dispersions, emulsions, gels, and glasses. High molecular weight fluids, such as polymer solution, viscoelastic or viscoplastic fluids, and colloidal suspension, exhibit non-Newtonian flow properties, as do the vast majority of biological fluids. Polymer solutions are mixtures of polymer and a solvent, whereas polymer melts are plastics that have been heated to a high temperature and begun to flow. Particle dispersions and emulsions are colloidal solutions in which a solid is distributed in a liquid, or emulsions in which oil is dispersed in water or water in oil, and are primarily two-phase systems. Gels are primarily solid-like materials that are extremely soft. Glasses, unlike soft solid gels, are a hard and rigid type of solid substance. Material systems of interest should be identified in order to determine which specific category they fall into, allowing them to be evaluated and effective models to be used and implemented. Food is an excellent example of how different material classes can be combined. Because it contains polysaccharides, starch, and a wide range of

polymers, as well as emulsions and crystals of specific food ingredients like salt and sugar. Cement is another example of a macromolecular–multiphase system, as good cement slurry now includes polymers to improve performance.

The predominant approach for simulating macroscopic flows is continuum mechanics. The derivation of continuum constitutive equations from kinetic theories requires closure approximations; nevertheless, in most computationally simulated real applications, equations for the constitutive model and material characteristics are derived from rheology data. The application of equations for the constitutive models that result from fitting of curves of rheometric flows (e.g., simple shear or uniaxial extensional) for the description of more complex flows should be undertaken with precaution. Viscoelastic flows, which are defined by the interaction of viscous and elastic effects, are difficult to model numerically due to their complex behavior. Because of the stiff nature of the hyperbolic differential constitutive equations, computational prediction of viscoelasticity is sensitive to numerical instabilities, and physical and nonphysical constitutive instabilities. For more than twenty years, one of the most important challenges in computational rheology has been the difficulty of numerically resolving the constitutive equations, which has been known as the high Weissenberg number problem (HWNP) [3]. The HWNP manifests itself as a lack of simulation stability, which causes numerical values to blow up. Depending on the flow problem, spatial discretization, and numerical method, it is triggered when the Weissenberg number (also known as the Deborah number) reaches a critical value. HWNPs play an important role in viscoelastic flow as they illustrate circumstances in which elastic forces substantially affect fluid behaviour, leading to intricate phenomena such as coil-stretch transitions and elastic instabilities that complicate precise simulation and practical comprehension across multiple technological and scientific applications. Overcoming these challenges at high Weissenberg numbers is critical for predicting and controlling viscoelastic flow behaviours in polymer processing, microfluids, and biomedical settings.

The domain of research dedicated to simulating viscoelastic flows has arrived at a pivotal crossroads, characterised by a synthesis of progress and obstacles. Researchers have achieved significant strides in the development of numerical methods, particularly concentrating on meshless methodologies for simulating the detailed behaviour of viscoelastic materials. The present condition of the area is marked by an increasing acknowledgement of the significance of precise simulations for various applications, encompassing industrial processes such as polymer production and biological systems like blood circulation. The Oldroyd B model continues to be a focus of current constitutive model research. Researchers are eager to investigate its application and integration into numerical simulations, recognizing its ability to accurately capture materials' viscoelastic properties. Even with these improvements, there are still challenges to face.

1 Introduction

Researchers are still looking into computational efficiency, stability, and how well systems can manage complex nonlinear viscoelastic behaviours. Additionally, the field is starting to see the importance of benchmark problems and standard validation procedures for evaluating the accuracy and reliability of different numerical methods. A detailed look at the current state of the research field shows an energetic atmosphere full of knowledge and ongoing studies. By investigating closely at recent publications, researchers can understand the details of meshless methods, how to implement constitutive models, and the main challenges that need teamwork to improve simulations of viscoelastic flows. Therefore, this thesis investigates the need for precise and efficient numerics to capture the complex dynamics of viscoelastic materials in a wide range of applications, from industrial processes to biological systems.

Meshless methods have become more popular for their enhanced capacity to manage complicated shapes and dynamic fluid interactions, making them a viable choice for simulating viscoelastic flows. A prominent meshless Lagrangian method in contemporary literature is the Lagrangian Differencing Dynamics (LDD), which serves as a feasible alternative to conventional mesh-based techniques. The principal objective of this study is to enhance the meshless Lagrangian Differencing Dynamics (LDD) method [4, 5, 6, 7] for simulating viscoelastic flows by integrating the Oldroyd–B constitutive model, thereby facilitating precise and efficient modelling of viscoelastic fluid behaviours. LDD is a numerical technique that integrates Lagrangian and mesh-free methodologies to accurately represent the dynamics of these fluids. In viscoelastic simulations, meshless Lagrangian discretisation provides a unique benefit through its particle-based property tracking, enabling the integration of memory effects. This thesis concentrates on derivative-based viscoelastic models, whereas integral formulations present a feasible alternate approach. The LDD method is devoid of tensile instability issues and can accommodate substantial negative pressures [4], unlike SPH schemes which necessitate numerical and algorithmic interventions [8, 9, 10, 11, 12]. The meshless design facilitates a more precise depiction of complex geometry and dynamic fluid interfaces. This thesis aims to enhance numerical tools by offering a more precise and economical approach to capturing the viscoelastic behaviour of materials. This thesis demonstrates how the suggested method offers a significant advantage by circumventing the constraints of conventional mesh-based approaches. Its meshless Lagrangian characteristic permits a more precise depiction of intricate geometries and dynamic fluid interfaces, while more readily evading HWNP. The significance of this investigation resides in its capacity to enhance simulation accuracy, therefore enabling progress in various domains, including polymer processing, biomedical engineering, and materials research. The method’s relevance to actual polymer fluid behaviour is shown by the effective modelling of benchmarks pertinent to industrial polymer processing contexts. The research tackles current numerical issues, and its noteworthy computa-

tional capability supports the optimisation of industrial processes, the innovation of novel materials, and the examination of biological fluid dynamics.

In order to understand why rheology is extremely complex to be numerically simulated, the following subsections shortly introduce the idea of viscoplasticity and viscoelasticity, while the further sections give details on relevant mathematics and numerics.

1.1.1 Viscoplasticity

Numerous fluids encountered in industrial applications and natural environments exhibit behavior that deviates significantly from Newton's law, which describes fluids with a constant viscosity. These non-Newtonian fluids often display complex flow characteristics. Among them, viscoplastic fluids represent a crucial category, distinguished by the presence of a yield stress. This means they behave like a rigid solid when subjected to stresses below a certain threshold and only begin to flow like a liquid once this yield stress is exceeded.

The Bingham model [2, 13] is a commonly employed and foundational model for describing viscoplastic behavior. Due to its relative mathematical simplicity (as a two-parameter model), it is frequently used in engineering applications across diverse industries such as food processing, drilling, oil and gas, and chemicals. The defining characteristic of a Bingham fluid is its dual nature: depending on the applied stress, it behaves either as a solid or as a viscous liquid. For flow to initiate, the applied shear stress must surpass the fluid's inherent yield stress. Unlike Newtonian fluids, which flow immediately upon the application of any stress (having negligible yield stress), a Bingham fluid will resist initial deformation. This yield behavior is critical in applications like suspending particles in drilling muds, preventing the sag of paints, or modeling the flow of substances like fresh cement, debris flows, avalanches, and lava flows. Examples of materials that can exhibit viscoplastic characteristics include mud, certain paints, some food products like ketchup or mayonnaise (which also show shear-thinning), and concentrated suspensions.

While viscoplasticity is defined by this yield stress, other non-Newtonian fluids exhibit different time-independent behaviors where viscosity changes with shear rate but without a distinct Bingham-like yield point. These are broadly termed purely viscous non-Newtonian fluids, including: shear-thinning fluids (their effective viscosity decreases as the shear rate increases; polymer solutions, biological fluids, mud or mayonnaise) and shear-thickening fluids (their effective viscosity increases as the shear rate increases).

Models like the Power Law [14] provide a generalized framework for describing these shear-dependent viscosities (shear-thinning for flow-behavior index $n < 1$, shear-thickening

for $n > 1$, and Newtonian for $n = 1$). The Casson model [15] is another model often used for shear-thinning materials, particularly those also exhibiting a yield stress distinct from the Bingham idealization. Understanding these varied behaviors is essential for engineers and designers to accurately predict flow in numerous industrial applications.

1.1.2 Viscoelasticity

Numerous synthetic and natural fluids demonstrate complex rheological behaviour, with viscoelasticity being a significant fluid characteristic. The accurate simulation of viscoelastic flows is essential in multiple industrial and biological applications, including fluid dynamics and the study of materials. Complex behaviours of fluids with elastic properties are observed in processes ranging from polymer manufacture to physiological systems. This study will employ a meshless Lagrangian approach to simulate viscoelastic flows, utilising the Oldroyd-B constitutive model, renowned for its efficacy in representing intricate viscoelastic phenomena. As companies increasingly depend on numerical simulations to enhance processes and evaluate material behaviour, the generation of reliable computational tools is essential. Lagrangian meshless methods provide a potential technique for precisely and efficiently recording the dynamics of viscoelastic flows. This study seeks to fill existing knowledge gaps in the numerics of Lagrangian meshless methods, aiming to enhance the basic comprehension of viscoelastic phenomena and to foster optimisation and innovative thinking in various areas such as material technology and biomedical research.

Continuum mechanics is the predominant method utilised for simulating macroscopic flows. Closure assumptions prove crucial for deriving continuum constitutive mathematical equations from kinetic theories. In actual computational simulations, the constitutive model and the material characteristics are generally obtained via rheological measurements. Nonetheless, it is crucial to approach the application of constitutive models obtained from curve-fitting of rheometric flows (e.g., simple shear or uniaxial extensional) to more complex flows with critical thought [16]. Viscoelastic flows present challenges in simulation due to their sophisticated behaviour, characterised by the interplay of viscous and elastic processes [17]. The stiff nature of the hyperbolic form of the differential constitutive equations renders the numerical modelling of these viscoelastic flows vulnerable to numerical instabilities, physical flow fluctuations, and nonphysical constitutive instabilities. [18, 16]. The numerical difficulty of resolving these constitutive equations, known as the high Weissenberg number problem (HWNP), has presented a considerable obstacle in computational rheology for almost two decades.

The domain of research dedicated to simulating viscoelastic flows has now arrived at a pivotal point characterised by a synthesis of progress and obstacles. Researchers

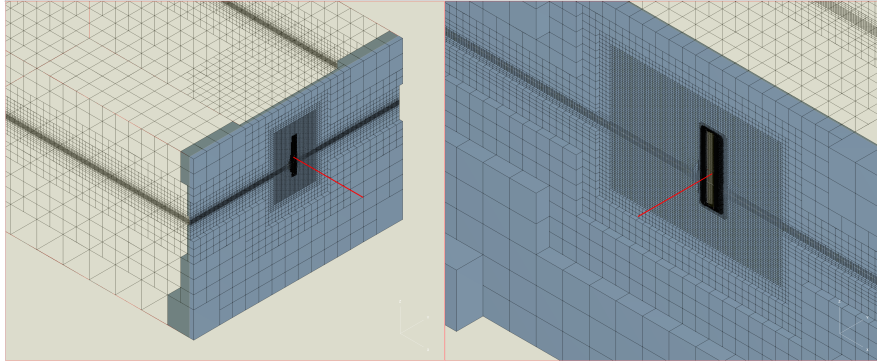


Figure 1.1: An example of an unstructured volume mesh prepared for a FVM simulation.

have achieved notable advancements in numerical approaches, particularly emphasizing meshless techniques for modelling the complex dynamics of viscoelastic materials. The current state of the discipline is marked by a growing recognition of the importance of accurate simulations for applications ranging from industrial processes, such as polymer production, to biological systems, such as blood circulation. The preliminary mathematical models introduced in the field of continuum mechanics were formulated by Oldroyd [19], nevertheless, the Oldroyd–B model remains a primary focus in research into constitutive models. The Upper-convected Maxwell (UCM), Oldroyd-B, and corotational Maxwell models exemplify earliest constitutive equations that are differential equations for the extra-stress tensor. Castillo Sánchez et al. [20] critically analysed the prevalent application of the Oldroyd-B model in forecasting instabilities in various shearing flows of viscoelastic fluids, highlighting its qualitative efficacy while acknowledging its limitations and proposing enhancements through more realistic constitutive models, alongside addressing unresolved issues in viscoelastic stability. Castillo et al. [20] authored a review article celebrating the birth of James Oldroyd, analysing the widespread application of the Oldroyd-B model in forecasting instabilities in various shearing flows of viscoelastic fluids. The article highlights its qualitative efficacy despite inherent limitations and explores potential enhancements through more realistic constitutive models, as well as unresolved enquiries in viscoelastic stability.

1.2 Numerical methods

1.2.1 Mesh-based methods

Mesh-based methods require a discretization of space in the form of subdivisions, which make a grid or a mesh. The mesh can contain complex topology, i.e. connectivity graphs between elements, and it can be locally refined where needed. An example of an a volumetric mesh for the FVM is shown in Figure 1.1. Popular mesh-based

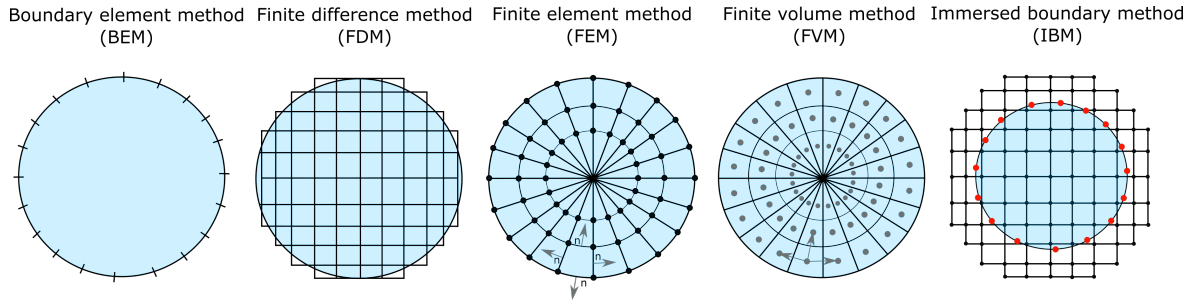


Figure 1.2: An example of an unstructured volume mesh prepared for a FVM simulation.

methods are listed below, and their characteristics are briefly described.

Boundary element method (BEM)

The boundary element method (BEM) is a fully equipped numerical technique for solving integral partial differential equations. Instead of using the entire space defined by the partial differential equation, the boundary element method attempts to fit the boundary values into the integral equation using the given boundary conditions. The integral equation can be used in the post-processing phase to directly compute the numerical solution at any desired point on the domain's boundary. As a result, the BEM discretizes the boundary and it is unsolvable for homogeneous and non-linear problems. It is more appropriate for domains that are infinite or semi-infinite.

Finite difference method (FDM)

The finite difference method (FDM) is a numerical technique for approximating differential equations. The FDM technique in a simple way solves linear or nonlinear ordinary differential equations (ODEs) or partial differential equations (PDEs). The method uses finite differences to replace derivatives in a differential equation. Then it converts them into a system of linear equations that matrix algebra can solve. The algebraic equations that result are solved, and an approximate solution is obtained. The domain must be structured in order to yield accurate derivatives and therefore produce. Simple forms of FDM are inapplicable in unstructured domains, and mesh refining worsens conditioning. Generalized FDM, on the other hand, can be applied to complicated domains in a mesh-free manner, which is explained below.

Finite element method (FEM)

The finite element method (FEM) solves differential equations in two or three space variables numerically. The method is capable of dealing with complex domains. Space discretization divides large systems into smaller parts, known as finite elements. Finite

elements accurately represent the complex geometry, and they can include dissimilar material properties. They are building the object's mesh, which represents the numerical domain used for calculations with a finite number of elements. The FEM formulation of the boundary value problem yields an algebraic equation system. Over the entire domain, the unknown function is approximated. Simple equations representing finite elements are combined to form a large system of equations that models the entire problem. In this manner, an easy representation of the total solution is obtained, as well as the capture of local effects. When the domain is discretized with many elements, conditioning issues arise. The FEM is more difficult and time-consuming to implement than the FDM. Both FEM and FDM struggle with large-scale problems and sparse matrices.

Particle Finite Element Method (PFEM)

Particle Finite Element Method (PFEM) models complex multidisciplinary engineering problems by combining Lagrangian particles and FEM. It is a tool for resolving multiphysics problems in evolving domains. The PFEM discretizes the physical domain with a mesh, and the governing PDEs are solved using the standard FEM method. The mesh nodes move according to the equation of motion when the fully Lagrangian approach is used. They behave like particles, and each particle has its own set of mathematical and physical properties. Mesh distortion is a common problem for mesh-based Lagrangian solvers, and it is usually resolved by creating a new mesh when the old one is too distorted. By keeping the nodes of a previous mesh fixed, PFEM avoids remapping from one mesh to another.

Finite volume method (FVM)

The finite volume method (FVM) is numerical method that solves PDEs. FVM is based on the mass conservation equations, described using fluxes. The concept of dividing a domain into finite volumes or cells is similar to that of the FEM. The conservation law is implemented in such a way that mass that enters the cell must exit the cell on the other side. In other words, the divergence term in volume integral is converted to surface integral using the divergence theorem. These terms represent fluxes at the surface of each finite volume cell. The method is suitable for unstructured meshes. The FVM can be compared with FDM in terms of using approximate derivatives in node points and with FEM by creating local approximations in order to get the global result.

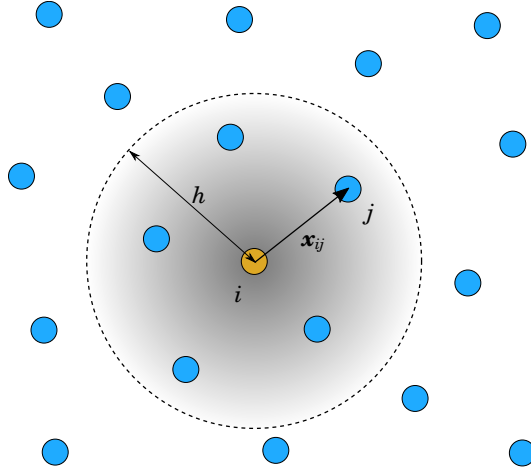


Figure 1.3: A representation of meshless discretization as a point cloud.

Immersed boundary method (IBM)

The immersed boundary method (IBM) is an approach for simulating fluid-structure interaction (FSI). It was first used to study blood flow through heart valves. The method solves coupled equations of motion for an elastic incompressible structure in a viscous and compressible fluid environment. It solves incompressible NS equations in particular. Delta function kernel equations describe the interaction of structure and fluid. The idea is that when the structure moves and deforms, there will be deformation that will push the structure to its preferred position, and the fluid near the structure will feel those effects. Similarly, when the fluid is moving, the structure needs to move at that same fluid velocity as well. The method employs two distinct grids. The first grid represents the fluid and is known as the Eulerian frame or grid. There are no individual fluid particles floating around; there are positions that are throwing down a velocity probe and measuring the fluid velocity at these positions through the simulation. There is, on the other hand, an actual immersed boundary or Lagrangian frame. That structure is deformable and has some physical material properties. Both grids are stacked on top of each other and communicate using differential equations as described below. Fiber models are material properties that can be implemented in a variety of ways. The fiber models are those that make this method powerful.

1.2.2 Meshless Methods

Instead of discretizing space by finite volumes or finite elements, meshless methods discretize space as point clouds. The chunk of fluid volume is represented by a particle, while a point describes the state of fluid without the volume information. An example of how the point cloud can replace the mesh discretization is shown in Figure 1.3.

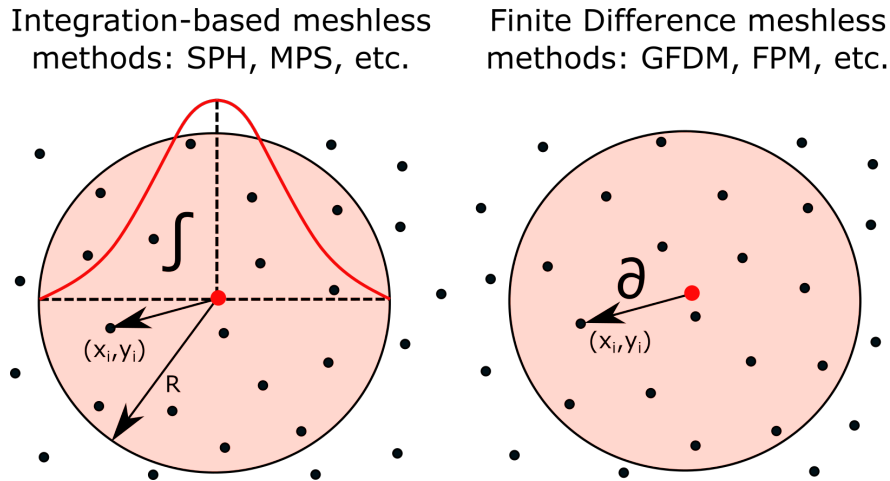


Figure 1.4: Meshless discretization.

Smoothed Particle Hydrodynamics (SPH) methods

Smoothed Particle Hydrodynamics (SPH) is a particle-based simulation method for solid mechanics and fluid flows. It can be used to calculate free surface flows or large boundary displacements. The continuum is defined as a cloud of discrete particles each with its own set of properties. The SPH defines the continuum description as an interpolation problem. The continuum field can be reconstructed by interpolating the scattered data. SPH represents particles in 2d and 3d using a Gaussian-like function. The end result is a smooth particle representation. It was thus given the name "smoothed" particle hydrodynamic. The Gaussian-like function is also known as the kernel function. It is possible to achieve a constant and continuous function by stacking particles together. Essentially, in the SPH, any type of PDE, such as conservation law, is transformed into an integral equation. After that, the kernel estimate provides an approximation for predicting field variables at discrete points. Changing the kernel functions and smoothing length can have an effect on the results as well as particle distribution along the axis. Furthermore, particle distribution significantly affects the gradient accuracy. Due to the lack of mesh, the calculation and implementation procedures are simplified, and the code can be fully parallelized.

Moving Particle Semi-Implicit (MPS) methods

The Moving Particle Semi-Implicit (MPS) method is a Lagrangian method for free-surface incompressible flows. By solving the Navier-Stokes equations in a Lagrangian framework, fluid can be represented by particles whose motion is calculated by a kernel function based on interaction with neighboring cells. To divide each time step into prediction and correction steps, the fractional step method is used. The method is a derivative of the SPH method and was created to address the shortcomings of the

SPH method for liquids and free-surface problems. The MPS is similar to SPH in that it provides approximation of the strong form of PDEs. The MPS employs simplified differential operators. The method employs local weighting in the absence of a kernel gradient. Basic SPH is used for compressible fluids, whereas weakly compressible SPH is used for liquid problems where the density is relatively constant. The kernel used in MPS is more of an asymptotic function than a smooth function like in SPH. Which of the following is a more natural description of particle-particle interaction. Because this is a semi-implicit method, the solution differs from SPH, which is a fully explicit method.

Generalized Finite Difference Method (GFDM)

The FDM contributed significantly to the generalized finite difference method (GFDM). In contrast to FDM, which requires the creation of an orthogonal grid, GFDM can be applied to an irregular set of points. It only requires the node coordinates. The method is applicable to any type of continuously changing domain geometry and can properly handle boundary conditions. The GFDM employs interpolation based on the Taylor series expansion and weighted least-squares fitting. In the method, it is critical to determine the effects of the weighting function, radius of influence, and stability parameters on time-dependent problems. Higher order approximations can be used to control the precision of the GFDM. Any physical or geometrical nonlinearity that occurs has no effect on the algorithm.

Finite Pointset Method (FPM)

The finite point-set method (FPM) is a numerical method used in continuum mechanics. FPM is a strong formulation that models PDS through direct operator approximation. For the FPM, the moving least squares (MLS) method is used and developed. In FPM, the fluid is represented by a collection of sampling points with local properties such as the pressure and velocity. This method differs from the others in that it allows for the use of a mixed Lagrangian-Eulerian approach. The points can move in a Lagrangian manner along with the flow or they can be fixed while the flow passes by them (Eulerian approach). In the Lagrangian approach, points can be added or removed to maintain the specified density. Smoothing length is commonly used to specify density. If increased accuracy is required, points could also be added in the Eulerian approach. The neighbor points are not fixed in either approach and are determined at each time step. The FPM, like most of mesh-free methods, can handle complex and/or time-evolving geometries and moving phase boundaries without additional computational effort. However, in order to produce good results, the points must cover the entire

domain area. The points are not allowed to have gaps between them, which means that each point must have a certain number of neighbors and cannot cluster.

Discrete Element Method (DEM)

The Discrete Element Method (DEM) is designed to simulate the collective behavior of a large number of distinct interacting particles. DEM explicitly tracks the motion, translation and rotation, of each individual particle based on Newton's laws of motion. Inter-particle forces are calculated directly from contact mechanics models, which define how particles interact upon collision or contact, typically incorporating repulsive, dissipative, and frictional components. The overall macroscopic behavior of the granular assembly or particulate system then emerges from the sum of these numerous individual particle interactions and motions. Its primary strength lies in its ability to provide micro-mechanical insights into granular systems, revealing phenomena such as force chain development, stress arching, particle segregation, that are difficult to capture with continuum approaches. However, when considering the simulation of non-Newtonian fluids, the computational cost sufficiently large number of discrete elements to avoid scale effects can become prohibitively expensive. Secondly, defining appropriate inter-particle contact laws that accurately replicate the complex rheology of a non-Newtonian fluid is non-trivial and often requires significant phenomenological calibration or multi-scale bridging.

1.3 Past research overview

BEM. The BEM is used in microfluidic pumping of non-Newtonian blood flow in combination with immersed boundary-lattice Boltzmann method (IB-LBM) Ren et al. [21]. The results of the calculations in the porous cavity show that BEM can be used effectively to solve transport phenomena in a saturated porous medium Jecl et al. [22, 23]. Florez et al. [24] used the BEM method to solve non-Newtonian flow in multi-domain problem that included viscous dissipation, temperature dependent viscosity, and natural convection. The multi-domain technique is a method of domain partitioning that divides the domain into smaller parts. Included effects brought numerical results closer to experimental results. Giraldo et al. [25] tracked motion and deformation of shear-thinning drop suspended in a Newtonian circular Couette flow (flow of a viscous fluid between two surfaces) with BEM method. The apparent viscosity was modeled with Power Law model. The results revealed that non-Newtonian drops had larger deformations than Newtonian drops due to a general decrease in viscosity. The local viscosities were found to be significantly influenced by both the velocity field generated by the internal cylinder's motion and the surface tension forces.

FDM. Eldabe et al. [26] investigated non-Newtonian Casson fluid with magnetohydrodynamics (MHD) boundary layer flow on a moving wedge with heat and mass transfer. Consideration is given to the effects of thermal diffusion and diffusion thermo with an induced magnetic field. This approximate numerical solution was found to be in good agreement with the analytical solution. Malkus et al. [27] investigated plane slow flow of a Maxwell fluid over a transverse slot. The FDM and FEM methods were used to obtain the results. FDM uses the differential form of the constitutive equation, whereas FEM uses the integral form. The two methods yield different results, especially at low De numbers. Extrapolation of the results to mesh with infinitesimally small spacing, on the other hand, reveals good overall agreement between the two methods. Sankar et al. [28] developed computational model to investigate the effects of a magnetic field in a pulsatile blood flow through narrow arteries with mild stenosis. The blood was treated as a Casson fluid. The simplified nonlinear partial differential equation is solved using FDM. Velocity is obtained with explicit finite-difference scheme. It is discovered that the velocity and flow rate drop as the Hartmann number increases, whereas the opposite pattern is observed for the wall shear stress and longitudinal impedance. Numerical simulations of complex rheological models in the HiGTree/HiGFlow system, demonstrating successful reproduction of shear-banding and yield-stress behaviors, are reported by Castillo-Sánchez et al. [29] through the implementation of finite differences on hierarchical grids and a moving least squares interpolation technique. Numerical simulations of the Modified-Bautista-Manero (MBM) thixotropic-viscoelastic model in expansion-contraction geometries were conducted by Castillo Sánchez et al. [30], demonstrating agreement with existing literature and providing insights into the behavior of corner vortices under varying Deborah and Reynolds numbers, especially in the unexplored 4:1:4 geometry. Castelo et al. [31] presented a moving least squares (MLS) Eulerian meshless interpolation method, facilitating intricate mesh arrangements while preserving overall precision, as evidenced by simulations of generalized Newtonian and viscoelastic fluid dynamics.

FEM. The Finite Element Method (FEM) was used to investigate mostly viscoplastic flows. In the 1980s, viscoelastic fluids were challenging to simulate due to loss of convergence. Fortina et al. [32] investigated numerical schemes for high De numbers. The problem of the convergence loss has tried to be resolved by using upwinding schemes. The simulations were done by decoupling the velocity and stress. The method had drawbacks and the authors suggested the use of better iterative schemes. Szady et al. [33] introduced a new discrete elastic-viscous-split-stress EVSS-G/FEM method which increases numerical stability compared to the original EVSS/FEM method. The results are obtained by simulating the steady-state flow in an eccentric rotating cylinder and a flow through a tube with wavy walls and square array. The authors report that any instabilities in the results came either by the finite element approximation or

the time integration method, that is why they used implicit time integration method. They have proved that with the EVSS-G/FEM method calculations are stable for $De > 100$, while simulations with EVSS/FEM are unstable even for $De > 5$. Grillet et al. [34] in their study used mixed (DEVSS/hp-SUPG) FEM in order to simulate the effect of fluid elasticity and stress distribution in lid-driven cavity flow. They have treated idealized Taylor’s corner, i.e. corner singularities by leaking a small amount of fluid which allowed convergence of the solution. Kren et al. [35] formulated the fundamental continuity and Navier-Stokes equations for Newtonian fluids by employing specific constitutive equations for viscosity to address non-Newtonian fluid flow. The spatial discretization is conducted by employing the FEM method. The method is tested in the total knee replacement by modeling the synovial fluid flow. The method yielded decoupled solutions for fluid flow with deformations. Convection in a square cavity with the Bingham model without regularization was tested in the work of Huligol et al. [36]. The FEM method with the operator-splitting method was used to solve the flow with differently heated vertical sides of the cavity. The yielded and unyielded zones of the flow were found to be easily obtainable. In the paper by Mackay and Phillips [37], a stabilised finite element scheme for compressible nonisothermal viscoelastic fluid flows is presented, exploring the effects of compressibility, viscoelasticity, and thermal influences on benchmark problems such as lid-driven cavity and natural convection flows.

FVM. The Finite Volume Method (FVM) is used in viscoelastic fluid flows. Nefyotou et al. [38] research the non-Newtonian flow effects using generalized Newtonian constitutive equations using the Finite Volume Method (FVM). The FVM solver scheme caused the use of the pressure-correction method in combination with the SIMPLE algorithm. The convective term was calculated by using the third-order accuracy QUICK differencing scheme. In this way, numerical diffusion effects have been avoided. The lid-driven cavity flow is performed for Newtonian and non-Newtonian flows using the viscous models Power Law and Quemada, and viscoplastic models modified Bingham and Casson. The paper investigates the non-dimensional impact of non-Newtonian models and the shear-thickening or shear-thinning characteristics of the fluid. Zou et al. [39] integrated the Lattice Boltzmann method (LBM) with the Finite Volume Method (FVM) and proposed a system for incompressible viscoelastic fluid flow. The novel scheme has the reliability and scalability of LBM and retains the precision and generality of the FVM. The findings are consistent with empirical and numerical results of other FVM schemes. De et al. [40] simulated unsteady viscoelastic fluid with FENE-P model on the 3D porous medium employing FVM with staggered grid. Boundary conditions were applied using a second-order immersed boundary method (IBM) which had previously been used only for Newtonian fluids. Simulations were conducted for De number up to 2.0 and low Reynolds number ($Re = 0.01$) although the cost of the simu-

lation was high. De et al. [41] researched creeping flow of a viscoelastic fluid through a porous 3D medium using FVM-IBM. Increased resistance of flow was associated with an increase in De number. A topology analysis of the flow was performed and it was found that most mechanical energy was dissipated in shear-dominated regions, even at increased viscoelasticity. Meburger et al. [42] present a numerical study that simulates non-isothermal viscoelastic flows at high Weissenberg numbers using a finite volume method utilizing the root conformation approach on unstructured meshes, demonstrating stable solutions and validating the thermo-rheological model against experimental data.

PFEM. In Lagrangian methods, and therefore in Particle Finite Element Method (PFEM), the convective term is not included in the momentum equation, so there is no need for numerical stabilization. But the incompressibility constraint still requires the treatment of stabilized numerical methods. In addition, when large deformations are expected, the Lagrangian approach is more preferable instead of fixed mesh methods. An extensive review of the Particle Finite Element Method (PFEM), outlining its theory, applications, advantages, and disadvantages for simulating multi-physics problems in evolving domains, was presented by Cremonesi et al. [43]. Salazar et al. [44] employed the PFEM to simulate fluid-structure interaction in landslides. Landslides produce impulse waves, and the unpredictable kinematics of the displaced material complicate the calculation of fluid-solid interactions. Application of the method was presented through case studies and actual full-scale measurements where the method provides a good risk analysis that can be used to estimate future full-scale events. Celigueta et al. [45] presented the procedure for coupling the FEM for Eulerian and particle FEM (PFEM) for Lagrangian flows with the discrete element method (DEM). The PFEM-DEM method calculates the drag force on fluid particles for non-Newtonian fluid by predicting the terminal velocity. The method was tested for the cuttings transport process (hole-cleaning) full of circulating fluids. Cremonesi et al. [46] did a number of tests on Newtonian and non-Newtonian fluids in order to validate PFEM method. The method is based on a Lagrangian formulation of the Navier-Stokes equations with an explicit finite-element approach for weakly compressible fluids. The Bingham dam-break test showed good agreement with the experimental results. Larese [47] has introduced a stabilized mixed PFEM for the calculation of non-Newtonian viscoplastic flows. The Bingham model with variable yield threshold in combination with the Mohr-Coulomb resistance criterion was used to analyze the deformation of granular non-cohesive material. The Bingham model has been tested on benchmarks, but does not adequately describe the behavior of the granular slope. The introduced variable yield-threshold does not have a mesh-size limitation, and yet it adequately describes materials with internal friction angles below 45° . Franci and Zhang [48] simulated free-surface Bingham fluids using the Lagrangian approach. Two- and three-dimensional

1 Introduction

simulations are done using the PFEM, and solid structures are simulated by employing FEM. Franci and Zhang [48] showed a lot of tests including a 3D fresh concrete slump problem. In particular, this test is the most widely accepted tool for measuring cement consistency at the work site, as viscometers are not accepted when it comes to ongoing construction. Della Vecchia et al. [49] examined Bingham fluids, focussing on the rheological properties of water-soil mixes during dam-break experiments. The numerical analysis investigated the viscosity and yield stress of the Bingham model by CFD-PFEM parametric studies. Since the yield stress and viscosity could not be recognized separately from the position of the evolving liquefied mass in the experiment, these parameters were attempted to be identified with PFEM simulations. They are obtained by monitoring the evolving aspect ratio of the flow mass or fluid pressure on a rigid obstacle. The results of the PFEM revealed linearity between researched parameters. A particle finite element method (PFEM) implementation for simulating viscoelastic free-surface flows, validated against benchmark flows, including an implementation of the Oldroyd-B constitutive model and a new approach for applying unilateral Dirichlet boundary conditions, was presented by Rizzieri et al. [50]. A direct numerical simulation (DNS) study of polymer-laden turbulent pipe flow, investigating the impact of polymer parameters and contrasting the FENE and FENE-P models using a two-way coupled Lagrangian approach, was presented by Serafini et al. [51], revealing the limitations of Peterlin’s approximation and proposing a new polymer Reynolds number as a key dynamic parameter.

MPM. Gordon et al. [52] proposed a novel variant of the Material Point Method (MPM) for simulating incompressible viscoelastic flows, demonstrating its effectiveness through various flow scenarios and achieving quadratic convergence for the Oldroyd-B fluid. Recently there are even neural network-based methods proposed to solve non-Newtonian flows [53, 54]. Zhou and Sun [55] propose a weakly compressible B-spline material point method for simulating complex non-Newtonian power law flows, demonstrating its efficacy in capturing various flow features and interactions. Zhou, Hua, and Sun [56] introduce a non-Newtonian general Cross model into the three-dimensional B-spline material point method to effectively simulate granular flow and impact behaviors, demonstrating its applicability in geotechnical engineering problems such as landslides and debris flows. Su et al. [57] proposed a unified second-order accurate MPM formulation for simulating viscoelastic liquids with phase change, integrating various viscosity models and demonstrating its application in 3D simulations. Li, Sovilla, Jiang, and Gaume [58] applied a three-dimensional material point method to model flow regimes in snow avalanches, revealing distinct flow behaviors and textures, and validating their findings with a real avalanche case in Switzerland. Li, Yao, Sun, and Wu [59] present a monolithic method using the material point method to analyze fluid-structure interactions in geohazards, demonstrating its reliability through various

benchmark problems and comparisons with laboratory tests. Ceccato, Yerro, and Di Carluccio [60] reviewed the Material Point Method’s applications in simulating landslides, highlighting its capabilities, challenges, and the need for further advancements in methodology. Kularathna et al. [61] presented a semi-implicit material point method for modeling coupled soil deformation and pore fluid flow, which improved numerical stability and reduced pressure oscillations in saturated soils.

SPH. The Smoothed particle hydrodynamics (SPH) method is widely used for a variety of fluid flow simulations Monghan et al. [62]. It is a Lagrangian and meshless method, suitable for simulating large deformations of solids and fluid flow, and therefore, it has been researched since its first publications Gingold et al. [63], Lucy et al. [64]. Researchers and scientists have been developing the SPH method, solvers and models according to the type of flow, although its traditionally formulation suffers from an inaccurate pressure field Xenakis et al. [65]. The SPH has also been applied to non-Newtonian problems including viscoelastic transient free-surface flows, such as mud and molding flows Fanf et al. and Shao et al. [10, 66], while Hossein et al. [67] presented a GPU implementation of the method to achieve better performance. Shao and Lo et al. [66] simulated a dam-break problem and discussed flow features of Newtonian and non-Newtonian flows. The simulations are conducted with the use of truly Incompressible SPH (ISPH) scheme for simulate divergence-free free surface flows. The advantage resides in the simplicity of monitoring the free surface by an approach analogous to that utilised in the moving particle semi-implicit (MPS) method. The results were consistent with the experiments. Ma et al. [68] in his paper presents a two-phase SPH model utilizing the Oldroyd-B constitutive model and modified Shields criterion to predict sediment transport and erosion in free-surface flow, incorporating correction techniques; the model effectively simulates sediment transport and erosion phenomena under various scouring conditions, demonstrating agreement with earlier studies. Fan et al. [9] devised a matrix-free, implicit SPH solution for very viscous non-Newtonian flows characterised by elevated pressure regions. The conventional, explicit SPH technique proved impractical since it required an exceedingly small time step to provide a robust simulation. Artificial force is created between the particles in order to stabilize the system, i.e. to prevent the tensile instability. With the modified Power Law model used, the method turned out to be suitable for simulating the flow of polymer fluids in the molding process. A 2D incompressible SPH algorithm incorporating a log-conformation formulation with an elasto-viscous stress splitting (EVSS) technique for simulating viscoelastic flows at high Weissenberg numbers was presented by King and Lind [69]. Bhattacharya et al. [8] tackled the tensile instability in SPH for weakly compressible fluids by devising an adaptive algorithm that employs a B-spline function as the SPH kernel, showing its efficiency via dispersion analysis of an Oldroyd B fluid model and benchmark fluid dynamics simulations. Xu and Yu [12] examined the

1 Introduction

problem of tensile instability in SPH when simulating transient viscoelastic free surface flows. They introduced an optimised particle shifting technique and validated its effectiveness through simulations involving impacting drops, injection moulding, and extrudate swell, providing comparisons with other numerical methods and techniques. Zhu et al. [70] in his paper assessed how well the plastic viscosity can be determined using the SPH approach. Papanastasiou's [71] Bingham constitutive model was implemented into the SPH model and tested against the results of published data. The study determined adequacy of the vane rheometer to assess rheological properties. They concluded that higher Bingham number values are responsible for larger sizes of unyielded materials in the inner blade region. Xu et al. [11] advanced the SPH approach to 3D non-Newtonian flows with complex free-surface shapes. The viscosity is calculated using the Casson model. Artificial stress-term is inserted into the momentum equation to prevent tensile instability, which leads to clustering of particles and non-physical defects in fluid stretching. Three complex engineering processes were simulated as non-Newtonian free surface flows, including a droplet-impact problem. The shear thinning behavior was found to be visible in all cases and the developed SPH algorithm was stable, reasonably accurate and consistent with the published results. Xenakis et al. [65] utilised a diffusion-based ISPH method to analyse free-surface flows, wherer the method has been developed to tackle inelastic non-Newtonian flows through the implementation of a novel viscous term. The innovative method was corroborated through comparison with analytical and experimental findings.

HWNP. The HWNP manifests as an absence of simulation stability, leading to a fast escalation of the numerical solution [16]. Inhibition transpires when the Weissenberg number (or Deborah number) attains a critical threshold, which fluctuates based on factors such as flow complexity, spatial discretization, and numerical methodology. The loss of positive-definiteness in the conformation tensor, an intrinsic variable that defines the arrangement of polymer chains, is recognized as a precursor to the HWNP [72]. In addition, Fattal and Kupferman et al. [72, 73] have demonstrated that numerical instabilities arise from inadequate resolution of spatial stress profiles. This is an issue because viscoelastic flow solutions generally entail stress boundary layers characterized by significant fluctuations in stress gradients and exponential stress profiles near geometric singularities. Insufficient representation of stress gradients, such as by polynomial interpolations of exponential profiles, leads to an underestimating of convective stress fluxes. This inaccuracy is subsequently mitigated by doubling the stress increase rate, ultimately resulting in computational inaccuracies. The log-conformation representation [74, 75, 76] preserves positive-definiteness while enhancing the depiction of notable stress gradients by converting exponential stress profiles into linear forms. Challenges associated with a high Weissenberg number are critical in viscoelastic flow, since they pertain to scenarios where elastic forces substantially influence fluid behav-

ior. This results in complicated phenomena such as coil-stretch transitions and elastic instabilities, which present problems for precise simulation and practical understanding in many industrial and research applications. Ensuring numerical stability is crucial for simulating flows with elevated Weissenberg numbers, as these conditions are especially prone to error propagation and solution failure [20, 77]. Verbeeten et al. [78] employed the Discrete Elastic Viscous Stress Splitting Technique alongside the Discontinuous Galerkin (DEVSS/DG) method to model a polyethylene melt, emphasizing the interaction between physical and numerical factors in attaining stable solutions for intricate flows. In order to try to simulate flows with high Weissenberg numbers, [72, 77] proposed the log-conformation formulation inside the framework of the FDM, employing the matrix logarithm of the conformation tensor to enhance stability at high Weissenberg numbers. This indicates that logarithmic variables mitigate numerical instability problems, while persistent obstacles pertain to accuracy deterioration at inadequate resolution. Ke and Wang [79] illustrated that multiple momentum equation stabilization algorithms markedly improve the stability of the Log-Conformation Representation method for low viscosity ratio viscoelastic lid-driven cavity flow simulations, enabling a decrease in the viscosity ratio that can be stably simulated and requiring shorter time steps relative to the original cases. Comminal et al. [16] integrated the log-conformation formulation with the streamfunction representation for incompressible viscoelastic flows. Fernandes [76] presented a block-coupled methodology for calculating viscoelastic flows via the log-conformation tensor method, utilizing implicit discretization for several terms and validating the algorithm for non-isothermal viscoelastic Oldroyd-B fluid dynamics. Meburger et al. [42] presented a methodology employing the root conformation technique on unstructured meshes, exhibiting stability and confirmation with experimental data for elevated Weissenberg numbers and varying wall temperatures. Fernandes et al. [80] presented an enhanced both-sides diffusion scheme within a finite volume method framework for simulating viscoelastic fluid flows, exhibiting precise predictions for benchmark cases and attaining steady-state solutions with refined meshes and a convergence rate approaching second order. The work of [74] also enhanced the stability of a FVM viscoelastic solver, demonstrating second-order accuracy in time and space for low Deborah numbers, while providing new insights into the vortex dynamics and transient behavior in the 4:1 planar contraction experiment. Giorgi and Morro [81] proposed a framework for modeling viscoelastic materials through the introduction of constitutive functions derived from measures of strain, stress, heat flux, and their temporal derivatives. This approach maintains adherence to the second law of thermodynamics and accommodates a diverse array of models, including nonlinear thermo-viscoelastic materials exhibiting significant deformations, thereby encompassing established models. Westervof et al. [82] introduced the Tensor Diffusion approach for simulating viscoelastic fluids, demonstrating its ability to

decompose the extra-stress tensor and reduce complex viscoelastic models to a generalized Stokes-like problem, thereby enhancing numerical behavior and convergence in various flow configurations. [3] demonstrate that the tensor interpolation method is identified as the primary cause of the loss of symmetric positive-definite property in conformation tensors, which exacerbates the high Weissenberg number problem in viscoelastic fluid flow, and they propose a tensor-based interpolation method that effectively enhances numerical accuracy and maintains the symmetric positive-definite property.

Miscellaneous. Other studies have been made investigating turbulence, sediment transport, etc. Sasmal [83] review the current understanding of electro-elastic instability and turbulence in electro-osmotic flows of viscoelastic fluids, highlighting the significant alterations in flow behavior due to viscoelasticity and the necessity for further research to explore their practical applications in microscale flow systems. Gupta and Sasmal [84] conducted extensive numerical simulations to elucidate the complex relationship between cavity aspect ratio and mixed convective heat transfer, revealing that the heat transfer rate’s dependency on aspect ratio varies significantly with Richardson and Prandtl numbers, with notable differences observed between Newtonian and viscoelastic fluids under different conditions. Brandi et al. [85] examine laminar-turbulent transition in viscoelastic fluid flows through Direct Numerical Simulation (DNS) and Linear Stability Theory (LST), illustrating the impact of polymer concentration and elastic forces on critical Reynolds numbers, and uncovering alterations in flow structures for particular parameters. Recent research additionally incorporate machine learning (ML) methods. For example, the study of Faroughi et al. [54] presented a machine learning framework utilizing Random Forest, Deep Neural Network, and Extreme Gradient Boosting models to assess the drag coefficient of spherical particles in a viscoelastic fluid, based on datasets derived from direct numerical simulations (DNSs). Su et al. [86] conducted a numerical study that examined the nonlinear behavior of electrohydrodynamic flow in viscoelastic fluids, revealing that viscoelasticity induces unique hydrodynamic behaviors and alters the transition to chaos compared to Newtonian fluids.

1.4 Motivation and open challenges

The study and application of non-Newtonian fluids is a vibrant area of research and development. Ongoing advancements are being made in the development of more accurate constitutive models and CFD techniques to better predict and simulate the complex flow behavior of these materials, particularly in intricate geometries or under extreme conditions. Novel applications continue to emerge, driven by progress in materials

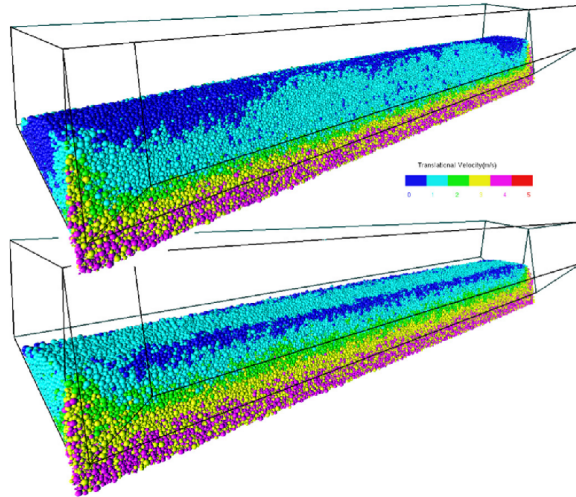


Figure 1.5: Gravitational hopper discharge using spherical particles solved by the DEM.

science and engineering. These include the development of increasingly sophisticated "smart" materials and structures incorporating responsive fluids. The continued exploration and manipulation of non-Newtonian fluid behavior promise further innovations and technological advancements across scientific and industrial domains, underscoring the enduring importance of understanding the complex ways in which matter can flow.

In the pursuit of advancing our comprehension of non-Newtonian flows, this PhD thesis emphasizes the pivotal role of numerical modeling as a powerful tool for unraveling the intricate physics governing these complex fluid dynamics. By introducing novelties to the current computational methods, this research aims to bridge theoretical insights with practical applications, enabling a deeper understanding of non-Newtonian behaviors crucial for optimizing industrial processes and engineering applications. The following sections describe the main motivation and challenges that have been addressed by the novelties of numerical modelling, that are introduced in this thesis.

1.4.1 Motivational prior research

Prior research, before starting to research the area involved in this thesis, included simulating the discharge of granular cargo from Trailing-Suction Hopper Dredgers (TSHD) using the Discrete Element Method (DEM) [87]. This work highlighted the impact of material dynamics show in Figure 1.5 on the stability of the ship, and underscored the complexities of modeling even seemingly simple particulate flows. While the DEM proved as effective tool for simulating granular systems, it also illuminated the computational challenges and inherent limitations when considering mixture of wet materials that behave more as a continuous medium. It has come to the conclusion that the simulated substances in [87] actually exhibit complex non-Newtonian flow behaviors

(viscoplasticity and viscoelasticity), which are better characterized using continuum mechanics principles. This realization motivated the initiation of the current PhD research, which shifts focus from discrete particle dynamics to the development and application of continuum-based numerical methods for simulating these challenging non-Newtonian flows. Therefore, the resulting goal is to leverage the strengths of continuum approaches to efficiently and accurately capture the macroscopic flow behavior governed by sophisticated constitutive laws, addressing phenomena not readily captured by particulate methods.

1.4.2 Complex and large deformations

A central challenge in simulating non-Newtonian flows, particularly those involving viscoelasticity or viscoplasticity, lies in accurately capturing the material's deformation. Unlike simple Newtonian fluids, the stress state in these materials is often intricately linked not just to the instantaneous rate of strain, but also to the history of deformation and the magnitude of accumulated strain. Phenomena such as stress relaxation, creep, yielding, and large elastic recoveries are direct consequences of how the material deforms over time.

Traditional Eulerian mesh-based methods, such as the FVM or FEM implemented on a fixed grid, face significant hurdles when dealing with the complex deformations characteristic of rheological flows. In an Eulerian framework, the fluid moves through a fixed mesh. Accurately tracking the deformation history of a specific material element becomes computationally demanding and prone to numerical diffusion. Reconstructing the history requires complex advection schemes and interpolation, which can smear out the very memory effects crucial for viscoelastic models, especially when dealing with sharp stress gradients or complex flow paths. While Eulerian methods avoid the mesh distortion inherent in Lagrangian mesh-based methods, they struggle with accurately representing large material stretching, folding, fragmentation, or coalescence, especially at free surfaces or interfaces. Methods like Volume of Fluid (VOF) or Level-Set are required to capture the interface, adding complexity and potentially introducing issues with mass conservation or interface sharpness. Simulating phenomena like die swell, droplet impact and breakup, or filament stretching becomes significantly complicated. Due to the memory effects of viscoelastic fluids, Lagrangian perspective is natural [88]. Lagrangian perspective is particularly effective in modelling complex flows, where the path and interaction of individual fluid elements are of significant interest, such as in turbulent flows or multi-phase systems. By focusing on the movement and interaction of individual parcels, Lagrangian numerical methods may provide a detailed and dynamic picture of fluid behaviour, revealing insights into the underlying physical processes and history driving the flow. Consequently, researchers investigated extend-

ing the most famous meshless method, Smoothed Particle Hydrodynamics (SPH), on the viscoelastic flows [9]. The exploration and refinement of meshless methods, such as Lagrangian Differencing Dynamics (LDD) [7], as viable alternatives to traditional mesh-based approaches is one notable trend in the current literature. Meshless methods have gained popularity due to their improved ability to handle complex geometries and dynamic fluid interfaces, providing a promising avenue for simulating viscoelastic flows. Despite these advances, obstacles remain, which are also presented in past research overview.

Computational efficiency, stability, and the ability to deal with highly nonlinear viscoelastic behaviors are still being researched. Furthermore, the field is increasingly recognizing the importance of benchmark problems and standardized validation protocols for evaluating the accuracy and reliability of various numerical methods.

1.4.3 Variability of rheological properties

The simulation is further complicated when rheological properties exhibit significant variability in both space and time. Such variations are common in numerous practical scenarios, e.g. in polymer processing involving temperature gradients [20]. Accurately capturing this spatio-temporal dependence within numerical simulations presents distinct challenges.

From an Eulerian standpoint, handling variable rheological properties necessitates careful consideration. Temporal variations at fixed locations can often be managed directly within the constitutive model. However, spatial variations, particularly those arising from the advection of elements with differing properties require the accurate transport of these scalar or tensorial property fields alongside the primary flow variables. This introduces additional advection equations, which are themselves susceptible to numerical diffusion.

Similarly to the above, the Lagrangian framework offers inherent advantages in managing spatio-temporal property variations. Since material properties are directly associated with and carried by the Lagrangian particles, their advection is implicitly handled by the particle motion, circumventing the numerical diffusion associated with explicitly solving advection equations for property fields on a fixed grid. Temporal evolution of properties due to intrinsic material kinetics, such as thixotropic structural changes or temperature-dependent viscosity changes within a material parcel subject to heat transfer, can often be described by ordinary differential equations (ODE) solved locally for each particle. Spatial variations in properties across the domain arise naturally from the initial distribution of particles with different characteristics or from the differing histories experienced by particles as they traverse the flow field.

However, the Lagrangian perspective is not without its own set of challenges. While the advection is simplified, the accurate computation of spatial gradients relies heavily on the quality of the meshless spatial differentiation operators and the local particle distribution. Maintaining sufficient particle regularity and accurately approximating derivatives from potentially irregular point clouds is crucial.

1.4.4 High–Weissenberg number challenges

A high Weissenberg number is a dimensionless number used in rheology to characterize the relative importance of elastic and viscous effects in a material. It is defined as the product of the characteristic time scale of deformation (usually relaxation time) and the characteristic rate of deformation (usually shear rate) in a rheological experiment, divided by the characteristic size of the system. When the Weissenberg number is high, it implies that the rate of deformation is much faster than the material’s ability to relax and adjust to the applied stress. This can lead to several challenges and problems in simulating rheological behavior.

Complex constitutive models must be adopted at high Weissenberg numbers, the material behaves in a highly elastic manner, which means it can store and release large amounts of energy during deformation. Capturing this behavior accurately requires the use of complex viscoelastic constitutive models, such as the Oldroyd-B [19], Giesekus [89], or FENE-P models [51], which involve numerous parameters and equations. These models may include terms to account for shear-thinning, shear-thickening, and relaxation behavior, making simulations mathematically intricate.

In numerical simulations of rheological behavior, it’s common to use finite difference FDM or finite element methods FEM [41]. When the Weissenberg number is high, the rapid changes in stress and strain rates can cause instability in the numerical solution, necessitating careful selection of numerical methods, mesh refinement, and time-stepping schemes to maintain stability [73]. In other words, the mesh resolution and time step used in numerical simulations may need to be very small to capture the rapid changes in stress and deformation. This increases computational demands substantially. High Weissenberg number regimes also lead to nonlinear rheological behavior, i.e. nonlinear relationship between stress and strain. Materials may exhibit strain hardening or softening, non-Newtonian behavior, or even viscoelastic effects that are challenging to model accurately. The viscoelastic response at high Weissenberg numbers may exhibit transient effects, including overshoots and undershoots in stress or strain, which can be difficult to predict and control. In conclusion, these behaviors are challenging to capture accurately in simulations and consequently, simulating high Weissenberg number flows requires significant computational resources.

Finally, it should also be noted that experimental validation of high Weissenberg number simulations can be challenging because it requires specialized equipment capable of applying high-frequency or high-strain-rate deformations to viscoelastic materials [49, 90]. Researchers must address these complexities to accurately model and understand the behavior of viscoelastic materials under high deformation rates or high-frequency deformations, which are relevant in various engineering and scientific applications.

1.4.5 Rationale

The simulation of non-Newtonian fluids, particularly those exhibiting viscoelastic or viscoplastic behavior, presents substantial computational challenges. As detailed in previous sections, accurately capturing large material deformations, evolving free surfaces, historical memory effects, variable rheological properties, and resolving issues like the HWNP requires specialized numerical approaches. Traditional mesh-based Eulerian methods often struggle with convective term complexities and mesh distortion for large deformations, while purely explicit Lagrangian methods can be limited by restrictive time-step constraints.

This thesis proposes and validates an enhanced Lagrangian Differencing Dynamics (LDD) method specifically tailored for simulating such complex non-Newtonian flows. LDD is a meshless, particle-based Lagrangian approach that combines the inherent advantages of tracking material history and handling large deformations (characteristic of Lagrangian methods) with the robustness of a semi-implicit solution scheme. Building upon the foundational LDD framework [91, 4, 7], which utilizes second-order consistent spatial operators derived from finite differences, a split-step decoupling for the generalised Navier-Stokes Equations (NSE) is introduced. The main challenges that remain to be resolved are as follows:

- Pressure and velocity are implicitly calculated in the methods that produce accurate results. The majority of these methods are mesh-based and Eulerian in nature, but they must deal with frameworks constrained by non-linear convective terms. Moreover, the CFL number requires good mesh quality and small time-step values for these methods to remain stable and accurate. The most well-known mesh methods are FEM and FVM. Besides the CFL and convective term, other open challenges are related to mesh-deformation issues and interface advection.
- A Lagrangian description of the flow, on the other hand, is natural description in which points move with the flow and do not require modeling of the convective term. These methods can be more efficient and can deal with larger time-step

values. Although the NSE lack of a convective term makes this type of flow description appealing to be solved implicitly, most Lagrangian methods are solved in the explicit manner. A method that efficiently and accurately describes flow in a Lagrangian manner and implicitly solves velocity and pressure is an open challenge. The PFEM method combines the Lagrangian and implicit methods well, but it still relies on the generated mesh. GFDM methods, on the other hand, can be implemented in the fully Lagrangian context but rely heavily on operators that are relatively slow.

- Having a Lagrangian method that is fully implicit and mesh-free would be a significant improvement. In theory, that method should produce accurate results, and it would be faster than traditional mesh-based Eulerian implicit methods but slower than Lagrangian explicit methods. At the same time, larger time-step could be used, resulting in a negligible loss of speed due to implicit solving pressure and velocity. This type of Lagrangian differencing dynamics could also be used to solve FSI problems with large deformations of the structure in any type of flow.
- Non-Newtonian flows with variable viscosity, as well as the governing equations that describe these multi-character flows, are major issues in industrial processes that require special attention. Processes that include mixing products with non-Newtonian character are still unsolved. Since viscosity resists to fluid motion, the motion created by the mixer impeller leaves portion of a tank unmixed. For shear-thinning and shear-thickening fluids the apparent viscosity is proportional to rotational speed. Time-independent fluids are influenced by shear rate applied to them, while time-dependent fluids change viscosity not only with shear rate, but also during and after the applied shear stress. The problem arises much more when mixing process creates non-Newtonian fluid (start with low viscosity and ends with high viscosity). Powder addition and emulsification can also be an issue.

Based on this rationale, this thesis introduces two critical, viscoplasticity and viscoelasticity, extensions:

- Generalized non-Newtonian viscosity: the scheme is adapted to solve the generalized NSE, explicitly accounting for variable viscosity dependent on local flow conditions, crucial for viscoplastic and shear-rate-dependent fluids.
- Viscoelastic modeling: the Oldroyd-B constitutive model, recognized for its ability to represent fundamental viscoelastic phenomena like stress relaxation and elastic recovery, is integrated into the LDD framework to simulate viscoelastic flows. The momentum equation is solved implicitly to robustly handle the coupling between flow and viscoelastic stresses.

1 Introduction

The objective of the extensions is to develop and demonstrate a more accurate, stable, and efficient numerical tool for complex rheological simulations. By leveraging the meshless Lagrangian nature of LDD, this research aims to overcome key limitations associated with conventional methods, thereby advancing our predictive capabilities. Such advancements are critical for optimizing industrial processes (e.g., polymer processing, mixing), understanding biomedical phenomena (e.g., blood flow), and analyzing geophysical flows, where non-Newtonian behavior is prevalent.

The following benchmarks are used to evaluate LDD's efficacy in simulating viscoplastic flows: Square lid cavity flow, Skewed lid-driven cavity flow, Dam break of a Bingham fluid, and fresh concrete slump. A lid-driven cavity simulates the flow inside a cavity with lid moving at a constant velocity. It is used to assess how accurately a method captures the recirculation and shear-thinning behavior of viscoelastic fluids in confined spaces. The dam break of a Bingham fluid serves as a difficult benchmark because it describes the abrupt release of a yield-stress fluid and the complex flow behavior involved. The fresh concrete slump test measures the workability and consistency of freshly mixed concrete. This test provides critical information about the quality of the concrete mix, which influences construction practices and ensures that the material meets specified standards for optimal performance and durability in a variety of structural applications.

To assess LDD's effectiveness in simulating viscoelastic flows, the following benchmarks are used: Square lid-driven cavity flow, droplet impact, 4:1 sudden contraction, and die swell in 2D. Droplet Impact simulation shows a droplet colliding with a surface. The ability of LDD to handle complex fluid interfaces and behaviors during impact, such as deformation and breakup, is assessed here. 4:1 Sudden contraction tests how well LDD captures viscoelastic effects such as flow separation, stress relaxation, and flow reformation in geometrically challenging scenarios by simulating fluid flow during a sudden contraction. Die swell in 2D is the expansion of a viscoelastic fluid when it is extruded through a small orifice. The ability of LDD to replicate non-Newtonian behaviors, such as elongational viscosity and elastic effects during flow extension, can be tested by simulating die swell in a 2D environment. The benchmarks help to evaluate LDD's performance in accurately modeling viscoelastic behaviors in a variety of flow scenarios, including confined spaces, complex geometries, and transient events like impact and flow deformation. LDD's effectiveness is determined by its ability to predict flow patterns, viscoelastic effects, and complex fluid dynamics that correspond to experimental observations or established theoretical expectations for these benchmarks.

The remainder of the thesis is structured as follows. Chapter 2 of this thesis provides a basic overview of non-Newtonian fluids, categorising them into time-independent, time-dependent, and viscoelastic types, while also addressing their unique rheological

1 Introduction

features and practical applications. Chapter 3 delineates the mathematical modelling framework, specifying stress, strain, constitutive laws for fluids, and the encapsulation of all pertinent components within the Navier–Stokes equations. Chapter 4 provides a comprehensive survey of many mathematical models employed to characterise the behaviour of both time-independent and time-dependent non-Newtonian fluids. Chapter 5 clarifies the numerical technique of the Lagrangian Differencing Dynamics (LDD) method, encompassing the splitting scheme in Lagrangian context for pressure and velocity, Lagrangian differencing for spatial operators, and the solution of the pressure and velocity equations within this framework. Chapter 6 delineates the verification and validation of the proposed LDD approach by juxtaposing it with experimental and numerical benchmark data for both non-Newtonian viscoplastic and viscoelastic flows. Chapter 7 concludes by summarising the principal findings, emphasising the efficacy of the LDD approach in modelling intricate fluid flows, and lists some prospective ideas to augment its capabilities and investigate novel applications.

2 Non-Newtonian fluids

Non-Newtonian fluids play an important role in both industrial and natural processes. Product performance during the manufacturing process has an impact on multiple industries. Examples include paint in the chemical processing industry, plastics in the plastics processing industry, slurries and muds in the mining industry, blood, lymph fluid, and cell fluid in biomedical flows, and milk, chocolate, and edible oil in the food industry. Non-Newtonian fluids frequently exhibit viscous properties, and it is critical for the designer or engineer to understand the flow behavior of such fluids in order to identify the fluid's physical properties and use these properties to predict flow behavior in industrial processes. As a result, rheological testing and investigation incorporate simulation-based flow studies.

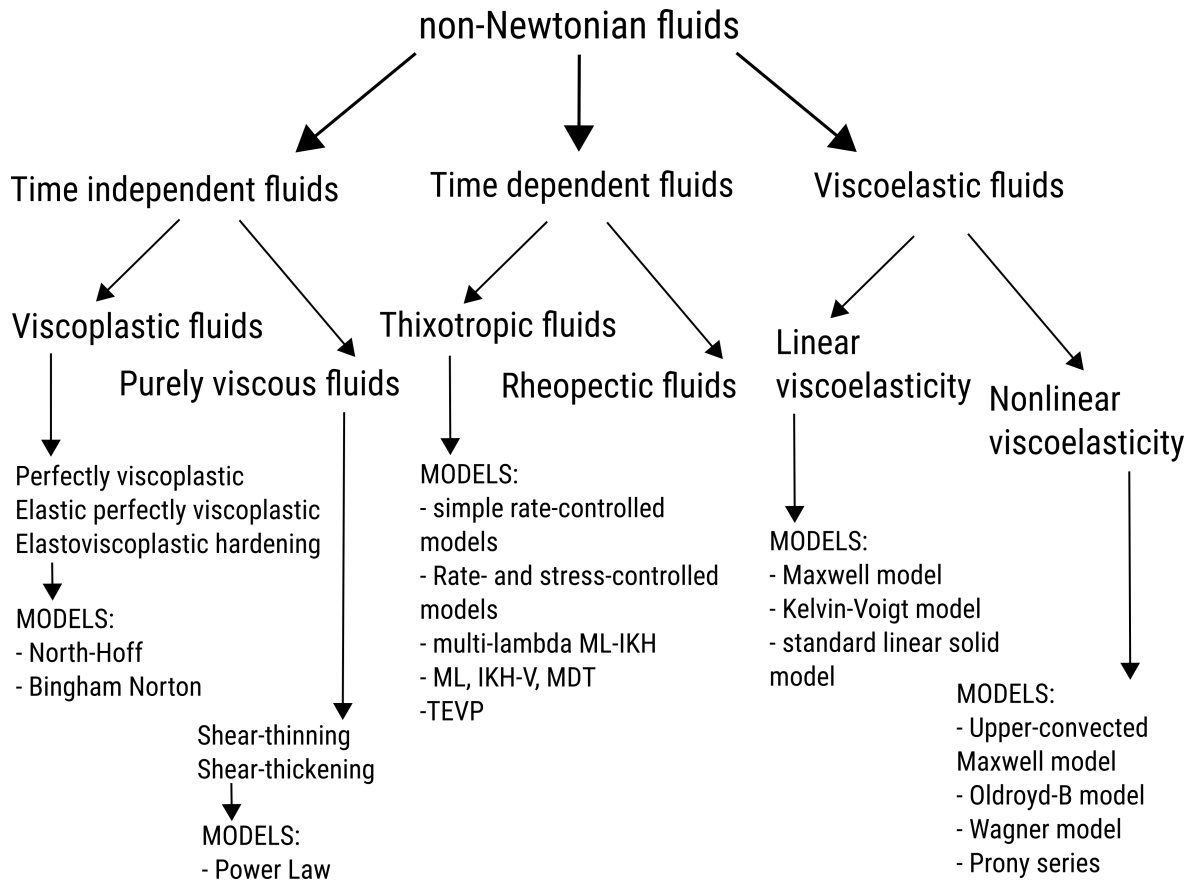


Figure 2.1: Non-Newtonian fluid classification and rheological models.

2 Non-Newtonian fluids

Non-Newtonian fluids are those whose viscosity varies with strain rate, indicating that the viscous stress within the fluid is not linear. The viscous stress tensor and shear rate fluctuate during the flow process. Non-Newtonian fluids move in more complex ways and have different flow characteristics than Newtonian fluids do. The microstructure formed in these fluids is complex, and thus must be studied and described. Non-Newtonian fluids' behavior can be described by relating stress to strain rate. They are divided into various groups and subgroups based on their physical characteristics. Non-Newtonian fluids are classified into three categories: time independent fluids, time dependent fluids, and viscoelastic fluids, as illustrated in Figure 2.1. Some are very different; for example, shear-thinning viscosity can be reduced through mechanical agitation, such as stirring or shaking. These include ketchup, yogurt, and acrylic paints. There are also thixotropic fluids, which means that the relative velocity between fluid layers reduces viscosity. Other materials show the opposite behavior, known as rheopexy, in which viscosity rises due to relative fluid movement. They are also referred to as shear-thickening or dilatant fluids. Considering that, the behavior of foods, beverages, paints, and medications during processing must be considered. Non-Newtonian fluids are used in food processing because their properties can affect the texture, flavor, and appearance of the product. Therefore, maintaining delicate cell structure is critical in the food, paint, and pharmaceutical industries.

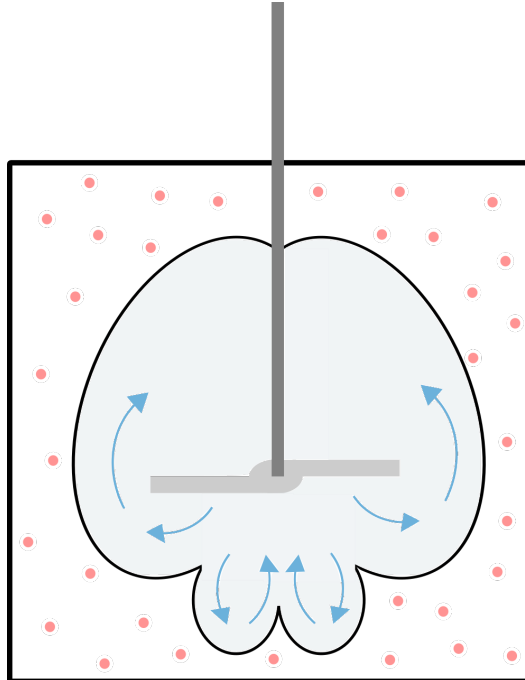


Figure 2.2: Representation of a non-Newtonian fluid moving around an impeller. Red dots represent the stagnant fluid area around the cavern. The size of the cavern is determined by the impeller type and torque.

Because the behavior of foods, beverages, paints, and medications during processing

is important to consider, maintaining delicate cell structure is critical in the food industry, as well as the paint and pharmaceutical industries, among others. Viscosity exists in all liquids and soft solids, and because food and medication processing involves moving goods through systems by applying force to them, viscosity is an important consideration in the design and operation of such industrial processes. Non-Newtonian fluids used in food processing can change the texture, flavor, and appearance of the product. A typical problem for such industries is the mixing problem depicted in Figure 2.2. Shear forces generated by relative motion between fluid layers also have an impact on system design. The shear force acts in a direction parallel to the pump and tube surfaces, and resistance to such forces is proportional to the viscosity and smoothness of the interior pipe surface. The viscosity, pressure, and temperature of the fluid within the system influence the relative velocity of fluid particles, allowing the fluid or soft solid to move either faster or slower. When processed, non-Newtonian fluids react to shear stress and shear rate in a variety of ways. Some thicken, i.e. their viscosity increases with increasing shear rate (cornstarch water mixture), while others become less viscous (blood, ketchup, lotions, etc.). Shear-sensitive fluids (shampoo, egg whites, ketchup) must be handled with care throughout the manufacturing process to ensure product quality. Because the system has an impact on product integrity, it is critical to determine pump speed, pressure generated by the pump, flow rates, pipe diameters, pipe roughness, etc. Maximizing process efficiency involves determining the product's shear sensitivity and viscosity. For example, viscosity influences the time it takes to distribute a product for packing. As a result, a process designed to optimize flow improves efficiency. The most common problem that viscosity and shear sensitivity cause in industrial processes is excessive power consumption and the possibility of product degradation. As a result, rheological testing and investigation involve flow studies at various pressures and temperatures.

If we assume that the description of structurally simple fluids is Newtonian in all possible flows, the description of complex fluids is frequently incomplete, with the exception of relatively limited simple flow kinematics. As a result, many real-world flow descriptions will be qualitative, if not quantitative. There are several aspects to rheological measurements and rheological response analysis using material functions in the process, and the most common modes of rheological observations are associated with steady state characterization. This includes both steady and oscillatory shear, stress, relaxation, and creep. All of them are primarily investigated at small deformations and in the linear viscoelastic range. Deformations can be arbitrarily large in engineering applications, so understanding how the material microstructure responds to large deformations is necessary before claiming to understand the rheological response of these materials.

2.1 Time-independent fluids

Time independent fluids can be subdivided in two groups:

- I. Viscoplastic fluids,
- II. Purely viscous fluids,

These two subgroups of time-independent fluids are explained below.

Viscoplastic fluids

Viscoplastic fluids act as solids until the yield value is exceeded, at which point they begin to flow. The rate of load application determines a viscoplastic fluid's plastic deformation. Toothpaste is a type of viscoplastic fluid. When a viscoplastic fluid is squeezed, the pressure gradient causes the flow. After applying pressure to the tube, the toothpaste is extruded. The velocity in the center is constant, and the flow is plug-like. Several constitutive models have been developed to characterize the behavior of viscoplastic fluids, each offering varying levels of complexity and accuracy:

- Perfectly viscoplastic solid (North-Hoff model), is an idealized model assumes a rigid material that abruptly transitions to plastic flow once the yield stress is reached, without any elastic deformation prior to yielding.
- Elastic perfectly viscoplastic solid (Bingham-Norton model) is a widely used viscoplastic model, incorporates a linear relationship between shear stress and shear rate after the yield stress has been exceeded.
- Elastoviscoplastic hardening solid models are widely used to incorporate a linear relationship between shear stress and shear rate after the yield stress has been exceeded.

Bingham fluids are particularly important class of viscoplastic fluids, due to its prevalence in numerous numerical applications. Bingham material modeling is important in industry because many materials behave like Bingham fluids (e.g., mayonnaise, ketchup, pastes, slurries, toothpaste, foams, oils, ceramics, emulsions, fresh concrete, etc.) [92]. Bingham fluids exhibit a linear behavior, constant viscosity, and constant yield stress. When the Bingham model begins to flow, it behaves as a Newtonian fluid. The Bingham model is used in mud flow calculations for drilling engineering because it only has two parameters: yield stress and plastic viscosity. Inter-particle bonding in the fluid must be broken during drilling by exceeding a specific shear stress limit. Until then, the fluid will be resistant to flow. Once the fluid begins to flow, shear stress and shear rate follow a linear relationship. This helps the drilling fluid suspend solids and cuttings in the fluid when circulation stops. This model is widely used because it is simple and can estimate pressure loss in turbulent flow.

The broader theory of viscoplasticity finds applications in diverse fields, including the estimation of permanent deformations, prediction of structural failure, stability analysis, automobile crash simulations, and the design of high-temperature systems (e.g., turbines and engines) and systems subjected to high strain rates.

Purely viscous fluids

Purely viscous fluids, a subset of time-independent non-Newtonian fluids, are characterized by a viscosity that is solely a function of the instantaneous shear rate. In contrast to Newtonian fluids, they lack a linear relationship between shear stress and shear rate. These purely viscous fluids are broadly categorized into two types

- *Shear-thinning (pseudoplastic) fluids exhibit a decrease in apparent viscosity with increasing shear rate.* The underlying mechanism is often attributed to microstructural changes within the fluid under shear. This behavior is commonly observed in a wide range of materials, including ketchup, mayonnaise, whipped cream, biological fluids (e.g., blood), quicksand, nail polish, modern paints, and most polymer solutions and melts. For example, whipped cream demonstrates this behavior, because at high flow rates, its low viscosity allows for smooth extrusion from a piping bag, while its increased firmness (due to higher viscosity at lower shear rates) allows it to retain its shape when dispensed. In polymer solutions or melts, randomly oriented and entangled polymer chains align themselves in the direction of flow at higher shear rates, reducing intermolecular interactions and flow resistance.
- *Shear-thickening (dilatant) fluids exhibit an increase in apparent viscosity with increasing shear rate,* representing the inverse behavior to shear-thinning fluids. This behavior is less common than shear thinning but is characteristic of concentrated suspensions. These fluids possess the unique ability to transition rapidly from a liquid-like to a solid-like state under sufficient applied load. At low shear rates, particles can move past each other relatively easily, lubricated by the surrounding fluid. At higher shear rates, the particles may be forced into closer contact or form transient jammed structures (hydroclusters), increasing resistance to flow. A mixture of water and sand provides a relevant example. Standing on wet sand causes legs to sink due to its lower viscosity under low shear, while running across it rapidly increases viscosity, creating a more solid-like mixture. A classic demonstration of this phenomenon involves a 2:1 solution of cornstarch in water. At low shear rates, the mixture appears liquid. Stirring it vigorously increases its resistance, while subjecting it to a sudden impact (e.g., throwing a heavy object) can cause it to solidify momentarily, causing the object

to bounce. Upon cessation of the applied stress, the material reverts to its liquid state.

A notable application of shear-thinning fluids is in architectural paints. These paints are designed to spread easily and evenly when applied with a brush or roller (high shear rate), but to resist dripping and sagging on the wall (low shear rate). This combination of properties is achieved by formulating the paint with shear-thinning additives. On the other hand, a notable application of shear-thickening fluids is in body armor. Traditional Kevlar-based body armor, while offering protection, is often stiff, heavy, and provides limited protection to extremities. Shear-thickening fluids, when impregnated into Kevlar fabric, provide enhanced flexibility and impact resistance. For instance, silica nanoparticles suspended in ethylene glycol create a flexible material under normal conditions, but rapidly stiffen upon impact, offering improved protection compared to conventional Kevlar alone.

2.2 Time-dependent fluids

Time-dependent fluids are a class of non-Newtonian fluids whose viscosity is not only dependent on the instantaneous shear rate, but also on the duration and history of applied shear stress. They are generally divided into two categories:

- *Thixotropic fluids, which exhibit a time-dependent decrease in viscosity under constant shear stress or rate.* This means that the longer the shear is applied, the lower the viscosity becomes. This behavior could be described as "shear-thinning over time," and is attributed to the gradual breakdown of the fluid's internal structure under shear. Upon cessation of shear, these fluids require a finite time period to gradually recover their original, higher viscosity as the internal structure slowly reforms. The duration of this recovery time varies between fluids and is associated with the time required for structural rebuilding. While many thixotropic fluids are also shear-thinning, the defining characteristic of thixotropy is this time-dependent nature of the viscosity change and recovery. When subjected to cyclic shear rate variations, this time lag in structural response often manifests as a hysteresis loop in the shear stress versus shear rate plot. Common examples include yogurt, ketchup, peanut butter, many paints, printing inks, some drilling muds, cement slurries, greases, gels, and biological fluids like cytoplasm.
- *Rheopectic fluids, which exhibit a time-dependent increase in viscosity under constant shear stress or rate,* in contrast to thixotropic fluids. Their viscosity increases as a function of both the magnitude and duration of the applied shear. This "shear-thickening over time" is a less common phenomenon than thixotropy,

and rheopectic materials can sometimes be mistaken for shear-thickening fluids. It is important to distinguish it from shear-thickening behavior: shear-thickening is solely dependent on the magnitude of stress, while rheopexy depends on both magnitude and duration. A common example is gypsum paste, which exhibits rheopexy. This paste becomes stiffer only after prolonged beating or mixing.

In summary, thixotropy arises from the duration necessary for particles or structured solutes to arrange themselves systematically. Anti-thixotropic or rheopectic fluids exhibit an increase in viscosity when exposed to stress over a prolonged duration. These phenomena get limited research focus due to their rarity in nature and industrial applications. Thixotropic viscoplastic (TVP) or ideal thixotropic models can be characterised by straightforward rate-controlled, rate-, and stress-controlled frameworks. The models characterised by multiple structural parameters encompass the multi-lambda ML-IKH, ML, IKH-V, MDT, and TEVP models. Thixotropic fluids are present in a variety of substances, including food items like ketchup and yoghurt, as well as in clay, cytoplasm, and ground substance within the human body. Additionally, they are utilised in drilling fluids, grease, printing ink, margarine, and polymer melt. Consequently, they are extensively utilised in the chemical and food sectors. Thixotropic fluids hold significant relevance in the fields of structural and geotechnical engineering, and they are the subject of extensive research efforts. In comparison to thixotropic fluids, rheopectic fluids are notably uncommon. Quicksand exhibits characteristics akin to a thixotropic fluid in its shear-thinning state. Initially it behaves as solid, and upon application of force it transitions to a more viscous state, causing objects that exert stress to sink at an accelerated rate. Gypsum paste, akin to cream, demonstrates rheopexy as it hardens solely after extended agitation. Thixotropy is linked to specific rheological phenomena, such as yielding, hysteresis during shear-rate ramps, the influence of rest time, and viscosity bifurcation.

2.3 Viscoelastic fluids

Viscoelastic fluids exhibit intricate, nonlinear flow characteristics resulting from the interaction of viscous and elastic properties. These fluids are frequently observed in various scientific and engineering applications, such as polymer melts, petroleum products, and biological systems like blood. Moreover, viscoelastic materials, including molten glass, metals, rubbers, and synthetic polymers, are thoroughly researched and employed in a wide range of industrial applications.

Understanding the rheological behaviour of viscoelastic fluids is a considerable problem due to the overlapping occurrence of viscous dissipation and elastic energy storage, intensified by highly nonlinear viscous and elastic characteristics. The interplay of

these constituent elements produces many macroscopic rheological behaviours that may change over time or under applied stress, including elastic-plastic transition, shear thinning, shear thickening, and thixotropy.

Viscoelastic fluids exhibit a duality in their nature, behaving as both solids and liquids. Upon the application of stress, a viscoelastic material can undergo either elastic deformation, plastic deformation, or a combination of both (analogous to pizza dough). When the applied stress remains below the material's yield stress, the deformation is primarily elastic. Conversely, exceeding the yield stress allows for both elastic and plastic deformations to occur, potentially resulting in a linear or non-linear stress-strain relationship. Upon the removal of stress, the elastic deformation is recovered, while the plastic deformation remains permanent. If a viscoelastic material is subjected to constant stress, it will exhibit continuous deformation if fluid-like, or deform asymptotically towards a limit if solid-like. The continued deformation under constant stress is known as creep. Conversely, if a viscoelastic material is rapidly deformed and then maintained in a fixed deformed state, the stresses within may remain constant (if elastic) or decrease over time (if fluid-like), ultimately reaching either an isotropic state of stress or an asymptotic limit. This time-dependent stress reduction under constant strain is termed stress relaxation. While previous deformation experiences influence the stresses in both viscoelastic and thixotropic fluids, viscoelastic fluids are uniquely defined by their elasticity, whereas thixotropic fluids are distinguished by the time dependence of their viscosity or yield stress. Creep and stress relaxation are characterized as viscoelastic phenomena because they stem from the material's response to internal friction and viscous effects. The viscoelastic properties of a material lead to damping and energy dissipation under dynamic loading, resulting in a hysteresis loop in the stress-strain relationship. The area within this hysteresis loop represents the energy dissipated during the loading cycle. Likewise, the propagation of sound in liquids and gases reflects an elastic response. Fluids, in general, exhibit both viscous and elastic character, and their resulting behavior is deemed viscoelastic. Typically, however, elastic deformations are of a significantly smaller order than the viscous deformations.

Constitutive models that quantitatively characterise viscoelastic fluid behaviour are typically expressed either by differential equations or integral representations. These models are frequently articulated through mechanical analogies. The Maxwell model, Kelvin-Voigt model, standard linear solid model, and Burgers model depict linear viscoelastic models employed for predicting material behaviour under diverse stress circumstances. Linear viscoelasticity is based on linear response theory, which presumes linearity within the system. This does not suggest a linear correlation among individual variables; more importantly, it indicates governing equations that linearly associate stress and strain, comprising algebraic, differential, and integral forms, or their combi-

nations.

Nonlinear constitutive models for viscoelasticity encompass the second-order fluid theory, the upper-convected Maxwell theory, the Oldroyd-B theory, the Wagner model, and Prony series. These models may represent more intricate phenomena displayed by fluids, encompassing time-dependent behaviour and nonlinear correlations between stress and strain.

2.4 Magnetorheological Fluids

Magnetorheological (MR) fluids [93] constitute a significant category of functional or "smart" materials, distinguished by rheological properties that can be precisely, rapidly, and reversibly controlled via an external magnetic field. Fundamentally, they are suspensions composed of micron-sized, magnetically permeable particles (typically carbonyl iron powder) dispersed within a non-magnetic carrier liquid, such as mineral, synthetic, or silicone oil [94]. Additives are commonly incorporated to enhance sedimentation stability, reduce abrasive wear, and prevent irreversible particle agglomeration. In the quiescent state, absent an applied magnetic field, MR fluids generally exhibit low viscosity, behaving much like their base carrier fluid. However, upon the application of a magnetic field, the suspended particles acquire magnetic dipole moments and rapidly align themselves, forming fibrous or columnar structures oriented parallel to the magnetic flux lines. These particle structures span the gap containing the fluid, significantly increasing the resistance to flow or deformation, particularly perpendicular to the field direction [95]. This phenomenon results in a dramatic and near-instantaneous transition (occurring within milliseconds) from a relatively low-viscosity, liquid-like state to a semi-solid state. Critically, this transition is characterized by the development of a substantial yield stress, causing the fluid to behave as a viscoplastic material (often approximated by Bingham or Herschel-Bulkley models) while the field is active. The magnitude of this yield stress, and consequently the static and dynamic resistance of the fluid, can be continuously and precisely modulated by adjusting the strength of the applied magnetic field. This field-induced change is fully reversible, with the fluid returning to its low-viscosity state almost immediately upon removal of the magnetic field.

2.5 Applications of non-Newtonian rheology

The departure of non-Newtonian fluids from the simplicity of Newtonian behavior grants them a significant presence across a diverse tapestry of natural phenomena and industrial processes. The interplay between shear stress and viscosity, deviating from

the linear norm, manifests in many essential applications where controlled flow and deformation are highly necessary. In this section, previously mentioned applications that depend on non-Newtonian fluids, are described.

2.5.1 Coatings and paints

Paints and coatings exemplify the intentional engineering of rheology for enhance of performance [96]. The main requirements appear contradictory: the coating should flow easily during application (e.g., brushing, rolling, or spraying) for smooth coverage and good surface wetting, but it must also resist dripping or sagging right after application, particularly on vertical surfaces. Additionally, paints require adequate storage stability to avoid the settling of pigments and fillers over time. These functions are mainly realised through shear-thinning behaviour, often alongside thixotropy [97]. The process generates high-shear rates from the brush or roller, leading to a reduction in paint viscosity. The thinning effect results from the breakdown of temporary structures in the paint (polymer chains and pigment agglomerates). Upon removal of the shear force, the internal structure reforms, leading to a rapid increase in viscosity to inhibit sagging and dripping. Thixotropy enables a time-dependent recovery of viscosity, facilitating initial flow and levelling before viscosity increases. The rheological profile of paint is controlled by additives or modifiers for balancing ease of application, film build, stability, and resistance to defects such as sagging and spattering.

2.5.2 Civil engineering

Fresh concrete, a blend of cement, water, aggregates, and sometimes chemical admixtures, requires specific rheological properties for effective construction [98]. Key performance attributes include workability, which refers to the ease of mixing, transporting, placing into formwork, consolidating, and finishing concrete. Stability is crucial, as it denotes the concrete's capacity to maintain homogeneity and resist segregation of coarse aggregates and bleeding of water during handling and after placement while still plastic. Inadequate rheology may result in defects such as honeycombing, voids, and weak interfaces, undermining the strength, durability, and quality of hardened concrete [99]. Fresh concrete exhibits complex flow behaviour as it consists of a dense particle suspension with a broad size distribution within a fluid matrix (cement paste). Its rheology is often approximated by the Bingham plastic model. A sufficient yield stress stops settling under gravity and aids in preserving the shape post-placement. Plastic viscosity determines flow resistance after surpassing yield stress. It affects the flow of concrete during placement, its capacity to fill formwork, and the ease of surface finishing. Lower plastic viscosity typically facilitates flow and decreases pumping pressure;

however, excessively low levels may worsen segregation. High plastic viscosity complicates placement and consolidation, potentially trapping air bubbles and impacting final quality. Thixotropy impacts concrete behaviour by influencing workability retention and structural development at rest. Controlling yield stress and plastic viscosity via mix design, such as adjusting water-cement ratios, aggregate grading, and chemical admixtures, is crucial for balancing flowability and stability.

2.5.3 Food processing and personal-care products

Controlling rheological properties is crucial for effective food manufacturing and development of personal-care products. Food products are complex mixtures (suspensions, emulsions, and solutions of large molecules like proteins and polysaccharides). Shampoos, conditioners, body washes, lotions, and creams are typically shear-thinning (pseudoplastic). Shear forces, such as pumping and mixing, reduce the viscosity of sauces, dressings, purees, and products like ketchup, aiding in processing and dispensing. They regain higher viscosity at rest, ensuring thickness and preventing sedimentation or phase separation during storage. Yield stress, found in Bingham plastics and Herschel-Bulkley fluids, is crucial for products requiring shape retention, including frostings, mayonnaise, certain cheeses, and thick pastes [100]. The yield stress inhibits flow under gravity, enabling products to retain texture and structure, such as maintaining peaks on a cake or remaining in place when spread. Thixotropic agents form a weak gel at rest, stabilising the product while easily breaking down when stirred or consumed, enhancing mouthfeel. Viscoelasticity also significantly influences creaminess, springiness, and chewiness in various products, including dairy, sauces, doughs, and gels [101]. Processing operations (pumping, mixing, extrusion, and filling) are significantly affected by the non-Newtonian rheology. Non-thermal processing technologies, such as high-pressure processing and pulsed electric fields, aim to maintain the nutritional, sensory, and rheological properties of heat-sensitive food materials that are often changed by traditional thermal methods.

2.5.4 Drilling and extraction

Drilling fluids serve essential roles in the oil and gas industry during well drilling. These tasks involve transporting rock cuttings from the drill bit to the surface, lubricating and cooling the drill bit and string, maintaining hydrostatic pressure to prevent formation fluid influx, stabilising the wellbore, and minimising fluid loss into permeable formations. Drilling fluids are designed to show Bingham plastic (or Herschel-Bulkley) properties, along with shear-thinning and thixotropic traits. When fluid circulation halts temporarily, the fluid must suspend cuttings to prevent settling at the wellbore's

bottom, which may lead to issues such as pipe sticking. The yield stress allows the fluid to act as a weak solid under the low gravitational stress on the cuttings when static. Shear-thinning behaviour is crucial for effective circulation. Fluid in the drill pipe and annulus undergoes moderate to high shear rates during pumping and flow. The capacity to thin in these conditions decreases pumping pressure, reduces energy use, and lessens equipment wear. Lower viscosity at elevated shear rates enhances hole cleaning by enabling turbulent flow regimes that effectively lift cuttings. When left static, the fluid develops a gel structure over time, improving its capacity to suspend cuttings and weighting materials. The gel structure must quickly disintegrate upon the resumption of circulation, facilitating fluid flow. This behaviour over time is typical of thixotropy. Characterising and modelling drilling fluid rheology with models such as Bingham plastic, Power Law, or Herschel-Bulkley is essential for predicting hydraulic performance, optimising cuttings transport, calculating pressure losses, and managing filter cake formation in permeable formations. The rheological properties depend on downhole conditions, as temperature and pressure can significantly affect viscosity and yield stress, along with contamination from drilled solids or formation fluids, necessitating careful monitoring and maintenance of the mud system. The interaction of yield stress, shear thinning, and thixotropy, adapted to drilling conditions, highlights the importance of non-Newtonian fluid mechanics in effective and economical drilling.

2.5.5 Additive manufacturing

Additive Manufacturing (AM), commonly known as 3D printing, inherently involves the controlled deposition and subsequent solidification or curing of materials. 3D printing processes have been optimized and new materials are being explored for extrusion-based processes [102]. Understanding the rheology and impact on the entire process is crucial for improving printing quality. In general, the material's rheological profile must satisfy a set of criteria simultaneously [103]. Shear-thinning behavior, for example, allows materials to be easily forced through fine print nozzles (experiencing high shear) while possessing sufficient viscosity at rest (low shear) to maintain the deposited shape and prevent sagging or spreading [104, 105]. The optimization of printing speed, extrusion temperature, and nozzle design leads to improved manufacturing efficiency, reduced material waste, minimization of print defects, and superior mechanical and functional properties in the final parts [106]. Hydrogels, which are three-dimensional networks of hydrophilic polymers capable of retaining large quantities of water, are extensively utilized in bioprinting due to their inherent biocompatibility, tunable properties, and ability to mimic the native extracellular matrix (ECM) of tissues [104, 107]. Direct Ink Writing (DIW), also known as Robocasting, is a prominent extrusion-based AM technique specifically adapted for fabricating dense or porous ceramic components with

complex three-dimensional architectures [108]. Polymer composite inks for AM involve the dispersion of functional filler particles within a polymer matrix. These inks are designed to combine the processability of polymers with the specific functionalities imparted by the fillers, such as enhanced mechanical strength, electrical conductivity, bioactivity, or thermal properties [103, 92]. 3D Food Printing (3DFP) is an emerging application of AM that offers the potential for personalized nutrition, the creation of intricate food designs, and the innovative use of alternative protein sources and food industry by-products. Extrusion-based printing is the most common modality for 3DFP, utilizing a wide variety of edible pastes and hydrocolloid-based formulations.

2.5.6 Biological Systems

The complex composition of biological fluids often leads to non-linear rheological behavior that is essential for physiological processes. Blood, a suspension of red blood cells, white blood cells, and platelets in plasma (which itself contains proteins and other macromolecules), is a quintessential example of a non-Newtonian fluid in biology and hemorheology. Its most prominent non-Newtonian characteristic is shear thinning of blood, which is advantageous for efficient circulation. Blood also exhibits viscoelastic and thixotropic properties, particularly related to red-blood-cells deformation and aggregation/disaggregation dynamics [109, 110, 111, 112, 113]. Synovial fluid is the viscous fluid found within the cavities of synovial joints, and its lubricating and shock-absorbing stem from complex rheology, primarily its viscoelasticity [101]. In degenerative joint diseases, altered rheological properties (reduced viscosity and elasticity) impair the fluid's lubricating and shock-absorbing capabilities contributing to joint pain, stiffness, and further cartilage degradation [114], so gels may be injected into the joint cavity to restore the viscoelastic properties of the synovial fluid.

2.5.7 Other applications

Shear thickening fluids enhance protective materials, especially flexible body armour. The core concept is based on the fluid's dilatant property, which allows it to quickly shift from a low-viscosity liquid to a high-viscosity, near-solid state under sudden, high-shear-rate impact [115]. Under typical conditions or low-speed movements, the armour retains its fluidity, enabling it to be flexible and comfortable. In milliseconds, it solidifies locally, and the hardened fluid boosts the stiffness and energy absorption of Kevlar fabric, improving penetration resistance and distributing impact energy over a wider area. Non-Newtonian fluids provide innovative mechanisms for damping unwanted vibrations in mechanical systems, over traditional viscous dampers. Both shear thickening and magnetorheological fluids are actively explored [100]. Fluids are used in

2 Non-Newtonian fluids

damping systems due to their ability to increase resistance under dynamic loading. Recent theoretical and experimental work has also investigated the use of non-Newtonian fluids sandwiched between layers in flexible laminates for impact protection, relevant to applications like smartphone display glass [116]. MR fluids stand out as highly versatile "smart" materials, enabling the development of adaptive mechanical systems where performance can be actively controlled in real-time [117]. One of the most successful application areas for MR fluids is in semi-active dampers [118], as they offer the reliability of passive systems combined with the adaptability approaching that of fully active systems. MR fluids can also be used to create controllable clutches and brakes, typically operating in shear mode [118].

3 Mathematical modelling

This chapter outlines the theoretical foundation for simulating the behavior of fluids as both solid and fluid materials, emphasizing the role of constitutive laws in capturing material responses under various conditions. While the core focus of this thesis lies in the numerical modelling of governing equations for non-Newtonian fluids, it is crucial to first distinguish solid and fluid behavior, as well as characterize materials exhibiting properties of both.

3.1 Introduction on modelling

The simulation of fluid dynamics relies on establishing a mathematical framework through constitutive equations, which accurately relate stress, strain rate, and time. These equations, that are underpinned by the fundamental principles of continuum mechanics, provide a means of predicting fluid behavior under varying conditions. Sophisticated numerical simulations, built upon these constitutive relationships, allow for detailed insight into intricate flow phenomena, which informs the design and optimization of efficient engineering systems. The selection of appropriate constitutive equations requires careful consideration, as no single model can universally describe the behavior of all fluids across all flow regimes. Each constitutive model possesses a limited range of applicability, accurately capturing the essential features of a specific flow field.

Continuum mechanics provides a theoretical foundation for analyzing matter regardless of its phase or structure. Material constitutive equations are, therefore, used to characterize the macroscopic properties of solids, liquids, and gases. These constitutive equations serve as macromechanical models, representing real-world material behavior at a scale significantly larger than individual atoms or molecules. A classic example is Hooke's law, which provides a foundational constitutive relationship for elastic solids, linearly relating stress and strain. The continuity assumption, a cornerstone of continuum mechanics, idealizes fluids as continuous media, even though they are composed of discrete molecules. This assumption allows for the description of fluid properties, representing average values of molecular characteristics, as continuously varying from

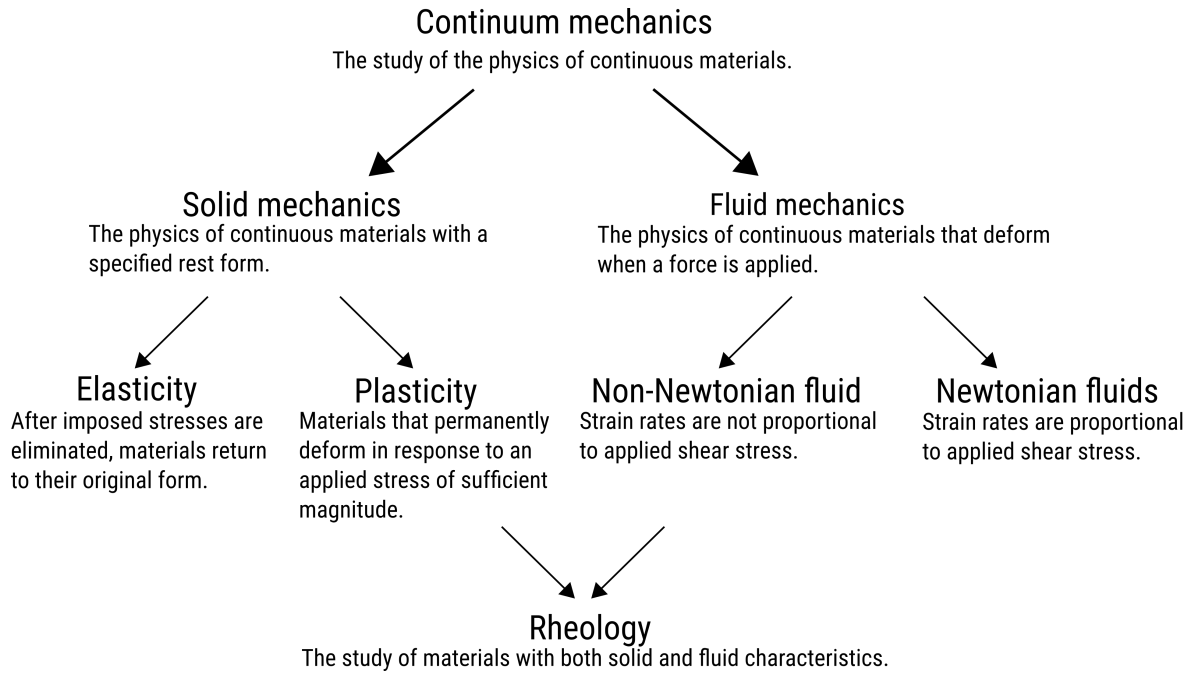


Figure 3.1: Terminology connecting classifications within continuum mechanics and rheology.

point to point within the fluid. This simplification enables the effective use of differential calculus to model fluid behavior. Specifically, the continuum assumption states that macroscopic properties such as density, pressure, temperature, and velocity can be accurately characterized within infinitesimal control volumes.

The diagram shown in Figure 3.1 illustrates the hierarchical structure of the relevant terminology, beginning with its broad definition as the study of the physics of continuous materials. Continuum mechanics branches into solid mechanics, focusing on materials with a defined rest form, and fluid mechanics, which concerns materials that deform under applied force. Solid mechanics further divides into elasticity, where materials return to their original form after stress removal, and plasticity, where materials undergo permanent deformation under sufficient stress. Plastic deformation is defined as irreversible deformation under sustained stress, and creep is characterized by time-dependent deformation under constant stress. As an example among many others, steel under elevated temperatures (above 400 °C) can undergo creep, while geological processes can induce substantial deformation in rocks like granite over extended timescales. Fluid mechanics then becomes the study of the mechanical properties exhibited by continuous flow. It encompasses both Newtonian fluids, characterized by a linear relationship between strain rate and applied shear stress, and non-Newtonian fluids, where this linear relationship does not hold.

Rheology is therefore the base encompassing a broader understanding of material behavior, i.e. the study of materials exhibiting both solid and fluid characteristics.

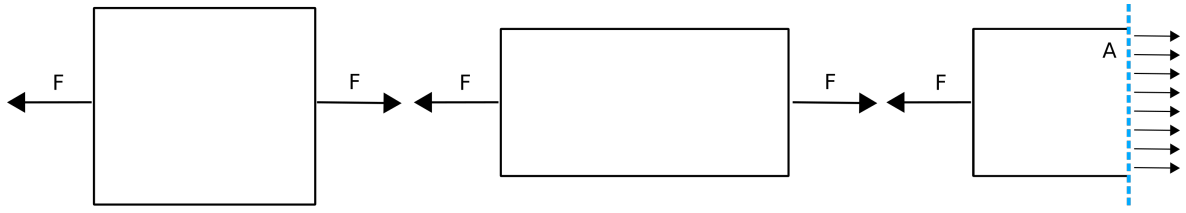


Figure 3.2: Normal stress definition.

3.2 Stresses in the material

Normal stress

Stress and strain are used to quantify a deformable body's internal response to external forces. Consider a uniaxial loading scenario, as depicted in Figure 3.2, where an external force is applied along a single axis, resulting in tensile loading. This applied force induces an internal reaction within the material, resisting the external load and striving to maintain a state of static equilibrium. The magnitude of the internally generated resistive force is, by Newton's third law, equal to the magnitude of the externally applied force. However, it is more physically informative to consider the distribution of these internal forces across the material's cross-sectional area, i.e. the concept of stress.

Stress represents the intensity of these internal forces acting over an infinitesimal area. Specifically, the component of internal force acting perpendicularly to a given cross-section is termed the normal stress typically measured in Pascals, and is defined mathematically as:

$$\sigma = \frac{F_n}{A}, \quad (3.1)$$

where F_n represents the magnitude of the internal force acting normal to the cross-section, measured in Newtons (N), and A represents the area of the cross-section perpendicular to the applied force, measured in square meters (m^2). Normal stress can be either tensile or compressive in nature. Tensile stress denotes a state of tension, where the material is being pulled or stretched, resulting in an increase in length along the loading axis. Conversely, compressive stress corresponds to a state of compression, where the material is being pushed or shortened, resulting in a decrease in length along the loading axis.

Strain

Strain is a dimensionless quantity that quantifies the deformation of a material in response to applied stress. Specifically, normal strain ε describes the change in length of a body along a particular axis, relative to its original length. For a slender bar

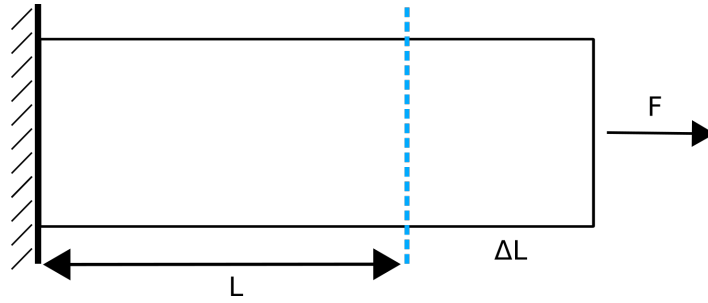


Figure 3.3: Schematic for defining the normal strain in a console.

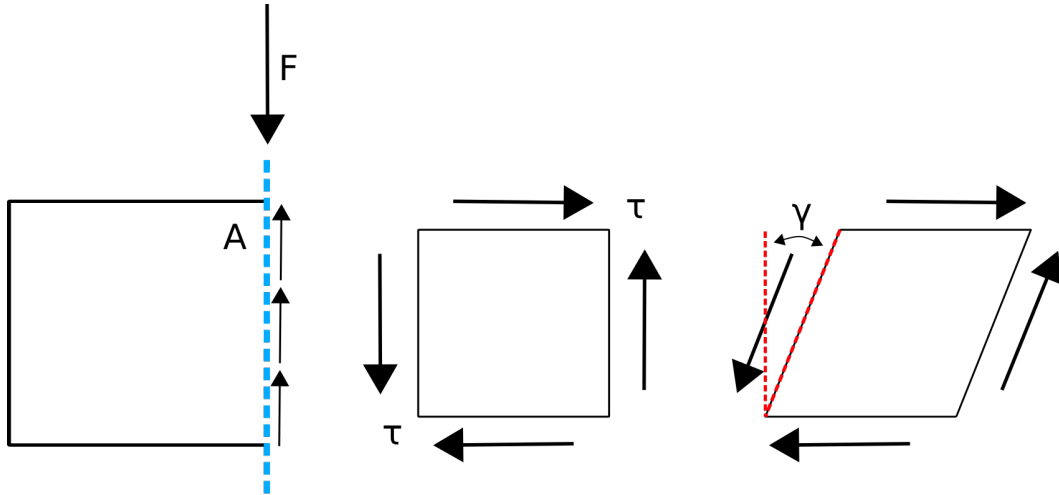


Figure 3.4: Shear stress definition.

subjected to uniaxial loading, as illustrated in Figure 3.3, the normal strain ε can be calculated as:

$$\varepsilon = \frac{\Delta L}{L}, \quad (3.2)$$

where L represents the original length of the bar before the application of the force, measured in meters (m), and ΔL represents the change in length of the bar due to the applied force, also measured in meters (m). Since strain is a ratio of two lengths, it is dimensionless and often expressed as a decimal or a percentage. Similar to stress, normal strain can be either tensile or compressive. Tensile strain indicates an elongation ($\Delta L > 0$) of the material, while compressive strain indicates a shortening or compression ($\Delta L < 0$) of the material.

Shear stress

Shear stress represents a fundamentally distinct type of stress compared to normal stress. It arises when a force is applied parallel to a surface or cross-section of a body, in contrast to the perpendicular application in normal stress. This type of loading generates internal forces within the material that are parallel to the cross-section,

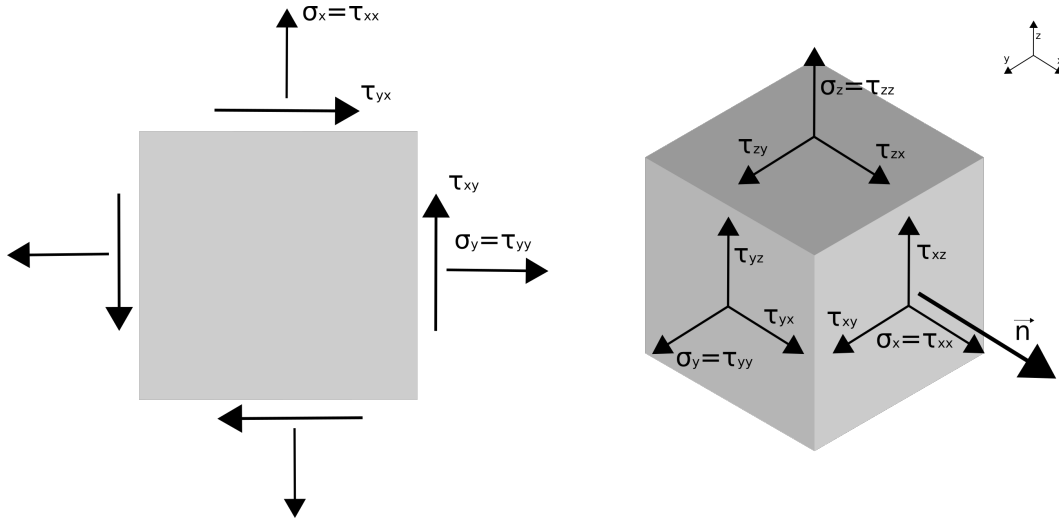


Figure 3.5: Infinitesimal stress–element definition in two and three dimensions.

termed shear forces. The shear stress, τ typically measured in Pascals, is quantified as the force acting tangentially per unit area:

$$\tau = \frac{F_t}{A}. \quad (3.3)$$

where F_t represents the magnitude of the internal force acting tangential to the cross-section. Figure 3.4 illustrates shear stress acting on an infinitesimal element within a deformable body. For this element to remain in static equilibrium, shear stresses must act on opposing faces with equal magnitude but opposite direction. Furthermore, to ensure rotational equilibrium, two additional shear stresses of equal magnitude τ are induced on the remaining two faces, defining a state of pure shear.

Shear strain

The application of shear stress causes a deformation of the material as shown in Figure 3.4, resulting in shear strain. This shear strain γ is defined as the change in angle within the material, as depicted in Figure 3.4, and is measured in radians. In analogy with Hooke’s law for normal stress, the shear stress and shear strain are related through the shear modulus G :

$$\tau = G\gamma, \quad (3.4)$$

where G denotes the shear modulus of the material, representing its resistance to shear deformation.

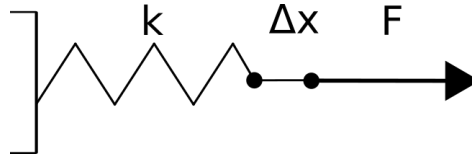


Figure 3.6: Hooke's law states that the force F necessary to generate an elongation Δx in a spring with a mechanical constant k .

Cauchy stress tensor

At any given point within a deformable body, a comprehensive description of the stress state considers both normal and shear stress components, acting on various planes passing through that point. The magnitudes of these stress components vary depending on the orientation of the plane under consideration. Figure 3.5 illustrates the distribution of stress components on a representative element in both two and three dimensions. To capture this complete stress state, the Cauchy stress tensor, denoted as $\boldsymbol{\sigma}$, is employed. The stress tensor is a second-order tensor that encapsulates all normal and shear stress components acting on a material element, providing a coordinate-independent representation of the stress state. The general form of the Cauchy stress tensor is given as:

$$\boldsymbol{\sigma} = \begin{bmatrix} \sigma_x & \tau_{xy} & \tau_{xz} \\ \tau_{yx} & \sigma_y & \tau_{yz} \\ \tau_{zx} & \tau_{zy} & \sigma_z \end{bmatrix} \equiv \begin{bmatrix} \tau_{xx} & \tau_{xy} & \tau_{xz} \\ \tau_{yx} & \tau_{yy} & \tau_{yz} \\ \tau_{zx} & \tau_{zy} & \tau_{zz} \end{bmatrix}, \quad (3.5)$$

where τ with subscripts define both normal and shear stresses, where the subscripts denote the stress plane.

3.3 Constitutive laws

3.3.1 Linear elasticity

As already noted, constitutive equations are mathematical expressions that describe the macroscopic mechanical behavior of materials under various external influences: applied loads, temperature changes, and pore pressure variations. These relationships are essential for predicting the deformation, stress state, and long-term responses. The selection of an appropriate constitutive equation is critical and depends on the material properties, the anticipated strain and stress magnitudes, and the loading rate. Constitutive models vary in complexity and applicability, ranging from simple linear elastic models to advanced nonlinear and time-dependent formulations.

Linear elasticity, described by Hooke's Law, serves as the foundational starting point for understanding solid mechanics. Linear elasticity represents the simplest constitutive relationship, establishing a linear connection between stress and strain through

constant coefficients. This relationship is analogous to the behavior of a spring, as illustrated in Figure 3.6, where the applied force F is directly proportional to the resulting displacement Δx :

$$F = k \Delta x, \quad (3.6)$$

where F is the applied force in Newtons, k is the spring stiffness in N/m, and Δx is the displacement in metres. For one-dimensional problems, Hooke's Law is typically expressed in terms of stress and strain:

$$\sigma = E \varepsilon, \quad (3.7)$$

where ε is the normal strain, and E represents Young's modulus in Pascals, i.e. the material property that quantifies stiffness.

While linear elasticity provides a fundamental and often sufficient framework for understanding the behavior of many solid materials under small deformations, its assumptions impose limitations. Primarily, it assumes a proportional relationship between stress and strain (i.e. the Hooke's law) and that the material perfectly returns to its original shape once the load is removed. Many real materials, especially when subjected to larger strains or specific loading conditions, deviate significantly from this idealized linear response. The modeling of nonlinear behavior can be approached in several ways, depending on the source and nature of the nonlinearity.

Even if deformations are geometrically small, the material's stress-strain curve might be nonlinear. Instead of a constant elastic modulus (e.g., Young's modulus, E), the material exhibits a strain-dependent stiffness. This can be modeled by polynomial, exponential, or power-law functions to fit experimental stress-strain data. Moreover, when deformations are large, then small strain assumption ($\varepsilon \ll 1$) is no longer valid. Changes in the geometry of the body significantly influence its mechanical response. Modeling this requires employing more complex strain measure, i.e. nonlinear functions of the displacement gradients. The equations of equilibrium and compatibility also become nonlinear due to these finite strain definitions and the need to account for the deformed configuration of the body (e.g., using Lagrangian formulations).

3.3.2 Equilibrium in general

Within a continuum body that is under static equilibrium, the components of the Cauchy stress tensor at each material point must satisfy the equilibrium equations, which are derived from the principle of conservation of linear momentum. This condition ensures that the net force acting on any infinitesimal volume element within the body is zero, resulting in no acceleration ($ma = 0$).

3 Mathematical modelling

To express this principle mathematically, consider the force summation on an infinitesimally small cubic element with its dimensions Δx , Δy , and Δz , as depicted in Figure 3.7. As the dimensions approach zero ($\Delta x \rightarrow 0$, $\Delta y \rightarrow 0$, $\Delta z \rightarrow 0$), the stress components acting on the element can be approximated using the Taylor-series expansions. In addition to the surface forces represented by the stress tensor, a body-force term must be considered. This term accounts for forces acting on the entire volume element, such as the Earth gravity. By summing up the forces in x direction $\sum F_x = ma = 0$ the following expression is obtained:

$$\sum F_x = (\tau_{xx} + \frac{\partial \tau_{xx}}{\partial x} \Delta x - \tau_{xx}) \Delta y \Delta z + (\tau_{yx} + \frac{\partial \tau_{yx}}{\partial y} \Delta y - \tau_{yx}) \Delta x \Delta z + (\tau_{zx} + \frac{\partial \tau_{zx}}{\partial z} \Delta z - \tau_{zx}) \Delta x \Delta y, \quad (3.8)$$

$$\sum F_x = (\frac{\partial \tau_{xx}}{\partial x} + \frac{\partial \tau_{yx}}{\partial y} + \frac{\partial \tau_{zx}}{\partial z}) \Delta x \Delta y \Delta z - b_x = 0, \quad (3.9)$$

Considering that $\Delta x \Delta y \Delta z$ represents the partial volume of the body:

$$\Delta V = \Delta x \Delta y \Delta z = \frac{m}{\rho},$$

then the sum of the forces in x direction $\sum F_x = 0$ can be expressed as follows:

$$\sum F_x = \frac{\partial \tau_{xx}}{\partial x} + \frac{\partial \tau_{yx}}{\partial y} + \frac{\partial \tau_{zx}}{\partial z} - b_x \rho = 0. \quad (3.10)$$

By summing up all the forces in all directions, i.e.:

$$\sum F_x = \sum F_y = \sum F_z = 0,$$

the general Cauchy's equilibrium equations are defined, which can be expressed in a shorter way by using the index notation as follows:

$$\frac{\partial \tau_{ij}}{\partial x_j} + b_i \rho = 0. \quad (3.11)$$

Finally, the same can be written in the vector form:

$$\nabla \cdot \boldsymbol{\tau} + b \rho = 0. \quad (3.12)$$

3.3.3 Stress tensor in fluids

Similar to solids, the concept of stress is crucial for describing the internal forces within a fluid. When a fluid flows and/or is subjected to external forces, internal stresses

3 Mathematical modelling

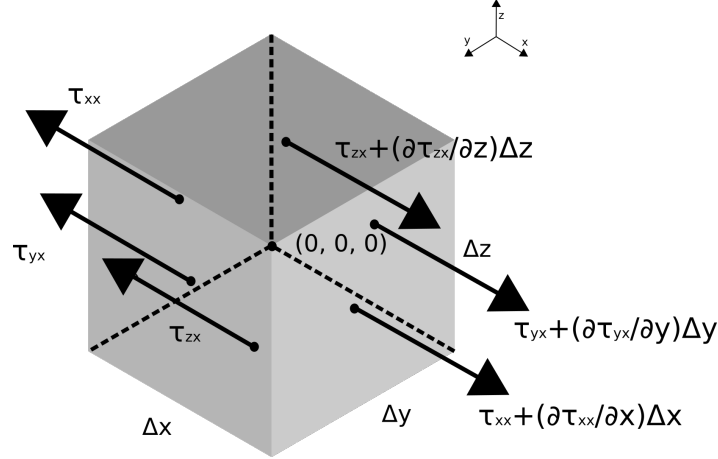


Figure 3.7: Equilibrium of forces in direction x .

develop. The Cauchy stress tensor provides a complete description of the state of stress at any point within the fluid. It relates the traction vector (force per unit area) \mathbf{t} acting on an arbitrary internal surface to the orientation of that surface, defined by its unit normal vector \mathbf{n} :

$$\mathbf{t} = \boldsymbol{\tau} \cdot \mathbf{n}. \quad (3.13)$$

The relationship holds true for fluids just as it does for solids, but the physical origins and constitutive relations for the stress tensor components differ. In fluids, it is conventional and physically insightful to decompose the stress tensor into two parts:

- *Isotropic pressure* p , which is a scalar that represents the hydrostatic and hydrodynamic pressure that acts equally in all directions (normal to any surface), and is present even in a fluid at rest. By convention, the pressure is taken as positive in compression.
- *Viscous-stress tensor* $\boldsymbol{\tau}$, which represents fluid's internal resistance to deformation, i.e. the shear stresses and the non-isotropic components of normal stresses. For a fluid at rest, the viscous stress tensor is zero.

Therefore, the total stress tensor in a fluid $\boldsymbol{\sigma}$ can be defined:

$$\boldsymbol{\sigma} = -p\mathbf{I} + \boldsymbol{\tau}, \quad (3.14)$$

where \mathbf{I} is the identity tensor, p is the pressure, and $\boldsymbol{\tau}$ is the viscous-stress tensor of the fluid. In the following sections, it will be described how the viscous-stress tensor is defined for Newtonian and non-Newtonian fluids, i.e. how complex relationship between $\boldsymbol{\tau}$ and the rate of deformation represents shear-thinning, shear-thickening, yield stress, and viscoelasticity effects.

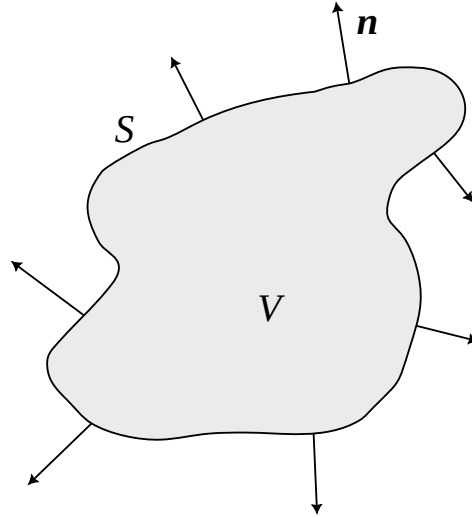


Figure 3.8: An arbitrary fluid volume V enclosed by a surface S that is represented by its normal vectors, \mathbf{n} .

3.3.4 Equilibrium for fluids

In order to give physical meaning to the “divergence of the stress tensor” in equation (3.12), the forces from the infinitesimal cube element in Figure 3.7 are considered in the context of the domain that represents an arbitrary volume shown in Figure 3.8. We consider the forces acting on an arbitrary fluid volume V enclosed by a surface S that is represented by its normal vectors, \mathbf{n} . The net surface force \mathbf{F}_S acting on this volume due to the stresses at its boundary is given by the integral of the traction vector over the surface:

$$\mathbf{F}_S = \int_S \mathbf{t} dS = \int_S (\boldsymbol{\sigma} \cdot \mathbf{n}) dS. \quad (3.15)$$

The divergence theorem (also known as Gauss’s theorem or Ostrogradsky’s theorem) provides a fundamental mathematical tool to relate this surface integral to a volume integral. The theorem states that for a continuously differentiable tensor field $\boldsymbol{\sigma}$, the integral of its normal component over a closed surface S is equal to the integral of its divergence over the volume V enclosed by S :

$$\int_S (\boldsymbol{\sigma} \cdot \mathbf{n}) dS = \int_V (\nabla \cdot \boldsymbol{\sigma}) dV \quad (3.16)$$

Applying this to the surface–force integral equation (3.15):

$$\mathbf{F}_S = \int_V (\nabla \cdot \boldsymbol{\sigma}) dV. \quad (3.17)$$

This indicates that the term $\nabla \cdot \boldsymbol{\sigma}$, i.e. “the divergence of the stress tensor”, represents the net surface force per unit volume acting on the fluid.

By combining the net–surface force per unit volume (3.17) with body forces per unit

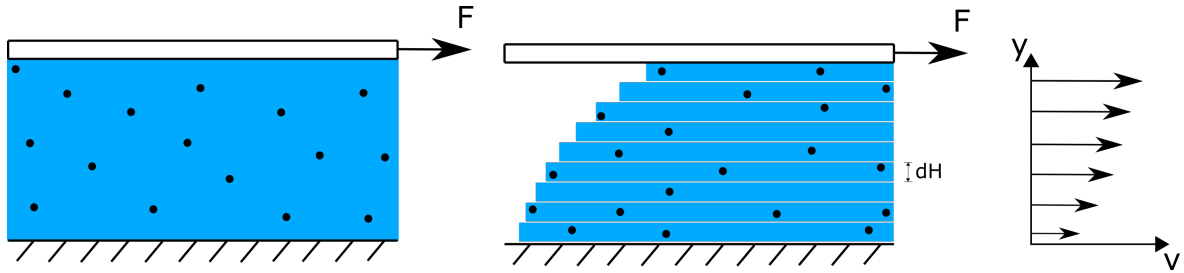


Figure 3.9: Schematic for defining the viscosity, shown in a simple shear flow.

volume \mathbf{f}_b (e.g. effect of gravity) and the rate of change of momentum per unit volume $\rho Du/Dt$, we arrive at Cauchy's equation of motion for a continuum, which is fundamental to fluid dynamics:

$$\rho \frac{Du}{Dt} = \nabla \cdot \boldsymbol{\sigma} + \mathbf{f}_b.$$

Substituting the decomposition of stress from equation (3.14), the final equation becomes:

$$\rho \frac{Du}{Dt} = -\nabla p + \nabla \boldsymbol{\tau} + \mathbf{f}_b.$$

This equation is the general form of the momentum conservation equation for any fluid. The specific nature of the fluid is encapsulated in the constitutive equation for the viscous-stress tensor.

3.4 Shear stress in fluids

For numerical modelling, accurately representing viscous-stress tensor for non-Newtonian fluids and then solving this system of partial differential equations is the central challenge. Therefore, in this section the explanation of stress-strain relationship and some examples useful in describing the non-Newtonian fluids are explained. It is critical to understand where the viscosity comes from and how the fluid flows.

Viscosity is defined as the resistance to fluid motion (i.e. continuous deformation). The higher the viscosity of the fluid, the greater its resistance to flow and the more difficult it is to travel or be transported from one location to another. Honey, for example, is such a viscous fluid that it sips slowly through a spoon after being removed from the jar. This is primarily due to the high viscosity, which indicates that there is a lot of tension in the surface and therefore a lot of forces acting on it. This means that the molecules move extremely slowly. Water is another example of a low-viscosity fluid because it flows quickly and smoothly.

Figure 3.9 shows two plates with some sort of fluid filled between them. The bottom plate is a solid and static base plate, while the top plate is pushed to the right by force

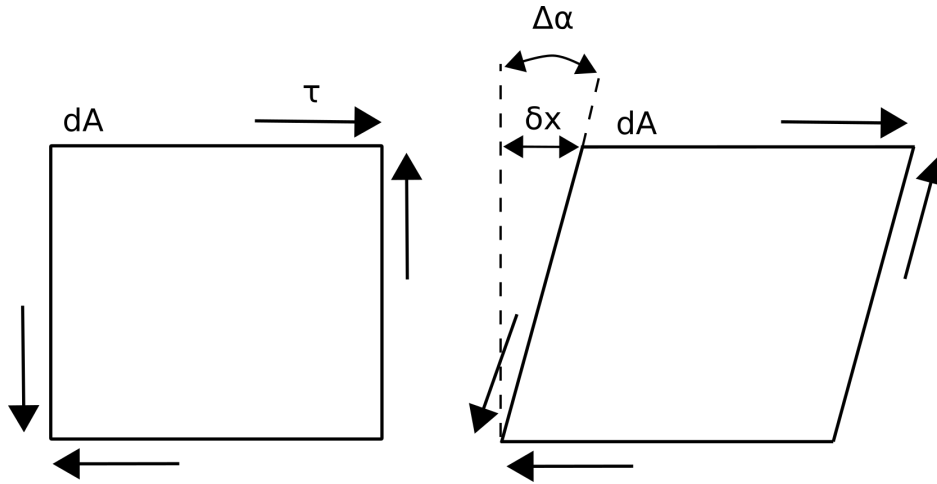


Figure 3.10: The change in fluid element in short period of time defines shear strain.

F . Fluids of all kinds, liquid or gas, with visible molecules, can be used. The fluid will not move in unison with the moving plate, molecules in fluids are not as tightly bound together as in solids. When molecules are moved, they attempt to adhere to the surfaces. A fundamental principle in fluid mechanics is the no-slip boundary condition, which states that fluid in immediate contact with a solid surface moves at the same velocity as the surface. Consequently, the fluid layer in contact with the stationary lower plate will have zero velocity. As the plate moves, the fluid will be displaced in infinitesimal layers and at infinitesimal height. The layers closest to the moving surface will travel much faster than the layers at the bottom. For Newtonian fluids (e.g. water in a pipe), this results in a parabolic velocity profile. Water near the walls tends to adhere to the wall, and the highest velocity occurs in the pipe's center, where there is the least resistance.

In a more formal sense, viscosity can be defined as a contribution to shear stress. Shear stress is caused by transverse planes passing each other, like shown in Figure 3.9. Shear stress at a point on an internal surface within the fluid is defined as the limiting ratio of an infinitesimal tangential force acting over an infinitesimal area element of that surface:

$$\tau = \lim_{\Delta A \rightarrow 0} \frac{\Delta F}{\Delta A} = \frac{dF}{dA}, \quad (3.18)$$

where dF represents the infinitesimal component of force acting parallel (tangential) to the surface element, and dA represents the infinitesimal area of that surface element over which the force dF is distributed.

When shear stress applied to a fluid element causes deformation, as depicted in Figure 3.10, it is characterized by a displacement δx of one layer of fluid relative to an adjacent layer separated by a distance Δy . This displacement results in an angular deformation $\Delta \alpha$, which defines the *shear strain*. For small deformations, which are typically assumed

3 Mathematical modelling

in defining the instantaneous rate of strain, the angle $\Delta\alpha$ is small, allowing for the approximation:

$$\Delta\alpha \approx \tan(\Delta\alpha) = \frac{\delta x}{\Delta y}. \quad (3.19)$$

The displacement δx is directly related to the difference in velocity Δu between these two fluid layers and the time interval Δt , over which the velocity difference happens. Specifically, the displacement can be expressed as:

$$\Delta u \Delta t = \delta x, \quad (3.20)$$

and by substituting equation (3.19) for δx and rearranging equation (3.20) we get the following expression for the rate of shear strain:

$$\frac{\Delta\alpha}{\Delta t} \approx \frac{\Delta u}{\Delta y}. \quad (3.21)$$

In the limit as the time interval approaches zero $\Delta t \rightarrow 0$, this relationship describes the instantaneous *rate of shear strain* (or *shear-strain rate*):

$$\dot{\gamma} = \frac{d\alpha}{dt} = \frac{du}{dy}. \quad (3.22)$$

For many common fluids, known as Newtonian fluids, the shear stress is directly proportional to this rate of shear strain. The constant of proportionality is the dynamic viscosity, μ . This constitutive relationship, defining *shear stress for Newtonian fluids*, is given by:

$$\tau = \mu \frac{du}{dy} = \mu \dot{\gamma}, \quad (3.23)$$

where letter μ represents the dynamic viscosity and has units of $\text{N s/m}^2 = \text{Pa s}$. It's important to recognize that this is an *empirical constitutive model* rather than a fundamental law of nature. It accurately describes the behavior of a specific class of fluids, often termed "simple fluids," which includes common examples like air, water, and many oils, under many flow conditions. The general functional dependence $\tau(\dot{\gamma})$ indicates that shear stress is a function of shear rate, which holds true for both Newtonian and non-Newtonian fluids, though the form of the function differs.

Another important viscous property is the kinematic viscosity, ν . It is defined as the ratio of the dynamic viscosity μ to the fluid density ρ :

$$\nu = \frac{\mu}{\rho}, \quad (3.24)$$

which has units of m^2/s . For a Newtonian fluid, a plot of shear stress (τ) against the

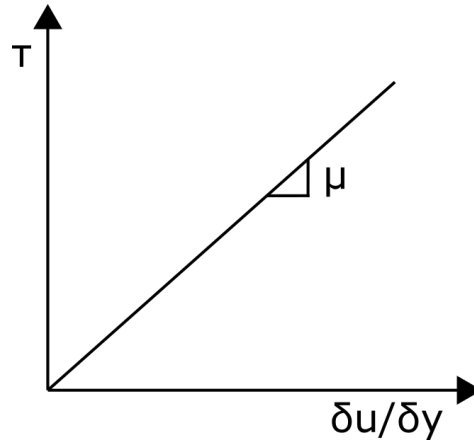


Figure 3.11: The viscosity relationship for a Newtonian fluid.

shear rate ($\dot{\gamma}$) yields a straight line passing through the origin, as illustrated in Figure 3.11. The constant slope of this line represents the fluid's dynamic viscosity, μ . This linear relationship (3.23) is referred to as *Newton's law of viscosity*.

In contrast, when shear stress is plotted against shear rate for non-Newtonian fluids, the resulting curves are non-linear, indicating that their viscosity is not constant but rather depends on the shear rate. For non-Newtonian fluids in simple shear flow, the concept of *apparent viscosity* is introduced, denoted $\eta(\dot{\gamma})$:

$$\eta(\dot{\gamma}) = \frac{\tau}{\dot{\gamma}}. \quad (3.25)$$

The apparent viscosity of a Newtonian fluid is constant and equal to the fluid's Newtonian viscosity, while the apparent viscosity of a non-Newtonian fluid depends on the shear rate. The SI unit for apparent viscosity is Pa·s. From equation 3.25, the shear stress is defined as:

$$\tau = \eta(\dot{\gamma}) \dot{\gamma}. \quad (3.26)$$

Several factors can influence the viscosity (either dynamic or apparent) of a fluid. The properties that may affect viscosity are:

- *Temperature*. It has been found empirically that the viscosity tends to fall with rise of the temperature. For example, for liquids it can be described using Andrade's equation as follows:

$$\eta = B e^{c/T}, \quad (3.27)$$

where T is the absolute temperature, and B and c are empirically determined constants for a given liquid. In the case of the gas state, there is the empirical Sutherland equation found through experiments:

$$\eta = \frac{BT^{3/2}}{T + C}, \quad (3.28)$$

where B and c are empirical constants for the specific gas.

- *Pressure.* For liquids, viscosity generally increases with an increase in pressure, although the effect is often less pronounced than that of temperature at moderate pressures. Under extremely high pressures, many liquids can exhibit substantial increases in viscosity and may even solidify. For gases, viscosity is nearly independent of pressure over a wide range, except at very low (rarefied) or extremely high pressures. The viscosity of an ideal gas is considered to be a function of temperature only.
- *Time of shearing.* As explained in Section 3.4, the viscosity of certain fluids can change over the duration t for which shear is applied, i.e. $\eta(t)$. These fluids are classified as thixotropic if their apparent viscosity decreases over time under constant shear, or rheopectic if it increases over time under constant shear.

3.5 Dimensionless numbers

Dimensionless numbers are invaluable tools in fluid mechanics for characterizing flow regimes, scaling experimental results, and understanding the relative importance of various physical phenomena. In the context of non-Newtonian fluids, particularly viscoelastic materials, Deborah and Weissenberg specific dimensionless numbers are crucial.

3.5.1 Reynolds number

The Reynolds number (Re) is a fundamental dimensionless parameter in fluid mechanics that quantifies the ratio of inertial forces to viscous forces within a fluid flow. It is crucial for predicting flow patterns and determining whether a flow will be laminar (smooth, orderly) or turbulent (chaotic, with eddies and fluctuations). It is generally defined as:

$$Re = \frac{\rho U L}{\mu}, \quad (3.29)$$

where U is a characteristic velocity of the flow (e.g., average velocity in a pipe, free-stream velocity over an object), and L is a characteristic length scale of the flow geometry (e.g., pipe diameter, chord length of an airfoil). The interpretation of the Reynolds number is as follows:

- *Low Re (e.g., $Re < \sim 2000$ for pipe flow of Newtonian fluids).* Viscous forces are dominant. The flow is typically laminar, characterized by smooth, parallel streamlines. Disturbances in the flow are damped out by viscosity.

- *High Re* (e.g., $Re > \sim 4000$ for pipe flow of Newtonian fluids). Inertial forces are dominant. The flow is typically turbulent, characterized by chaotic eddies, mixing, and significant fluctuations in velocity and pressure.
- *Intermediate or transition Re*. The flow may exhibit intermittent bursts of turbulence or be in a transitional state between laminar and turbulent.

3.5.2 Deborah number

The Deborah number (De) is a dimensionless parameter used to characterize the "fluidity" or "solid-like" nature of a material's response under specific flow conditions. It quantifies the ratio of the material's intrinsic characteristic relaxation time (t_c) to the characteristic time scale of the observation or deformation process (t_p):

$$De = \frac{t_c}{t_p}. \quad (3.30)$$

where t_c represents the *relaxation time* of the material that quantifies the time required for the material to adjust or "relax" its internal stresses after a deformation or when subjected to applied stresses. It reflects the material's memory of its past deformation history. t_p represents the observation time or the *characteristic time scale* of the experiment, simulation, or engineering process being considered. The Deborah number effectively compares how quickly a material can respond to changes relative to how quickly those changes are being imposed:

- $De \ll 1$ (*fluid-like behavior*). If the Deborah number is small, it implies either that the material's relaxation time t_c is very short (the material responds almost instantaneously to changes) or that the observation time t_p is very long (the material has ample time to flow and relax). In this regime, the material behaves predominantly like a viscous fluid, and energy imparted during deformation is primarily dissipated as heat.
- $De \gg 1$ (*solid-like behavior*). If the Deborah number is large, it indicates either that the material's relaxation time t_c is very long (the material responds very slowly to changes) or that the observation time t_p is very short (the deformation occurs too rapidly for the material to flow significantly). In this regime, the material behaves more like an elastic solid, and energy imparted during deformation is primarily stored elastically.

3.5.3 Weissenberg number

The Weissenberg number (Wi) is a dimensionless parameter used to characterize viscoelastic fluid flows. It quantifies the relative importance of elastic forces to viscous

3 Mathematical modelling

forces within the fluid under a given deformation rate. The Weissenberg number is typically defined as the product of a characteristic relaxation time of the fluid (λ , often the same or related to t_c used in De) and a characteristic shear rate ($\dot{\gamma}$) of the flow:

$$Wi = \lambda\dot{\gamma}.$$

Alternatively, it can be conceptualized as the ratio of elastic stresses to viscous stresses:

$$Wi = G\frac{\lambda}{\eta}, \quad (3.31)$$

where G is an elastic modulus. Thus, the Weissenberg number assesses the degree of elastic response:

- $Wi \ll 1$ (*viscous-dominated flow*). Elastic effects are negligible, and the fluid behaves primarily like a purely viscous (Newtonian or generalized Newtonian) fluid.
- $Wi \gg 1$ (*elasticity-dominated flow*). Elastic effects are significant and can lead to phenomena not observed in purely viscous flows, such as rod-climbing (the Weissenberg effect), die swell, and flow instabilities.

3.5.4 Bingham number

The Bingham number (Bn) is a dimensionless parameter specifically used to characterize the flow of viscoplastic fluids, such as Bingham plastics or Herschel-Bulkley fluids. These materials exhibit a yield stress (τ_y), meaning they behave like a rigid solid below this stress threshold and flow like a fluid only when the applied stress exceeds it. The Bingham number quantifies the ratio of the yield stress to viscous stress:

$$Bn = \frac{\tau_y L}{\mu_p U} \quad (3.32)$$

where τ_y is the yield stress of the fluid, L is a characteristic length scale (e.g., pipe diameter, channel height), μ_p is the plastic viscosity (the constant viscosity exhibited by a Bingham plastic above its yield stress) and U is a characteristic velocity. The significance of the Bingham number is:

- *Low Bn , viscous forces are dominant compared to the yield stress.* The yielded regions of flow will be extensive, and the unyielded "plug" regions (where the stress is below τ_y) will be small or non-existent. The fluid behaves more like a purely viscous fluid.
- *High Bn , the yield stress is dominant.* The fluid will resist flow significantly, and

large unyielded plug regions will exist. Flow may only occur in limited regions where the local stress exceeds τ_y , or it may not occur at all if the driving forces are insufficient to overcome the yield stress globally.

In numerical simulations of viscoplastic flows, the Bingham number helps to characterize the problem and is essential for implementing constitutive models that incorporate yield stress, often requiring specific numerical techniques to handle the discontinuous nature of the yield stress criterion.

3.6 Navier–Stokes equations

The motion of incompressible fluids, including those exhibiting complex non-Newtonian behaviors such as viscoplasticity and viscoelasticity, is fundamentally governed by the principles of mass and momentum conservation. These principles are mathematically expressed through a generalized form of the Navier–Stokes equations. For an incompressible fluid, these governing equations are presented in a strong vector form suitable for continuum mechanics:

$$\frac{D\mathbf{u}}{Dt} = \frac{1}{\rho} \{-\nabla p + \nabla \cdot \boldsymbol{\tau}_s + \nabla \cdot \boldsymbol{\tau}_p\} + \mathbf{a}_{ext}, \quad (3.33)$$

$$\nabla \cdot \mathbf{u} = 0, \quad (3.34)$$

$$\frac{D\mathbf{x}}{Dt} = \mathbf{u}. \quad (3.35)$$

where ρ is the fluid density, \mathbf{u} is the velocity vector, p is the pressure, \mathbf{x} is the position of the Lagrangian parcel, \mathbf{a}_{ext} is the external–acceleration vector field, $\boldsymbol{\tau}_s$ is the solvent–diffusion stress tensor, and $\boldsymbol{\tau}_p$ is the extra–stress polymeric tensor, and the advective Lagrangian derivative is denoted as D/Dt . These equations form a system of coupled, nonlinear partial differential equations (PDEs), which are dependent on time ($t \geq 0$) and space (in the fluid domain Ω), even the equations do not specify it explicitly. From a Lagrangian perspective, the momentum equation (3.33) describes the acceleration experienced by an individual fluid parcel. This parcel advects along its trajectory governed by the local velocity field as described by the kinematic condition (3.35), while the movement is incompressible due to the continuity constraint (3.34).

Equation (3.33) splits the extra stress into the viscous–solvent contribution, $\boldsymbol{\tau}_s$, and the (viscoelastic) polymer stress contribution, $\boldsymbol{\tau}_p$. This decomposition can be extended to the total effective viscosity of the fluid if a generalized Newtonian framework is considered. Consequently, the total dynamic viscosity of the fluid might be conceptualized

as a sum of solvent and polymeric contributions:

$$\mu = \mu_s + \mu_p, \quad (3.36)$$

where μ_s is the dynamic viscosity of the solvent and μ_p is the dynamic viscosity of the polymeric part. It should be noted that for viscoelastic fluids, the polymeric stress $\boldsymbol{\tau}_p$ (containing its viscosity) is typically defined by its own evolution equation rather than a simple viscosity. In the following subsections, the definition of solvent and polymeric stresses are defined.

3.6.1 Diffusion of constant-viscosity flows

The contribution to the total stress arising from the solvent's viscous properties (often termed solvent diffusion in some contexts) is typically modeled using a symmetric stress tensor linearly proportional to the rate of strain:

$$\boldsymbol{\tau}_s = 2\mu_s (\mathbf{E}) \mathbf{E}, \quad (3.37)$$

where \mathbf{E} is the *rate of strain*, i.e. symmetrized gradient of the velocity:

$$\mathbf{E} = \frac{1}{2} \left[\nabla \mathbf{u} + (\nabla \mathbf{u})^\top \right], \quad (3.38)$$

which also known as the rate of deformation tensor. In the momentum equation (3.33), the force per unit volume (i.e. the acceleration) due to this solvent stress is given by its divergence, $\nabla \cdot \boldsymbol{\tau}_s / \rho$. The form of this divergence term depends on whether the solvent viscosity is constant or variable.

To calculate $\nabla \cdot \boldsymbol{\tau}_s = \nabla \cdot [2\mu_s (\mathbf{E}) \mathbf{E}]$, let's define the "divergence of the scalar–tensor product" identity for a tensor \mathbf{T} and scalar ϕ as:

$$\nabla \cdot (\phi \mathbf{T}) = \phi \nabla \cdot \mathbf{T} + \mathbf{T} \nabla \phi. \quad (3.39)$$

Therefore, the divergence of the shear stress $\boldsymbol{\tau}_s$ may be expanded by applying the identity (3.39) to equation (3.37):

$$\begin{aligned} \nabla \cdot \boldsymbol{\tau}_s &= \nabla \cdot (2\mu_s \mathbf{E}) \\ &= 2\mu_s \nabla \cdot \mathbf{E} + 2\mathbf{E} \nabla \mu_s. \end{aligned} \quad (3.40)$$

Equation (3.38) is substituted into equation (3.40) to obtain the following:

$$\begin{aligned}
 \nabla \cdot \boldsymbol{\tau}_s &= \mu_s \nabla \cdot \left[\nabla \mathbf{u} + (\nabla \mathbf{u})^\top \right] + 2\mathbf{E} \nabla \mu_s \\
 &= \mu_s \nabla^2 \mathbf{u} + \cancel{\mu_s \nabla \cdot (\nabla \mathbf{u})^\top}^{\mathbf{0}} + 2\mathbf{E} \nabla \mu_s \\
 &= \mu_s \nabla^2 \mathbf{u} + 2\mathbf{E} \nabla \mu_s.
 \end{aligned} \tag{3.41}$$

The term $\nabla \cdot (\nabla \mathbf{u})^\top$ is null vector, since the “divergence of the transpose of a vector gradient” is equivalent to the “gradient of the divergence of a vector”, which is evident using the index notation:

$$\nabla \cdot (\nabla \mathbf{u})^\top = \frac{\partial^2 u_j}{\partial x_i \partial x_j} = \frac{\partial}{\partial x_i} \frac{\partial u_j}{\partial x_j} = \nabla (\nabla \cdot \mathbf{u}) = \mathbf{0}.$$

The above shows that if the solvent viscosity is constant throughout the fluid domain ($\nabla \mu = \mathbf{0}$), then the divergence of the solvent stress tensor simplifies significantly, i.e. the diffusion acceleration depends on the Laplacian of the velocity:

$$\nabla \cdot \boldsymbol{\tau}_s = \mu_s \nabla^2 \mathbf{u}. \tag{3.42}$$

3.6.2 Diffusion of variable-viscosity flows

For the sake of completeness, the diffusion of constant-viscosity flows was defined. Since this work investigates variable-viscosity flows, $\nabla \mu \neq \mathbf{0}$, the above simplification does not hold. If the solvent viscosity varies with position (e.g., due to temperature gradients, pressure, or other scalar fields), i.e. for $\mu = f(\mathbf{x}, \mathbf{u}, p, \dots)$, the divergence term has a more complex equation (3.41). Now equation (3.41) may also be investigated further. Equation (3.38) may be substituted into equation (3.37) and $\nabla \cdot \boldsymbol{\tau}_s$ may be expressed as:

$$\begin{aligned}
 \nabla \cdot \boldsymbol{\tau}_s &= \nabla \cdot (2\mu_s \mathbf{E}) \\
 &= \nabla \cdot \left\{ \mu_s \left[\nabla \mathbf{u} + (\nabla \mathbf{u})^\top \right] \right\} \\
 &= \nabla \cdot (\mu_s \nabla \mathbf{u}) + \nabla \cdot \left[\mu_s (\nabla \mathbf{u})^\top \right].
 \end{aligned} \tag{3.43}$$

The identity (3.39) may be applied to the second term of the right-hand-side in equation (3.43), therefore obtaining:

$$\nabla \cdot \boldsymbol{\tau}_s = \nabla \cdot (\mu_s \nabla \mathbf{u}) + \cancel{\mu_s \nabla \cdot (\nabla \mathbf{u})^\top}^{\mathbf{0}} + (\nabla \mathbf{u})^\top \nabla \mu_s. \tag{3.44}$$

In conclusion, the diffusion acceleration has to take into account both derivatives of

the viscosity and velocity:

$$\nabla \cdot \boldsymbol{\tau}_s = \nabla \cdot (\mu_s \nabla \mathbf{u}) + (\nabla \mathbf{u})^\top \nabla \mu_s. \quad (3.45)$$

Fluids devoid of elasticity can be effectively modelled using the diffusion term with variable viscosity without including the effect of $\boldsymbol{\tau}_p$, because their non-linear viscosity characteristics primarily respond to shear rates without memory effects or elastic recovery, i.e. $\mu = f(\mathbf{E})$. The viscosity function can be described using any non-Newtonian model.

3.6.3 Acceleration due to polymeric stress

To accurately model viscoelastic fluids, which exhibit both viscous (energy-dissipating) and elastic (energy-storing) characteristics, it is necessary to introduce an extra stress tensor, $\boldsymbol{\tau}_p$, beyond the purely viscous stress $\boldsymbol{\tau}_s$. This component is commonly referred to as the *polymeric stress tensor* (or *elastic stress tensor*), defined for capturing the fluid's memory effects (deformation history) and its capacity to store and subsequently release elastic energy. The evolution of $\boldsymbol{\tau}_p$ in time and space is typically described by a constitutive equation that involves an time derivative to ensure frame-invariance (i.e., the constitutive relationship remains the same regardless of the observer's motion or rotation). A common choice is the upper-convected derivative (also known as the Oldroyd derivative), which is defined as:

$$\overset{\nabla}{\boldsymbol{\tau}}_p = \frac{D\boldsymbol{\tau}_p}{Dt} - \boldsymbol{\tau}_p \cdot \nabla \mathbf{u} - (\nabla \mathbf{u})^T \cdot \boldsymbol{\tau}_p. \quad (3.46)$$

If the polymeric stress tensor is assumed to be symmetric, this expression can be simplified using the rate-of-strain tensor:

$$\overset{\nabla}{\boldsymbol{\tau}}_p = \frac{D\boldsymbol{\tau}_p}{Dt} - 2\boldsymbol{\tau}_p \cdot \mathbf{E}, \quad (3.47)$$

where the dot-product between two tensors may be defined using the matrix product, $\mathbf{A} \cdot \mathbf{B} = \mathbf{BA}$.

The use of convected derivatives like the upper-convected or lower-convected derivative is crucial in viscoelastic constitutive models to ensure that the material response is described independently of the observer's reference frame, a principle known as material frame-indifference or objectivity.

For this study, as a demonstrative example to validate the proposed numerical methodology, the Oldroyd-B model is employed to represent the polymeric contribution to the total stress. The Oldroyd-B model is one of the simplest linear constitutive models

3 Mathematical modelling

capable of capturing fundamental viscoelastic phenomena, such as stress relaxation and non-zero normal stress differences in shear flow, making it suitable for describing dilute polymeric solutions under general flow conditions [119]. Besides Oldroyd-B model, several other models were introduced by Rivlin, Green, Tobolsky, Ericksen, Lodge, Phan-Thien, Tanner, Giesekus, Doi, Edwards [119]. The evolution of the polymeric stress tensor according to the Oldroyd-B model is given by:

$$\boldsymbol{\tau}_p + \lambda_1 \overset{\nabla}{\boldsymbol{\tau}}_p = 2\mu_p \mathbf{E}, \quad (3.48)$$

where λ_1 is the relaxation time over which the elastic stress relaxes when the strain is constant, and μ_p is the polymeric viscosity contribution representing the viscosity associated with the polymer chains.

The Oldroyd-B model can also be formulated to include a solvent viscosity and a retardation time, λ_2 , which is related to the decay of memory effects in the material. The viscosity ratio may be defined as $\beta = \mu_s/\mu = \lambda_2/\lambda_1$. Setting $\lambda_2 = 0$ reduces the model to the Upper-Convected Maxwell (UCM) model, as this modification eliminates the solvent viscous contribution.

In a Lagrangian framework, the constitutive equation (3.48) can be transformed into a system of ordinary differential equations (ODE), along particle paths. This transformation is advantageous because the Lagrangian approach inherently tracks the deformation history and stress evolution of individual material elements as they move with the flow.

4 Models of non-Newtonian fluids

Understanding the intricacies of viscoplastic and viscoelastic models is essential in numerous scientific and engineering domains, as these models capture the time-dependent deformation and flow behaviors of materials under stress. Their significance extends to diverse applications such as material design, structural analysis, and manufacturing processes, enabling more accurate predictions and optimizations in areas ranging from aerospace engineering to biomechanics.

Linear viscoelastic behavior is defined by a material's ability to exhibit both viscous and elastic properties when deformed. When exposed to external forces, viscoelastic materials can deform over time. This behavior is defined by a linear relationship between stress and strain, where stress is the force per unit area applied to the material and strain is the resulting shape or deformation. The governing equations of linear viscoelasticity are closely related to other linear response theories, such as communication engineering and signal processing. Linear viscoelasticity is related to linear response theory in general, in which the entire system is linear, but this does not imply that the variables have a linear relationship. It refers to the equations that specify variables in linear algebraic, differential, or integral equations or combinations. As a result, a linear system implies that the variables of interest are connected via linear equations.

In general, energy response in viscoelastic materials involves viscous response which occurs when the current condition of stress and strain rate are significant and related to one another. Elastic response occurs when the present rate of stress is proportional to the current state of strain. In terms of energy, a viscous reaction is a dissipative response that loses energy, whereas an elastic response stores energy. The dissipation rate of viscous fluids is proportional to stress times strain rate, but in Newtonian fluids it is related to viscosity times strain rate squared. This is the rate of fluid dissipation. Similarly, with Hooke's elastic material, the storage energy is proportional to stress times strain and to modulus times strain squared. In Newtonian fluids, stress is related to viscosity and strain rate, whereas stress in Hooke's elastic solids is proportional to modulus and strain. The contribution from both of these responses is referred to as the viscoelastic response. There will be energy dissipation and energy storage, with the relative contributions of these two varying depending on the time scale chosen. The total material response may differ depending on how quickly or slowly the material

is examined. The entire response can be related to the current state of stress and strain, strain rate, rate of stress, rate of stress rate, and so on in terms of mathematical formulation for defining the behavior. The time frame range of interest defines the other relative contributions. As a result, relaxation time is defined since much depends on how the material is evaluated, how fast or slow the material is analyzed, and how the reaction changes due to the examined material's viscous or elastic contribution.

The constitutive equation for linear viscoelasticity provides a basic framework for understanding the relationship between stress and strain in these materials. In the context of linear viscoelasticity, various mathematical methods can be used to describe the mechanical behavior of materials. For linear viscoelastic materials, the constitutive equation is a useful tool for describing the mathematical relationship between stress and strain. However, when considering the mathematical methods used to specify the mechanical behavior of linear viscoelastic media, it is important to note that both linear hereditary laws and differential operator laws have practical applications, but each method has advantages and disadvantages. Differential equations are commonly used and debated since they can relate all distinct quantities. The overall formulation can also be viewed from the current level of stress, which is determined by the material's overall history of deformation, resulting in the integral formulation. The models that are described in integral form, where the current state of stress is determined by all of the previous deformations that the material has undergone. When looking at viscoelastic response provided that material is probed at different times and frequencies, it is typically seen that either very high times and frequencies or very low frequencies and short times yield either entirely viscous or completely elastic response.

To fully comprehend the constitutive equation for linear viscoelasticity, it is necessary to consider the various approaches that can be taken to establish this relationship. Three major approaches are frequently used: integral models, linear differential models, and fractional derivative models. Integral models approach the constitutive equation by expressing it in the form of convolution integrals. These integrals capture the viscoelastic material's time-dependent behavior while also relating stress and strain mathematically. Integral models are especially useful for dealing with materials that exhibit complex and nonlinear behavior over time. In contrast, linear differential models describe the constitutive equation using differential operators.

For small deformations, the strain reduces to an infinitesimal strain tensor; for arbitrarily large deformations, the overall finite strain tensor should be used. When working with fluid-like materials, strain frequently does not appear in the overall governing equations; however, when the integral form is considered, strain may appear in the overall governing equation. If solid-like materials are the majority, the standard linear solid model includes strain in the overall governing equation. When considering an

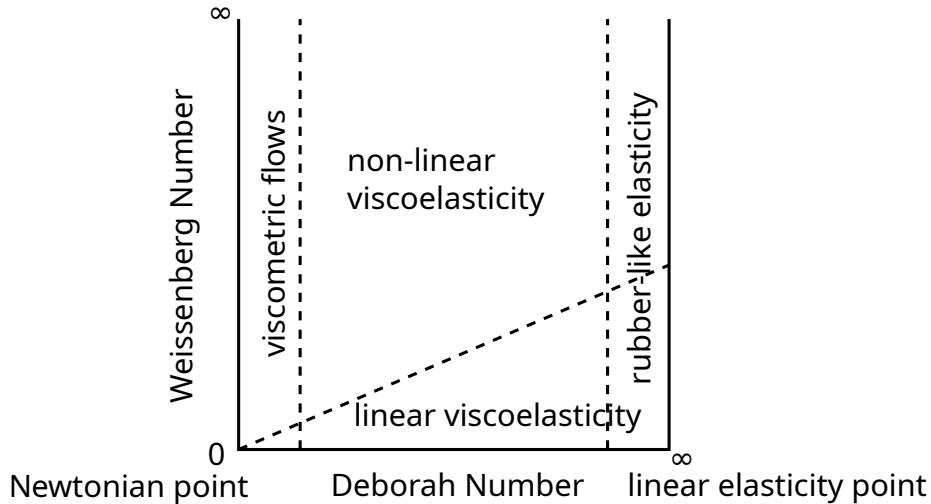


Figure 4.1: Pipkin diagram.

overall model for large deformations, the small infinitesimal strain tensor, which is valid for small deformations, must be replaced by the finite strain tensor. The overall finite strain tensor may be less common than the nonlinear response of solid-like materials.

The Pipkin diagram is a visual representation of the relationship between stress and strain in a material. The elasticity in the Pipkin diagram is shown in Figure 4.1. This diagram is widely used in the field of elasticity to analyze and comprehend the behavior of materials under various loading conditions. It generates a visual "fingerprint" of a material and enables quantitative analysis of its stress-strain relationship.

4.1 Material responses

Responses in linear viscoelasticity refer to a material's behavior in the presence of an external force or deformation over time. Viscoelastic materials have viscous (flow-like) and elastic (spring-like) properties, and their response to stress or strain varies over time. Material reactions can be used to categorize viscoelastic responses and refers to the qualitative description of a class responses, such as viscous, viscoelastic, thixotropic, and so on. Materials may display characteristic responses, such as the Maxwellian response. Material functions measure material reaction in controlled settings. The material functions examined include viscosity, relaxation modulus, storage modulus, loss modulus, stress relaxation, dynamic viscosity, creep compliance, extensional viscosity, and stress growth viscosity. A material function should ideally be linked to another material function. Constitutive models such as the Carreau Yasudi model, Maxwell model, Structural model, and Herschel Bulkley model can be defined if the material response and material functions are recognized. Linear viscoelasticity has two primary responses: the stress response and the strain response. Key material

functions in linear viscoelasticity include:

- Stress response $\sigma(t)$ is the stress force applied per unit area and measures a material's internal resistance to deformation, which is typically represented by a stress relaxation function or a dynamic modulus.
- Stress-relaxation modulus $G(t)$ describes the decay of stress over time when the material is subjected to a constant, instantaneously applied strain. For an ideal elastic solid, $G(t)$ would be constant (the elastic modulus). For a viscoelastic material, $G(t)$ typically decays from an initial glassy modulus $G(0)$ towards a long-time equilibrium modulus (which may be zero for viscoelastic liquids).
- Creep compliance $J(t)$ describes the increase of strain over time when the material is subjected to a constant, instantaneously applied stress. For an ideal elastic solid, $J(t)$ would be constant (the inverse of the elastic modulus). For a viscoelastic material, $J(t)$ typically increases from an initial instantaneous compliance $J(0)$ and may continue to increase indefinitely (for viscoelastic liquids) or approach an equilibrium compliance (for viscoelastic solids).
- Dynamic moduli (Storage Modulus $G'(\omega)$ and Loss Modulus $G''(\omega)$) characterize the material response to oscillatory (sinusoidal) deformation at a given angular frequency ω . When a linear viscoelastic material is subjected to a small-amplitude sinusoidal strain, the resulting stress $\sigma(t)$ will also be sinusoidal at the same frequency but out-of-phase. G' represents the elastic (energy storage) component, and G'' represents the viscous (energy dissipation) component of the response.
- Dynamic viscosity (η' and η'') are related to the dynamic moduli, often in-phase component with strain rate and out-of-phase component with strain rate.

These material functions are central to linear viscoelasticity, and are measured using experimental techniques (stress relaxation testers, creep rheometers, and dynamic mechanical analyzers (DMA)) to provide. Once these material responses and functions are experimentally determined or theoretically understood, they form the basis for defining or fitting constitutive models.

4.2 Constitutive equations of linear viscoelasticity

For linear viscoelasticity, constitutive equations must describe materials that exhibit both viscous (fluid-like, energy-dissipating) and elastic (solid-like, energy-storing) behavior, with the crucial assumptions that the response is linearly proportional to the applied load or deformation and that the Boltzmann superposition principle holds. This principle implies that the response to a complex loading history is the sum of responses to individual loading steps. Constitutive equations are often derived from the

premise of a stored energy functional that reflects the material's internal energy during deformation, or they can be formulated based on phenomenological models (e.g., arrangements of springs and dashpots). These equations typically take the form of linear differential equations or, more commonly for capturing time-dependent history effects, integral equations known as linear hereditary laws. As detailed by Leitman and Fisher [120], these hereditary laws link the current stress to the entire history of strain (and vice-versa) through convolution integrals involving material-specific functions. As stated in the previous section, two fundamental material functions characterize the behavior in linear viscoelasticity: the relaxation modulus $G(t)$ and the creep compliance $J(t)$.

The stress relaxation constitutive equation relates the stress σ and the strain ε through the relaxation modulus $G(t)$, which describes how stress relaxes over time for a given strain history. The integral form is given by:

$$\sigma(t) = \int_{-\infty}^t G(t - \tau) \frac{d\varepsilon(\tau)}{d\tau} d\tau. \quad (4.1)$$

Assuming the material is undisturbed for $\tau < 0$ and the strain is applied starting from $\tau = 0$:

$$\sigma(t) = G(t) \varepsilon(0) \int_0^t G(t - \tau) \frac{d\varepsilon(\tau)}{d\tau} d\tau. \quad (4.2)$$

In the frequency domain, and under sinusoidal loading, this can be expressed as a convolution integral:

$$\sigma(\omega) = G(\omega) * \varepsilon(\omega) \quad (4.3)$$

where $*$ denotes convolution operator, ω is the angular frequency, and $G(\omega)$ is the complex relaxation modulus in the frequency domain which can be related to $G(t)$ through a Fourier or Laplace transform.

The creep constitutive equation relates the strain ε and the stress σ through the creep compliance $J(t)$, which describes how strain accumulates over time for a given stress history. The integral form is given by:

$$\varepsilon(t) = \int_{-\infty}^t J(t - \tau) \frac{d\sigma(\tau)}{d\tau} d\tau. \quad (4.4)$$

Similarly as above, assuming the material is undisturbed for $\tau < 0$ and the stress is

applied starting from $\tau = 0$:

$$\varepsilon(t) = J(t) \sigma(0) + \int_0^t J(t - \tau) \frac{d\sigma(\tau)}{d\tau} d\tau \quad (4.5)$$

In the frequency domain, the relationship is:

$$\varepsilon(\omega) = J(\omega) * \sigma(\omega) \quad (4.6)$$

where $J(\omega)$ is the complex creep compliance in the frequency domain.

In conclusion, these integral constitutive equations, defined by $G(t)$ or $J(t)$, effectively capture the time-dependent, hereditary nature of linear viscoelastic materials.

4.3 History independent models

Now that the viscoelasticity has been defined, it is important to introduce a simplification, i.e. generalized Newtonian fluid models, which are not dependent on the history of deformation. As the flow behavior of Newtonian and non-Newtonian fluids differs significantly, many non-Newtonian fluids where the primary deviation from Newtonian behavior is a shear-rate-dependent viscosity, and time-dependent effects (like thixotropy or viscoelastic memory) are negligible for the process under consideration. In such cases, generalized Newtonian fluid models are widely employed. These models express the shear stress tensor as a product of apparent viscosity and the rate-of-strain tensor $\dot{\gamma}$ (or $2\mathbf{E}$).

4.3.1 Bingham model

The Bingham model, introduced by Bingham in 1922 [2, 13] is a fundamental two-parameter model for viscoplastic materials. These materials exhibit a yield stress below which they behave as a rigid solid, and above which they flow with a constant plastic viscosity. Due to its relative mathematical simplicity, it is widely used in engineering applications across industries like food processing, drilling, oil and gas, and chemicals, where many industrial fluids approximate this behavior. According to the [71] 3D model, the stress tensor is calculated as:

$$\boldsymbol{\tau} = \left[\mu_\infty + \frac{\tau_0}{|\dot{\gamma}|} (1 - e^{-m|\dot{\gamma}|}) \right] \dot{\gamma}, \quad (4.7)$$

where τ_0 is the yield stress, μ_∞ is the dynamic viscosity at infinite shear rate, and m is the regularization parameter to avoid discontinuity in numerical simulations. The

effective viscosity is calculated using the following expression:

$$\mu(|\dot{\gamma}|) = \mu_{\infty} + \frac{\tau_0}{|\dot{\gamma}|} (1 - e^{-m|\dot{\gamma}|}). \quad (4.8)$$

4.3.2 Power Law model

The Power-Law (or Ostwald-de Waele) model is a simple yet widely used two-parameter model that can describe shear-thinning or shear-thickening behavior over a limited range of shear rates. For purely viscous fluids described by this model, the stress tensor is:

$$\boldsymbol{\tau} = k |\dot{\gamma}|^{n-1} \dot{\gamma}, \quad (4.9)$$

and the model is characterised by the effective viscosity, which is expressed as a function of the shear rate in the following manner:

$$\mu(|\dot{\gamma}|) = \mu_0 |\dot{\gamma}|^{n-1}, \quad (4.10)$$

where μ_0 denotes the flow consistency index, while n is the flow behavior index. Based on the flow-behavior index n , three distinct types of fluids can be mathematically modelled. For $n < 1$, the effective viscosity decreases with increase of shear rate, i.e. it describes shear-thinning fluid. For $n > 1$, the model describes a shear-thickening fluid, and $n = 1$ describes a Newtonian fluid. The zero-shear viscosity is approached at minimal shear rates, whereas the infinite shear viscosity is approached at maximal shear rates.

4.3.3 Cross Power Law model

The Cross power-law model is a four-parameter model that describes shear-thinning behavior more realistically over a wider range of shear rates than the Power-law model. It incorporates limiting viscosities at zero and infinite shear rates. The effective viscosity is given by:

$$\mu(|\dot{\gamma}|) = \mu_{\infty} + \frac{(\mu_0 - \mu_{\infty})}{1 + (m \dot{\gamma})^n}, \quad (4.11)$$

where μ_0 is viscosity at zero shear rate, μ_{∞} is viscosity at infinite shear rate, n is the dimensionless flow index rate parameter expressing the degree to which viscosity is dependent on shear rate in the shear-thinning zone, and m is the amount of time in s required for linear behavior to change to a Power Law. The model smoothly transitions from Newtonian behavior at low shear rates ($\mu \approx \mu_0$) to Power-Law like shear-thinning in an intermediate range, and back to Newtonian behavior at high shear rates ($\mu \approx \mu_{\infty}$).

4.3.4 Bird–Carreau model

Bird Carreau is a four parameter model that is valid for the entire range of shear rates. When there are significant deviations from the Power Law systems overall analysis model, such as at very high and very low shear rates, it is necessary to incorporate the values of viscosity at zero and at infinite shear rate. At high and low shear rate values the Carreau fluid behaves as a Newtonian fluid. The effective viscosity is defined by the following equation:

$$\mu(|\dot{\gamma}|) = \mu_{\infty} + (\mu_0 - \mu_{\infty}) \times [1 + (k \dot{\gamma})^a]^{(n-1)/a}, \quad (4.12)$$

where a influences the shape of the transition between the Newtonian plateau and the power-law region, and is set to the default value of 2. μ_0 is the dynamic viscosity at zero shear rate, μ_{∞} is the dynamic viscosity at infinite shear rate, k is the relaxation time in seconds s and n is power index.

4.3.5 Herschel–Bulkley model

Herschel-Bulkley model also belongs to the group of generalized models of a non-Newtonian fluid. In this model stress-strain relationship is non-linear and it is defined by shear stress tensor and effective viscosity equation as follows:

$$\boldsymbol{\tau} = \tau_0 + k |\dot{\gamma}|^n, \quad (4.13)$$

$$\mu(|\dot{\gamma}|) = \min(\mu_0, \frac{\tau_0}{|\dot{\gamma}|} + k \cdot |\dot{\gamma}|^{n-1}), \quad (4.14)$$

where μ_0 is viscosity at zero shear rate, τ_0 is the yield shear stress, k is the consistency and n is the flow index. If the $\tau < \tau_0$ the Herschel-Bulkley fluid will behave as a solid, and based on the value of flow behavior index the fluid shows shear-thinning character for $0 < n < 1$, Newtonian character for $n = 1$ and $\tau_0 = 0$, and shear-thickening character for $n > 1$.

4.3.6 Casson model

The Casson model as a rheological model that is used to describe viscoelastic flow. It is expressed in accordance with the Papanastasiou [71] regularization:

$$\boldsymbol{\tau} = \left[\sqrt{\mu_{\infty}} + \sqrt{\frac{\tau_0}{|\dot{\gamma}|}} \left(1 - e^{-\sqrt{m|\dot{\gamma}|}} \right) \right]^2 \dot{\gamma}, \quad (4.15)$$

where τ_0 is the yield stress, μ_{∞} is the dynamic viscosity at infinite shear rate, and m is the regularization parameter. The effective viscosity is determined using the following

method:

$$\mu(|\dot{\gamma}|) = \left[\sqrt{\mu_\infty} + \sqrt{\frac{\tau_0}{|\dot{\gamma}|}} \left(1 - e^{-\sqrt{m|\dot{\gamma}|}} \right) \right]^2. \quad (4.16)$$

4.4 History dependent models

4.4.1 Linear Maxwell model

There are several factors in viscoelasticity that are associated to one another. The Maxwell model is a two-parameter model used to describe linear viscoelasticity. Stress is related to stress rate and strain rate in this model. As a mode of deformation, simple shear is utilized, and just one component of stress rate and one component of strain rate is considered.

There are nine stress components in practically in all materials, and six components due to matrix symmetry. To fully specify the state of the system, all of these must be solved, but if the material is just subjected to simple shear, it is sufficient to have only one component of stress and strain rate. It is important to remember that the Maxwell model is only valid for simple shear issues with small deformations. The Maxwell model is as follows:

$$\boldsymbol{\tau} + \lambda \dot{\boldsymbol{\tau}} = \mu \dot{\boldsymbol{\gamma}}, \quad (4.17)$$

where λ is relaxation time, μ is the constant which determines viscous contribution. The model can be stated with subscripts to indicate that simple shear is the mode of deformation:

$$\tau_{yx} + \lambda \frac{\sigma \tau_{yx}}{\sigma t} = \mu \dot{\gamma}_{yx}. \quad (4.18)$$

The situations where $\lambda \rightarrow 0$ Maxwell model is as follows:

$$f(\lambda, \boldsymbol{\tau}) = 2 \frac{\lambda_1}{\lambda_2} e^{Q_0(\lambda-1)} \left(1 - \frac{1}{\lambda} \right) + \frac{1}{\lambda^2} \left[1 - \frac{\alpha}{3G_0^2} \text{tr}(\boldsymbol{\tau} \cdot \boldsymbol{\tau}) \right], \quad (4.19)$$

$$\boldsymbol{\tau}_{yx} \approx \mu \dot{\boldsymbol{\gamma}}_{yx}, \quad (4.20)$$

the model reduces to viscous fluid, i.e it describes Newtonian fluid. When $\lambda \rightarrow \infty$ the model is as follows:

$$\dot{\boldsymbol{\gamma}}_{yx} \approx \frac{\sigma \boldsymbol{\gamma}_{yx}}{\sigma t}, \quad (4.21)$$

The model behaves like an elastic solid and is only valid for small deformations. In general, strain rate is not the same as strain rate tensor, and finding convicted rates of strain is required to obtain strain rate. This relationship is adequate because deformations are minor and only linear viscoelasticity is addressed. As a result, it is possible

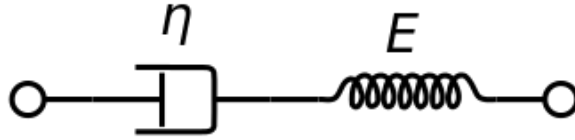


Figure 4.2: The Maxwell model that consists of a completely viscous damper and a strictly elastic spring arranged in series.

to demonstrate:

$$\lambda \frac{\sigma \tau_{yx}}{\sigma t} = \mu \frac{\sigma \tau_{yx}}{\sigma t}, \quad (4.22)$$

when two derivatives are associated for any arbitrary amount of time, it follows that:

$$\tau_{yx} = \frac{\mu}{\lambda} \gamma_{yx}. \quad (4.23)$$

This implies that stress is proportional to strain and is the second parameter that defines the Maxwell model, whereas $G = \mu/\lambda$ is a constant that defines the elastic contribution. As seen, the Maxwell model combines viscous and elastic responses.

Viscoelastic models are sometimes described using mechanical analogs. They are used to illustrate how viscous and elastic responses are coupled in a particular model. Maxwell's model is a sequence of springs representing elastic response and dashpot representing viscous reaction. The analogies aid in comprehending and analyzing the effect of stress and strain on the given model.

Stress relaxation is another type of mechanical deformation. Stress relaxation is an experiment in which the material gamma $\gamma_{yx} = \gamma_{yx}^0$ is subjected to a continuous strain at time $t = 0$. The superscript 0 signifies that the value is constant and does not vary over time. Constant strain is imparted to the material during the experiment, and the response of viscoelastic material may be seen in the response of the Maxwell model. Given that $\gamma_{yx} = \gamma_{yx}^0 = \text{const.}$, the Maxwell model's governing equation is as follows:

$$\tau_{yx} + \lambda \frac{\sigma \tau_{yx}}{\sigma t} = 0; \quad \tau_{yx}(0) = G \gamma_{yx}^0, \quad (4.24)$$

Due to the fact that this is an ordinary differential equation, the solution is exponential. For the initial condition, it is possible to assert that the stress response is fully elastic. For every applied deformation, the parameter G specifies the elastic response of a Maxwell model, i.e. the amount of stress required in the initial time interval $t = 0$. As may be seen from the following equation, the stress decays with time.

$$\tau(t) = G \gamma_{yx}^0 e^{-\frac{t}{\lambda}}, \quad (4.25)$$

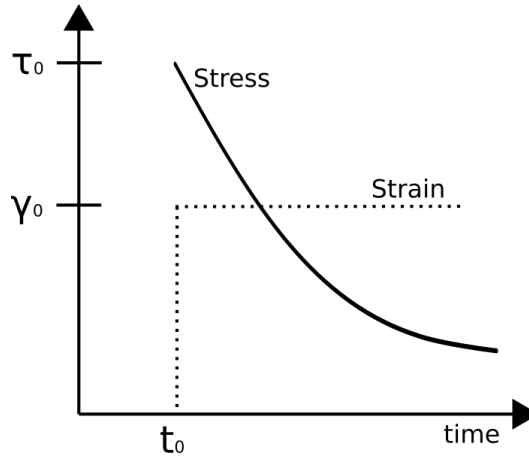


Figure 4.3: Stress response to a step strain.

$$G(t) = \frac{\tau_{yx}(t)}{\gamma_{yx}} = G^{(-\frac{t}{\lambda})}, \quad (4.26)$$

where G is called relaxation module. Because there is a stress decay in the material, as illustrated in Figure 4.3, the stress decreases, a phenomenon known as stress relaxation. The amount of stress necessary to maintain the material in its new deformed state reduces with time, and the rate at which this occurs is defined by λ . If $\lambda \sim 0$, the stress equals zero and the decline is immediate for perfectly viscous fluid. If $\lambda \sim \infty$, there is only an elastic reaction and no decay for perfectly elastic solid.

In the Maxwell model, stress and stress rate are connected to strain rate, and stress results in an exponentially decaying function. The decay of a viscous fluid is instantaneous, whereas Hookean elastic material never decays. Lambda defines how fast or slow the total decay will be for general viscoelastic material with relaxation time as an exponential function. Based on this, the relaxation module is defined as an exponential function that is connected to stress as a function of time divided by strain.

Multiple relaxation moduli can be identified for common materials. Figure 4.3 shows an exponential curve that corresponds to only one relaxation process, as well as the relaxation time. Most common materials, in general, will not be able to fit a single exponential. In that situation, it is necessary to determine the significance of the material's numerous relaxation processes.

Given that any differential equation can be recast into integral form, for example, by employing an integrating factor. In general, there are two types of models in rheological analysis; one is a rate type of model (differential form of Maxwell model) because different rates of different quantities are incorporated, and the same model can be expressed as the stress at present time, which is integral of all past deformations. Because the governing problem is a differential equation, several methods for solving ordinary differential equations, such as the integrating factor approach, can be utilized

to simplify the overall equation. In the case of the Maxwell model, the integral form is as follows:

$$\tau_{yx} \frac{1}{\lambda} e^{(\frac{t}{\lambda})} + \frac{\partial \tau_{yx}}{\partial t} e^{(\frac{t}{\lambda})} = \frac{n}{\lambda} \dot{\gamma}_{yx} e^{(\frac{t}{\lambda})}, \quad (4.27)$$

$$\frac{\partial}{\partial t} \left(\tau_{yx} e^{(\frac{t}{\lambda})} \right) = G \dot{\gamma}_{yx} e^{(\frac{t}{\lambda})}, \quad (4.28)$$

$$\tau_{yx}(t) = - \int_{-\infty}^t G e^{-\left(\frac{t-t'}{\lambda}\right)} \dot{\gamma}_{yx} dt', \quad (4.29)$$

where overall stress is shown as an integrated exponential function multiplied by strain rate. Stress at time t is as follows:

$$t = \sum_{past} [G(t-t')] \times [\dot{\gamma}_{yx} \Delta t'], \quad (4.30)$$

where the term $G e^{-\left(\frac{t-t'}{\lambda}\right)}$ represents weighting factor, and the term $\dot{\gamma}_{yx} dt'$ represent incremental deformation in a small time window. Time-related stress t is the sum of all previous effects, where each effect is a relaxation module multiplied by strain at a different time. The variable $(t-t')$ keeps track of how far back in time is looked. When the time is not too far away, the weighting factor is big, and when the time is much farther away, the weighting factor tends to fall off to zero. Depending on the needs, one can use either the integral form or the rate type form.

Normal stress differences in complex materials can be represented by a convected Maxwell model, in which case the convected rates will be utilized instead of the normal rates. This will be an objective and frame-invariant model that can handle arbitrarily huge deformations. In that situation, the convected model is the rate type model, and there is an equivalent termed the lodge rubber like liquid model, which is an integral model.

4.4.2 Oldroyd-B model

In following section non-linear rheological response of materials and what are the tools that are needed in order to describe the non-linear response are going to be discussed. Since strain is defined through infinitesimal strain tensor which is only valid for small deformations. For large deformations strain tensor should be redefined. In addition, convected rates to be frame invariant and for rates to be proper, instead of using partial or substantial derivatives, the frame invariant rates are needed and especially for quantities such as stress and strain. The frame invariant rates are very useful in determining physically meaningful rates. As an example of that, upper convected and

lower convected derivatives which are quite commonly used in describing the non-linear response of materials.

Time dependent fluids are harder to model since shear stress τ changes with respect to time. Shear stress τ increases or decrease monotonically with constant shear rate $\dot{\gamma}$ and constant temperature. Initial properties are recovered some time after the shear rate has returned to zero. A thixotropic fluids experience hysteresis loop. Examples of these fluids are drilling fluids, grease, printing ink, margarine, and some polymer melts.

The Oldroyd-B model, introduced by James G. Oldroyd in 1950 [19], is a linear viscoelastic constitutive equation widely used to describe the behavior of certain dilute polymer solutions. It is a time-dependent model capable of capturing fundamental viscoelastic phenomena such as stress relaxation, creep, and non-zero normal stress differences in shear flow, while remaining relatively simple to implement and analyze. A common way to present the Oldroyd-B model is by decomposing the total stress tensor into a solvent contribution and a polymeric (or elastic) contribution.

It is a time dependent model that can describe vis

$$f(\lambda, \boldsymbol{\tau}) = 2 \frac{\lambda_1}{\lambda_2} e^{Q_0(\lambda-1)} \left(1 - \frac{1}{\lambda} \right) + \frac{1}{\lambda^2} \left[1 - \frac{\alpha}{2G_3} \text{tr}(\boldsymbol{\tau} \cdot \boldsymbol{\tau}) \right], \quad (4.31)$$

coelastic flow. For a fluid, the stress tensor is calculated from the following equation:

$$\boldsymbol{\tau} + \lambda_1 \overset{\nabla}{\boldsymbol{\tau}} = 2\mu_0 [\mathbf{E} + \lambda_2 \mathbf{E}], \quad (4.32)$$

where μ_0 is total dynamic viscosity composed of solvent dynamic viscosity μ_s and polymer viscosity μ_p , λ_1 is the relaxation time, λ_2 is the retardation constant defined as follows:

$$\lambda_2 = \frac{\mu_s}{\mu_0} \lambda_1. \quad (4.33)$$

The upper-convected time derivative of a tensor, $\overset{\nabla}{\mathbf{A}}$, is expressed as follows:

$$\overset{\nabla}{\mathbf{A}} = \frac{D\mathbf{A}}{Dt} - \mathbf{A} \cdot \nabla \mathbf{u} - (\nabla \mathbf{u})^T \cdot \mathbf{A}. \quad (4.34)$$

The shear-stress tensor can be split into the Newtonian solvent stress τ_s and the extra stress τ_p as follows:

$$\boldsymbol{\tau} = \boldsymbol{\tau}_s + \boldsymbol{\tau}_p, \quad (4.35)$$

where the solvent stress is defined as:

$$\boldsymbol{\tau}_s = \mu_s \hat{\boldsymbol{\gamma}}, \quad (4.36)$$

and the extra stress is defined using the expression:

$$\boldsymbol{\tau}_p + \lambda_1 \overset{\nabla}{\boldsymbol{\tau}}_p = \mu_p \dot{\boldsymbol{\gamma}}. \quad (4.37)$$

4.4.3 eXtended Pom-Pom (XPP) model

The eXtended Pom-Pom (XPP) model is a sophisticated constitutive equation developed to describe the rheological behavior of a significant class of branched polymer melts and concentrated solutions, particularly those exhibiting strain-hardening in extensional flows. The original Pom-Pom model, proposed by McLeish and Larson [121] was derived from molecular considerations of polymer chain dynamics, specifically modeling "pom-pom" shaped molecules with a backbone and multiple arms. Inkson et al. [122] later applied and further developed aspects of this model. The XPP model attempts to bridge the gap between detailed molecular theories and phenomenological models by incorporating key molecular mechanisms (like backbone stretching, arm retraction, and orientation) into a manageable macroscopic constitutive equation. The single-equation form of the XPP model, as often presented, relates the polymeric stress tensor to the deformation rate and molecular parameters. A common representation is:

$$f(\lambda, \boldsymbol{\tau})\boldsymbol{\tau} + \lambda_1 \overset{\nabla}{\boldsymbol{\tau}} + G_0(f(\lambda, \boldsymbol{\tau}) - 1)\mathbf{I} + \frac{\alpha}{G_0}(\boldsymbol{\tau} \cdot \boldsymbol{\tau}) = 2\mu_P \mathbf{E}, \quad (4.38)$$

where λ_1 governs the relaxation of the backbone chain extension, G_0 is the linear relaxation modulus, α is the parameter that controls the anisotropy of the stress tensor, and the function $f(\lambda, \boldsymbol{\tau})$ is defined as:

$$f(\lambda, \boldsymbol{\tau}) = 2 \frac{\lambda_1}{\lambda_2} e^{Q_0(\lambda-1)} \left(1 - \frac{1}{\lambda}\right) + \frac{1}{\lambda^2} \left[1 - \frac{\alpha}{3G_0^2} \text{tr}(\boldsymbol{\tau} \cdot \boldsymbol{\tau})\right], \quad (4.39)$$

where Q_0 is the number of arms at each end of the backbone of the pom-pom molecule, λ_2 is the orientation relaxation time of the backbone segments, and λ is the backbone stretch specified as follows:

$$\lambda = \sqrt{1 + \frac{1}{3G_0} \text{tr}(\boldsymbol{\lambda})}. \quad (4.40)$$

The temporal constants of this model are λ_1 and λ_2 being, respectively, the orientation and backbone stretch relaxation times.

5 Numerical methodology

5.1 The splitting scheme

Numerical methods that separate velocity and pressure yield simpler systems of equations with fewer interdependent variables, so avoiding saddle-point problems. Consequently, these techniques are appealing for specific large-scale issues. This thesis presents a numerical method for the pressure Poisson equation (PPE) reformulation of the Navier-Stokes equations related to viscoelastic fluids within a completely Lagrangian framework. Consequently, by decoupling pressure and velocity using the split-step technique [123, 7], the equations (3.33), (3.34), and (3.35) represent the three primary phases for solving the flow within a time step:

1. moving the fluid particles according to (3.35),
2. solving the pressure equation, derived from (3.34),
3. solving the velocity field using (3.33),
4. increment the time and go to step (1).

The mathematical and numerical details on the listed steps are outlined in the following text.

5.1.1 Pressure equation

A crucial element in developing an efficient numerical approach that separates velocity from pressure is the identification of the appropriate pressure equation. The pressure equation is utilised as a replacement for the continuity constraint equation (3.34), namely the condition that the velocity field stays solenoidal. The pressure field, $p(\mathbf{x})$, must produce the acceleration of fluid particles via the pressure gradient ∇p , ensuring that the equation (3.34) is fulfilled at all discrete time intervals. The pressure field to be determined comes from a scalar Poisson equation, which is derived by applying the divergence operator $\nabla \cdot$ onto the momentum equation (3.33). The corresponding boundary condition at walls is derived by dotting the momentum equation (3.33) by

the wall normal \mathbf{n} [124]. These operations yield the following system:

$$\nabla^2 p = \nabla \cdot \left\{ -\rho \frac{D\mathbf{u}}{Dt} + \rho \mathbf{a}_{\text{ext}} + \nabla \cdot \boldsymbol{\tau}_s + \nabla \cdot \boldsymbol{\tau}_p \right\}, \quad (5.1)$$

$$\frac{\partial p}{\partial \mathbf{n}} = \mathbf{n} \cdot \left\{ -\rho \frac{D\mathbf{u}}{Dt} + \rho \mathbf{a}_{\text{ext}} + \mu \nabla^2 \mathbf{u} \right\}. \quad (5.2)$$

where all the terms are described as follows. For the first term, the divergence of the Lagrangian acceleration is approximated as:

$$\nabla \cdot \frac{D\mathbf{u}}{Dt} = C_{\text{acc}} (\nabla \cdot \mathbf{u}) \frac{|\mathbf{u}|}{\Delta}. \quad (5.3)$$

where C_{acc} is the coefficient for suppressing velocity divergence, based on particle acceleration. Integrating $\nabla \cdot \mathbf{u}$ into equation (5.1) is crucial to mitigate the compressibility in time, and hence, it is commonly referred to as the ‘divergence damping term’. Although its application and interpretation in the Eulerian framework remain ambiguous [125, 123], it possesses physical significance inside the Lagrangian framework. The expression $(\nabla \cdot \mathbf{u}) |\mathbf{u}| / \Delta$ may be understood as ‘how fast the divergence propagates to neighbouring particles’, which must be handled within a time step. In this thesis, the vector for the external acceleration field is taken as constant, $\nabla \cdot \mathbf{a}_{\text{ext}} = 0$. The third term from the equation is the Laplacian, which accounts for the velocity divergence sourcing from the viscous term:

$$\nabla \cdot (\nabla \cdot \boldsymbol{\tau}_s) = C_{\text{visc}} \nabla \cdot [\mu_s \nabla (\nabla \cdot \mathbf{u})], \quad (5.4)$$

where C_{visc} is the coefficient for suppressing velocity divergence, based on viscosity. The last term accounts for the elasticity:

$$\nabla \cdot (\nabla \cdot \boldsymbol{\tau}_p) = C_{\text{elast}} \nabla^2 \text{tr}(\boldsymbol{\tau}_p), \quad (5.5)$$

where C_{elast} is the coefficient for suppressing velocity divergence, based on elasticity component. The coefficients C_{acc} , C_{visc} and C_{elast} are relaxation coefficients, usually taken as 1. In equation (5.2) we assume $\mu = \text{const}$ at Γ_{wall} for simplicity, even for fluids with spatially variable viscosity. This serves as an adequate approximation for second-order schemes, as the viscosity value has already been extrapolated from adjacent fluid node to the wall, and a second extrapolation would not enhance physics. Comprehensive information on the solvability and convergence of the the system of equations (5.1)–(5.2) is provided in [7].

For single phase flows, the gas phase is assumed not to affect the liquid phase flow, and therefore it is not modelled. Consequently, the Dirichlet boundary condition for

the pressure must be imposed at the free surface. When the surface tension is needed to be included in the simulation, the Dirichlet boundary condition is determined from the Young–Laplace equation:

$$p = \sigma\kappa. \quad (5.6)$$

When the surface tension is neglected, the ambient pressure is set to zero value:

$$p = 0. \quad (5.7)$$

In order to impose the boundary conditions at the free surface, the meshless points that are on the edge of the point cloud must be recognised and marked as boundary points to impose the pressure boundary condition (5.6) or (5.7).

Divergence of the diffusion

If one examines equation (5.4), the divergence of the diffusion stress is a scalar that is presented in fully expanded formulation:

$$\begin{aligned} \nabla \cdot [\nabla \cdot (\mu \nabla \cdot \mathbf{u})] &= \mu \frac{\partial}{\partial x} \left(\frac{\partial^2 u}{\partial x^2} + \frac{\partial^2 u}{\partial y^2} + \frac{\partial^2 u}{\partial z^2} \right) + \\ &\quad \mu \frac{\partial}{\partial y} \left(\frac{\partial^2 v}{\partial x^2} + \frac{\partial^2 v}{\partial y^2} + \frac{\partial^2 v}{\partial z^2} \right) + \\ &\quad \mu \frac{\partial}{\partial z} \left(\frac{\partial^2 w}{\partial x^2} + \frac{\partial^2 w}{\partial y^2} + \frac{\partial^2 w}{\partial z^2} \right) + \\ &\quad \frac{\partial \mu}{\partial x} \left\{ \left(\frac{\partial^2 u}{\partial x^2} + \frac{\partial^2 u}{\partial y^2} + \frac{\partial^2 u}{\partial z^2} \right) + \frac{\partial^2 u}{\partial x^2} + \frac{\partial^2 v}{\partial y \partial x} + \frac{\partial^2 w}{\partial z \partial x} \right\} + \\ &\quad \frac{\partial \mu}{\partial y} \left\{ \left(\frac{\partial^2 v}{\partial x^2} + \frac{\partial^2 v}{\partial y^2} + \frac{\partial^2 v}{\partial z^2} \right) + \frac{\partial^2 u}{\partial y \partial x} + \frac{\partial^2 v}{\partial y^2} + \frac{\partial^2 w}{\partial z \partial y} \right\} + \\ &\quad \frac{\partial \mu}{\partial z} \left\{ \left(\frac{\partial^2 w}{\partial x^2} + \frac{\partial^2 w}{\partial y^2} + \frac{\partial^2 w}{\partial z^2} \right) + \frac{\partial^2 u}{\partial z \partial x} + \frac{\partial^2 v}{\partial z \partial y} + \frac{\partial^2 w}{\partial z^2} \right\} + \\ &\quad \frac{\partial^2 \mu}{\partial y \partial x} \left(\frac{\partial u}{\partial y} + \frac{\partial v}{\partial x} \right) + \frac{\partial^2 \mu}{\partial z \partial x} \left(\frac{\partial u}{\partial z} + \frac{\partial w}{\partial x} \right) + \\ &\quad \frac{\partial^2 \mu}{\partial z \partial y} \left(\frac{\partial v}{\partial z} + \frac{\partial w}{\partial y} \right) + \frac{\partial^2 \mu}{\partial x^2} \frac{\partial u}{\partial x} + \frac{\partial^2 \mu}{\partial y^2} \frac{\partial v}{\partial y} + \frac{\partial^2 \mu}{\partial z^2} \frac{\partial w}{\partial z} \end{aligned} \quad (5.8)$$

The equation may be more cleanly written using vector and tensor notation:

$$\nabla \cdot [\nabla \cdot (\mu \nabla \cdot \mathbf{u})] = \mu \nabla \cdot (\nabla^2 \mathbf{u}) + \nabla \mu \cdot \left[\nabla^2 \mathbf{u} + \nabla \cdot (\nabla \mathbf{u})^T \right] + \left\langle \mathbf{H}(\mu)^T, \nabla \mathbf{u} \right\rangle_F \quad (5.9)$$

where the last term is referred to as the Frobenius inner product (or Hilbert-Schmidt inner product in broad context), which is defined as $\langle \mathbf{A}, \mathbf{B} \rangle_F = \text{tr} \{ \mathbf{A}^T \mathbf{B} \}$. It is characterised as “the trace of the product of two tensors, with the first tensor transposed,”

or as “the summation of element-wise multiplication of two tensors”. $\mathbf{H}(\mu)$ represents the Hessian of μ .

The curl-curl identity is defined for the analysis of the first term in equation 5.9:

$$\nabla^2 \mathbf{u} = \nabla (\nabla \cdot \mathbf{u}) - \nabla \times (\nabla \times \mathbf{u}). \quad (5.10)$$

Given that the curl operator consistently produces a solenoidal vector field, applying the divergence to the aforementioned equation results in the equivalence:

$$\nabla \cdot (\nabla^2 \mathbf{u}) = \nabla^2 (\nabla \cdot \mathbf{u}) \quad (5.11)$$

The approximation of equation 5.9 is then given as:

$$\nabla \cdot [\nabla \cdot (\mu \nabla \cdot \mathbf{u})] = 2\mu \nabla^2 (\nabla \cdot \mathbf{u}) + 2\nabla \mu \cdot \nabla^2 \mathbf{u} + 2\nabla^2 \mu (\nabla \cdot \mathbf{u}), \quad (5.12)$$

where the primary term is predominant and should be incorporated as the source term for pressure to mitigate compressibility in extremely viscous fluids resulting from the diffusive dispersion of velocity divergence.

Divergence of the divergence of the polymeric stress

Equation (5.5) introduces the ‘Laplacian of the polymeric–tensor trace’, which is assumed as an appropriate approximation. The derivation of this assumption is explained here, backed by observations in [126], and later validated using numerical experimenting.

An arbitrary symmetric second–rank tensor in three dimensions is defined as 3x3 matrix:

$$\mathbf{T} = \begin{bmatrix} T_{11} & T_{12} & T_{13} \\ T_{12} & T_{21} & T_{23} \\ T_{13} & T_{23} & T_{33} \end{bmatrix}. \quad (5.13)$$

In the field of viscoelastic fluid dynamics, all components of the matrix are contingent upon spatial and temporal variables, $T_{ij} = f(\mathbf{x}, t)$. The “divergence of the tensor divergence”, $\nabla \cdot (\nabla \cdot \mathbf{T})$, is a scalar:

$$\nabla \cdot (\nabla \cdot \mathbf{T}) = \frac{\partial^2 T_{11}}{\partial x^2} + \frac{\partial^2 T_{22}}{\partial y^2} + \frac{\partial^2 T_{33}}{\partial z^2} + 2\frac{\partial^2 T_{12}}{\partial x \partial y} + 2\frac{\partial^2 T_{13}}{\partial x \partial z} + 2\frac{\partial^2 T_{23}}{\partial y \partial z}. \quad (5.14)$$

Alternatively, the aforementioned statement (5.14) can be reformulated utilising the tensor operation:

$$\nabla \cdot (\nabla \cdot \mathbf{T}) = \langle \mathbf{H}, \mathbf{T} \rangle_F. \quad (5.15)$$

where the operation on the right-hand-side of equation (5.15) is known as the Frobenius inner product, $\langle \mathbf{A}, \mathbf{B} \rangle_F = \text{tr} \{ \mathbf{A}^\top \mathbf{B} \}$. Formally, it is defined as “the trace of the product of two tensors, where the first one is transposed”. On the other hand, to understand the above, it is more appropriate to define it as “the sum of element-wise multiplication of two tensors”. \mathbf{H} is the Hessian operator, $\mathbf{H} = \partial^2 / (\partial x_i \partial x_j)$.

Given that the aforementioned equation is challenging to interpret numerically, a simplification in numerical modelling is required. The Hessian of a scalar is a symmetric tensor, attributable to the symmetry of second derivatives, and is defined as the “transpose of the Jacobian matrix of the gradient of a function,” $\mathbf{H}(f) = \mathbf{J}(\nabla f)^\top$. Moreover, if the tensor \mathbf{T} is based on a gradient of vector field, $\mathbf{T} = \nabla \mathbf{v}$, where $\mathbf{v} = [u \ v \ w]^\top$, then \mathbf{T} is defined as:

$$\mathbf{T} = \begin{bmatrix} \frac{\partial u}{\partial x} & \frac{\partial u}{\partial y} & \frac{\partial u}{\partial z} \\ \frac{\partial v}{\partial x} & \frac{\partial v}{\partial y} & \frac{\partial v}{\partial z} \\ \frac{\partial w}{\partial x} & \frac{\partial w}{\partial y} & \frac{\partial w}{\partial z} \end{bmatrix}. \quad (5.16)$$

Consequently, the divergence of the tensor divergence is:

$$\begin{aligned} \nabla \cdot (\nabla \cdot \mathbf{T}) &= \left(\frac{\partial^3 u}{\partial x^3} + \frac{\partial^3 u}{\partial y^2 \partial x} + \frac{\partial^3 u}{\partial z^2 \partial x} \right) + \\ &+ \left(\frac{\partial^3 v}{\partial y^3} + \frac{\partial^3 v}{\partial y \partial x^2} + \frac{\partial^3 v}{\partial z^2 \partial y} \right) + \\ &+ \left(\frac{\partial^3 w}{\partial z^3} + \frac{\partial^3 w}{\partial z \partial x^2} + \frac{\partial^3 w}{\partial z \partial y^2} \right) \\ &= \nabla^2 \left(\frac{\partial u}{\partial x} + \frac{\partial v}{\partial y} + \frac{\partial w}{\partial z} \right) \\ &= \nabla^2 (\nabla \cdot \mathbf{v}) \\ &= \nabla^2 [\text{tr}(\mathbf{T})]. \end{aligned} \quad (5.17)$$

In essence, if the tensor originates from the gradient of a vector field, the div-div operation on the tensor simplifies to the Laplacian of its trace. It is evident that the expression is valid for $\mathbf{T} = (\nabla \mathbf{v})^T$, as well as for tensors derived from symmetrised vector gradients, $\mathbf{T} = 1/2 [\nabla \mathbf{v} + (\nabla \mathbf{v})^T]$. Within the framework of the extra-stress tensor, its trace $\text{tr}(\boldsymbol{\tau}_p)$ signifies the isotropic component of stress that influences volumetric alterations in the material. It quantifies the typical stresses that indicate a tendency for volumetric expansion or contraction under specific stress situations. In summary, the pressure equation derives from the Laplacian of pressure, so it is logical in a numerical setting to utilise (5.17) as the source term for pressure resulting from fluid elasticity.

5.1.2 Velocity equation

The second-order backward differencing formula (BDF2), utilised with varying time-step sizes, is applied to discretise the Lagrangian derivative for velocity:

$$\frac{D\mathbf{u}}{Dt} = \frac{1}{\delta t} \left[\left(\frac{1+2r_t}{1+r_t} \right) \mathbf{u}_{n+1} - (1+r_t) \mathbf{u}_n + \left(\frac{r_t^2}{1+r_t} \right) \mathbf{u}_{n-1} \right], \quad (5.18)$$

where r_t is the ratio of the current and previous time-step sizes, $r_t = t_n/t_{n-1}$. The momentum equation (3.33) incorporates the pressure field as explicit term, which is obtained by solving the system of equations (5.1)–(5.2). Explicitly solving for the next velocity \mathbf{u}_{n+1} by substituting equation (5.18) into the momentum equation (3.33) is obtained by leaving the velocity term \mathbf{u}_{n+1} , and the diffusion term, on the left-hand-side while relegating all other terms (pressure gradient and viscoelasticity divergence) on the right-hand-side:

$$\mathbf{u}_{n+1} = C_{n-1} \mathbf{u}_{n-1} + C_n \mathbf{u}_n + C_{n+1} \mathbf{a}, \quad (5.19)$$

where \mathbf{a} is the total acceleration.

On the other hand, let us look at the momentum equation of generalised Navier-Stokes equations is defined as:

$$\rho \frac{D\mathbf{u}}{Dt} - \mu \nabla^2 \mathbf{u} = 2\mathbf{E} \nabla \mu - \nabla p + \mathbf{F}_{\text{ext}} \quad (5.20)$$

Substituting discretisation of $\frac{D\mathbf{u}}{Dt}$ into the momentum equation, we get:

$$\begin{aligned} \frac{\rho}{\delta t} \left[\left(\frac{1+2r_t}{1+r_t} \right) \mathbf{u}_{n+1} - (1+r_t) \mathbf{u}_n + \left(\frac{r_t^2}{1+r_t} \right) \mathbf{u}_{n-1} \right] - \mu \nabla^2 \mathbf{u}_{n+1} &= \\ &= 2\mathbf{E}_n \nabla \mu_n - \nabla p + \mathbf{F}_{\text{ext}} \end{aligned} \quad (5.21)$$

First let's multiply by $\delta t/\rho$ to see the equation more clear:

$$\begin{aligned} \left(\frac{1+2r_t}{1+r_t} \right) \mathbf{u}_{n+1} - (1+r_t) \mathbf{u}_n + \left(\frac{r_t^2}{1+r_t} \right) \mathbf{u}_{n-1} - \delta t \nu_n \nabla^2 \mathbf{u}_{n+1} &= \\ &= \delta t \left(2\mathbf{E} \nabla \nu_n - \frac{\nabla p}{\rho} + \mathbf{a}_{\text{ext}} \right) \end{aligned} \quad (5.22)$$

where $\nu = \mu/\rho$ is the kinematic viscosity, and \mathbf{a}_{ext} is the external acceleration. Rearranging unknowns to the lhs, and knowns to the rhs:

$$\left(\frac{1+2r_t}{1+r_t} \right) \mathbf{u}_{n+1} - \delta t \nu_n \nabla^2 \mathbf{u}_{n+1} = (1+r_t) \mathbf{u}_n - \left(\frac{r_t^2}{1+r_t} \right) \mathbf{u}_{n-1} + \delta t \left(2\mathbf{E} \nabla \nu_n - \frac{\nabla p}{\rho} + \mathbf{a}_{\text{ext}} \right) \quad (5.23)$$

And dividing by the leading coefficient leads to:

$$\begin{aligned} \mathbf{u}_{n+1} - (\delta t \nu_n) \left(\frac{1+r_t}{1+2r_t} \right) \nabla^2 \mathbf{u}_{n+1} &= \frac{(1+r_t)^2}{(1+2r_t)} \mathbf{u}_n - \left(\frac{r_t^2}{1+2r_t} \right) \mathbf{u}_{n-1} + \\ &+ \delta t \left(\frac{1+r_t}{1+2r_t} \right) \left\{ 2\mathbf{E} \nabla \nu_n - \frac{\nabla p}{\rho} + \mathbf{a}_{\text{ext}} \right\} \end{aligned} \quad (5.24)$$

i.e. using the more readable form, the final equation to obtain the velocity field is:

$$\mathbf{u}_{n+1} - C_L \nu_n \nabla^2 \mathbf{u}_{n+1} = C_n \mathbf{u}_n + C_{n-1} \mathbf{u}_{n-1} + C_{n+1} \left\{ 2\mathbf{E} \nabla \nu_n - \frac{\nabla p}{\rho} + \mathbf{a}_{\text{ext}} \right\} \quad (5.25)$$

where the coefficients are: $C_L = \delta t \left(\frac{1+r_t}{1+2r_t} \right)$, $C_n = \frac{(1+r_t)^2}{(1+2r_t)}$, $C_{n-1} = - \left(\frac{r_t^2}{1+2r_t} \right)$, $C_{n+1} = \delta t \left(\frac{1+r_t}{1+2r_t} \right)$. The momentum equation of generalised Navier-Stokes equations can also be defined as:

$$\rho \frac{D\mathbf{u}}{Dt} - \nabla \cdot (\mu \nabla \mathbf{u}) = (\nabla \mathbf{u})^\top \nabla \mu - \nabla p + \mathbf{F}_{\text{ext}} \quad (5.26)$$

and using the same derivation as above, the discretized equation to obtain the velocity field is:

$$\begin{aligned} \mathbf{u}_{n+1} - C_L \nabla \cdot (\nu_n \nabla \mathbf{u}_{n+1}) &= C_n \mathbf{u}_n + C_{n-1} \mathbf{u}_{n-1} + \\ &+ C_{n+1} \left\{ (\nabla \mathbf{u}_n)^\top \nabla \nu_n - \frac{\nabla p}{\rho} + \mathbf{a}_{\text{ext}} \right\} \end{aligned} \quad (5.27)$$

Conclusion is that the introduced equations are variations of the momentum equation for generalized Navier-Stokes equations that are implemented in the LDD framework to calculate the velocity field with variable viscosity, and other acceleration terms included on the right-hand-side.

5.1.3 Advection step

In Lagrangian CFD methods, the fluid dynamics are analysed from a particle-centric perspective. This approach involves tracking discrete fluid parcels as they advect and carry their properties (such as temperature, etc.). The trajectory of each parcel is computed by integrating its velocity over time, allowing the simulation to capture the evolving flow patterns and interactions within the fluid. The first order derivative in time describes the particle advection within the time step:

$$\frac{D\mathbf{x}}{Dt} = \frac{1}{\delta t} (\mathbf{x}_{n+1} - \mathbf{x}_n) \quad (5.28)$$

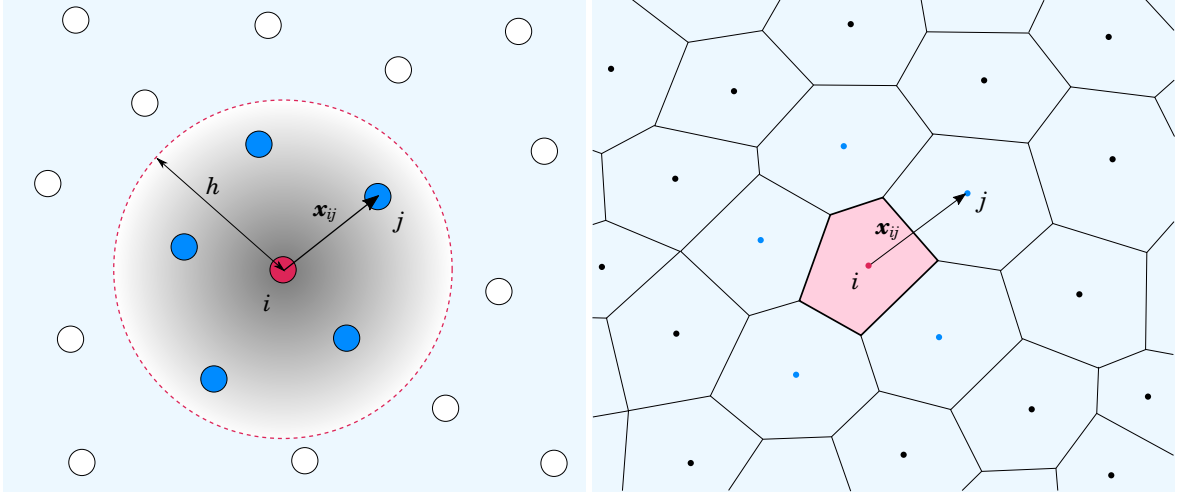


Figure 5.1: Comparison of the mesh-free (left) vs mesh (right) discretisations of the fluid. The central node i is red, while neighbour nodes $j \in \mathcal{N}$ are blue. For meshless discretisation, the neighbour nodes are in sphere of radius h .

so the equation (3.35) may be explicitly solved as:

$$\mathbf{x}_{n+1} = \mathbf{x}_n + \mathbf{u}_{n+1} \delta t. \quad (5.29)$$

The numerical particle is explicitly advected in time using the newly acquired velocity \mathbf{u}_{n+1} . In a discrete numerical framework, advection consistently yields compressive results [127] due to: the method's order (truncation), inadequate convergence, floating-point inaccuracies, or the potential for adjacent streamlines to collide or diverge due to a substantial discrete value of δt . Owing to the intrinsic characteristics of Lagrangian advection, all particles are rearranged post-advection by the PBD method, which is both iterative and unconditionally stable [7, 128]. A semi-implicit strategy for advection is devised utilising explicit movement and implicit reordering.

The variable time-step size in the numerical simulation is determined by the Lagrangian CFL (LCFL) condition number, described as follows:

$$\text{LCFL} = \delta t |\nabla \mathbf{u}|_{\infty}. \quad (5.30)$$

The condition limits the time-step size according to the maximum strain in the flow, namely the L-infinity norm, $|\nabla \mathbf{u}|_{\infty}$, which is independent of the discretisation size, in contrast to the classical Eulerian CFL conditions. The constraint defined as $\text{LCFL} < 1$ ensures that characteristic curves will not meet inside the time step.

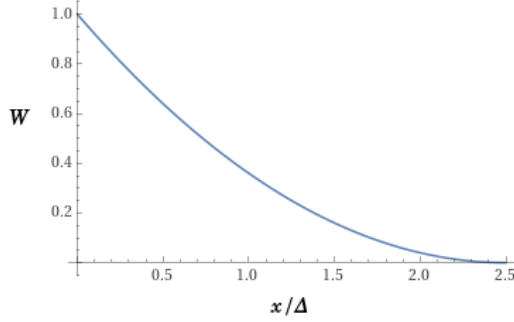


Figure 5.2: Plot of equation 5.31, showing how distance between points influences interaction contribution. The scale is unimportant, as all interactions are renormalised.

5.2 Lagrangian differencing

The split-scheme defining the pressure–velocity–advection steps can be resolved utilising any Lagrangian approach that incorporates consistent spatial operators. In this thesis, Lagrangian Differencing Dynamics (LDD) is extended to simulate viscoplastic and viscoelastic non-Newtonian flows, due to its capacity to achieve second-order precision [91, 7], and due to its performance and extensibility.

LDD represents the computational domain as a point cloud, eliminating the need for topological information. In discrete equations, the Lagrangian particle i is defining the central particle, while j is its neighbour particle from the set neighbouring particles \mathcal{N} . For simplicity of equations, the subscript ij defines the difference between values of two neighbouring particles, $\square_{ij} = \square_j - \square_i$. Particle’s i neighbours $j \in \mathcal{N}$ are searched around the location \mathbf{x}_i to be within the compact radius h , i.e. $0 < |\mathbf{x}_{ij}| \leq h, \forall j \in \mathcal{N}$. For the incompressible flow, closest neighbours are organised to be distanced close to some initial particle spacing, Δ , and the first ring of neighbours around the particle i is taken for the discretisation of spatial operators [91]. So the recommended values of the compact radius are $1.3\Delta < h < 2.5\Delta$, and of $h \approx 1.7\Delta$ is on the safe side to capture full ring of closest neighbours. Based on the incompressibility assumption and $h < 2.5\Delta$, the weighting function describes how much one neighbour contributes to interaction between particles, based on distance \mathbf{x}_{ij} between two neighbours:

$$W_{ij} = \left(1 - \frac{|\mathbf{x}_{ij}|}{h_{max}}\right)^3. \quad (5.31)$$

The defined fluid domain is represented without topological information, using a cloud of points described by set Ω . At a given time, each point $i \in \Omega$ at location $\mathbf{x}_i(t)$ in a specific time instant t carries some fluid properties. Each point i interacts with a set of neighbour points, \mathcal{N} , which are found in the sphere with radius h , as shown in Figure 5.1. A symmetric and positive weighting function $W(r, h)$ is used to evaluate the

strength of interaction between points based on distance between them, $r = \|\mathbf{x}_i - \mathbf{x}_j\|$. Unlike in SPH, where the smoothing function must fulfill the quadrature requirements, in the LDD method the weighting function is used only for weighting of interactions, and therefore, it can take an arbitrary shape. Values of a continuous function $f(\mathbf{x})$ may be approximated anywhere between nodes by using Shepard's formula:

$$\langle f(\mathbf{x}) \rangle = \frac{\sum_{j \in \mathcal{N}} W_j f_j}{\sum_{j \in \mathcal{N}} W_j}, \quad (5.32)$$

where $\langle \rangle$ indicates a discrete version of some expression, $f_j \equiv f(\mathbf{x}_j)$ is introduced for compactness, and $W_j \equiv W(\|\mathbf{x} - \mathbf{x}_j\|, h)$ indicates the weight of the neighbor node j in the neighborhood. A renormalization tensor \mathbf{B}_i for the discrete gradient is defined as [91]:

$$\mathbf{B}_i = \left(\sum_{j \in \mathcal{N}} W_{ij} \mathbf{x}_{ij} \mathbf{x}_{ij}^T \right)^{-1}. \quad (5.33)$$

$$\mathbf{o}_i = \sum_{j \in \mathcal{N}} W_{ij} \mathbf{x}_{ij}. \quad (5.34)$$

which are calculated each time step, for each point's neighbourhood. Since the Navier-Stokes equations are solved in strong form, the equations are directly discretised by substituting the discrete LDD spatial operators. The first-order derivatives discretised in LDD context are defined as follows:

$$\nabla f_i = \sum_{j \in \mathcal{N}} W_{ij} \mathbf{B}_i \mathbf{x}_{ij} f_{ij}, \quad (5.35)$$

$$\nabla \mathbf{f}_i = \sum_{j \in \mathcal{N}} W_{ij} \mathbf{B}_i \mathbf{x}_{ij} \mathbf{f}_{ij}^T, \quad (5.36)$$

$$\nabla \cdot \mathbf{f}_i = \sum_{j \in \mathcal{N}} W_{ij} \mathbf{B}_i \mathbf{x}_{ij} \cdot \mathbf{f}_{ij}, \quad (5.37)$$

$$\nabla \cdot \mathbf{F}_i = \sum_{j \in \mathcal{N}} \mathbf{F}_{ij} (W_{ij} \mathbf{B}_i \mathbf{x}_{ij}), \quad (5.38)$$

where the term $W_{ij} \mathbf{B}_i \mathbf{x}_{ij}$ can be understood as a component of the Hamilton (nabla or del) operator, It is referred to as component, since the complete result is obtained by summing separate neighbour weights $\forall j \in \mathcal{N}$. The Laplacian of a scalar field (results in scalar):

$$\nabla^2 f_i = 2d \frac{\sum_{j \in \mathcal{N}} L_{ij} f_{ij}}{\sum_{j \in \mathcal{N}} L_{ij} |\mathbf{x}_{ij}|^2}, \quad (5.39)$$

where $L_{ij} \equiv W_{ij} (1 - \mathbf{x}_{ij} \cdot \mathbf{B}_i \mathbf{o}_i)$. Equation (5.39) has the same formulation for a vector function, \mathbf{f} . Similarly, the Laplacian with a variable-coefficient multiplier may

be defined as:

$$\nabla \cdot (\phi \nabla f)_i = d \frac{\sum_{j \in \mathcal{N}} L_{ij} (\phi_i + \phi_j) f_{ij}}{\sum_{j \in \mathcal{N}} L_{ij} |\mathbf{x}_{ij}|^2}. \quad (5.40)$$

By using equation (5.33), the discrete approximation of the gradient is obtained using the expression:

$$\langle \nabla f \rangle_i = \mathbf{B}_i \sum_{j \in \mathcal{N}} W_{ij} f_{ij} \mathbf{x}_{ij}. \quad (5.41)$$

The derivation of this expression for the gradient is given in [91], and the convergence theorems are presented in [129]. The method is shown to be consistent up to second-order, and robust on highly irregular arrangements of nodes.

An accurate discrete expression for the Laplacian used in this study belongs to a class of renormalized Laplacian operators, introduced in [91], which were validated on particularly irregular neighborhood arrangements. The discrete Laplacian is defined as:

$$\langle \nabla^2 f \rangle_i = 2d \frac{\sum_{j \in \mathcal{N}} W_{ij} f_{ij} (1 - \mathbf{x}_{ij} \cdot \mathbf{B}_i \mathbf{o}_i)}{\sum_{j \in \mathcal{N}} W_{ij} \|\mathbf{x}_{ij}\|^2 (1 - \mathbf{x}_{ij} \cdot \mathbf{B}_i \mathbf{o}_i)}, \quad (5.42)$$

where \mathbf{o}_i is the offset vector of the node i :

$$\mathbf{o}_i = \sum_{j \in \mathcal{N}} W_{ij} \mathbf{x}_{ij}, \quad (5.43)$$

which points from \mathbf{x}_i to the point where the arrangement the neighborhood dominates. It was shown that renormalization enhances the operator when approximating a scalar field Laplacian, and that it is responsible for reaching second-order accuracy when solving Poisson problems, while original SPH and MPS formulations yield first-order accuracy. This operator is a crucial ingredient to discretize the pressure and velocity equations.

5.3 Algorithm overview

In the discrete Lagrangian framework, the split-step scheme is defined by its independent pressure-velocity-advection steps, which are addressed once during each time increment. This naturally non-iterative method represents the optimal performance to solve the Navier-Stokes equations. Nonetheless, it is important to acknowledge that the technique cannot enforce perfect convergence, owing to the lack of many iterations per time step, as well as additional faults such as truncation order, among others. Therefore, it is essential to regulate the time stepping to guarantee global convergence and preserve system stability in the discrete framework. A single time step comprises the following sub-steps:

1. Advection step:
 - a) Move bodies from either imposed motion, or by using integrated fluid forces and torques.
 - b) Move meshless points along their streamlines.
 - c) Reorder the new positions so that more regular organisation is achieved, as described.
 - d) Interpolate momentum on reordered positions (if needed).
2. Generation step:
 - a) Generate inlet particles, and assign their initial conditions.
 - b) Generate boundary particles on walls by projecting closest fluid particles onto walls.
3. Preparation step:
 - a) Prepare interactions between neighbours (equations (5.33) and (5.43)).
 - b) Detect free surface points, as explained in [7].
4. Pressure equation:
 - a) Prepare the RHS of the pressure equation.
 - b) Solve the pressure equation.
 - c) Calculate the pressure gradient.
5. Velocity equation:
 - a) Prepare the RHS of the velocity equation.
 - b) Solve for velocity.
 - c) Calculate the velocity gradient.
6. Updates based on the solution:
 - a) Calculate variable viscosity.
 - b) Calculate viscoelasticity tensor.
 - c) Calculate fluid forces and torques on the bodies.
 - d) Calculate the next allowable time-step size.

6 Verification and validation

This chapter is dedicated to the rigorous verification and validation of the extended Lagrangian Differencing Dynamics (LDD) method. The primary objective is to systematically assess its accuracy, stability, and capability to simulate the complex rheological behaviors of non-Newtonian fluids. The validation process is structured to address the simulation of time-independent viscoplastic flows and time-dependent viscoelastic flows. A series of well-established benchmark problems are simulated and the numerical results obtained with the LDD method are quantitatively and qualitatively compared against a combination of experimental data, analytical solutions, and previously published numerical results from the literature.

The first part of the validation process focuses on the LDD method's ability to model viscoplastic materials, which are characterized by a yield stress and shear-rate-dependent viscosity. The following benchmark cases are used to assess the implementation of the generalized Newtonian fluid models:

- *Lid-driven cavity flows*: used to verify the method's accuracy in capturing complex recirculation patterns, handling sharp velocity gradients, and performing robustly in geometries with singularities.
- *Dam break*: to test the method's capability to simulate transient, free-surface flows governed by a yield stress; critical for validating the correct prediction of both the initial collapse and the final arrested shape of the material, with results compared directly against experimental data.
- *Fresh concrete slump test*: a widely used engineering test to validate the model against the behavior of a real-world, complex industrial material, the evolution of the slump and spread is compared with experimental findings.
- *Dam break with an elastic gate*: to evaluate the method's versatility by coupling the viscoplastic fluid simulation with a Finite Element Method (FEM) solver to model fluid-structure interaction (FSI), demonstrating its potential for multi-physics applications.

The second part of the validation process assesses the extension of the LDD method for simulating viscoelastic flows, specifically through the implementation of the Oldroyd-B

constitutive model. These benchmarks are chosen to challenge the solver’s ability to capture phenomena arising from fluid memory and elasticity:

- *Lid-driven cavity flow*: revisited in the viscoelastic context, to test the method’s stability at high Weissenberg numbers and its ability to capture key features such as the upstream shift of the primary vortex and the formation of stress-induced secondary eddies.
- *Droplet impact*: used to validate the model’s handling of dynamic interfaces, large deformations, and the characteristic elastic rebound of a viscoelastic droplet upon impact with a solid surface.
- *4:1 planar contraction*: a classic and challenging benchmark for viscoelastic flows, used to evaluate the prediction of strong extensional stresses, vortex dynamics near the contraction, and the overall stability of the method in a flow with significant geometric and stress singularities.
- *Die swelling*: to test the method’s ability to predict the extrudate swell phenomenon, a direct consequence of stress relaxation as the fluid exits the die.

6.1 Viscoplastic fluids

6.1.1 Square lid-driven cavity flow

Lid-driven cavity tests serve as widely recognised benchmarks for evaluating newly developed CFD solvers and methodologies [130]. The straightforward geometry of this test produces a variety of complex and distinct flow types, thereby enhancing the understanding of industrial processes within closed recirculating regions. Strong extension is observed near the lid edges, while the rotational flow is evident in the centre of the recirculating region. The moving lid interacts with the stationary wall as a result of idealisation, leading to a discontinuous velocity profile. Obtaining the complete range of kinematics and the rapid variations in pressure and stress near the corners is more challenging than it initially appears. A suitable method for calculating convection-dominated momentum transfer is essential. Due to the aforementioned factors, lid-driven flow within a cavity serves as an effective preliminary experiment for validating flow characteristics across a range of Reynolds numbers and flow properties.

The two-dimensional steady lid-driven cavity problem is utilised to simulate Casson fluid flow. The validation of the LDD numerical simulations is performed by comparing them with the simulations conducted by [38]. The cavity is defined using dimensionless 1×1 square, and the lid is steadily moving using dimensionless horizontal speed of $u_{lid} = 1$. The no-slip wall-boundary condition is applied at the moving lid geometry

6 Verification and validation

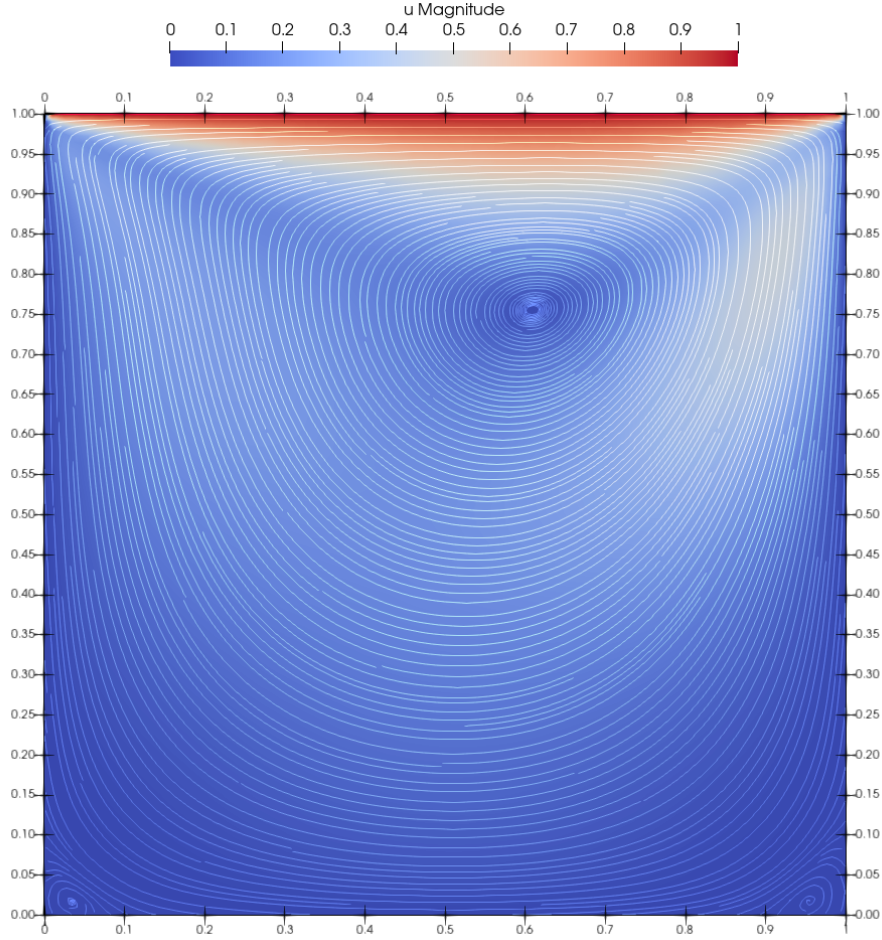


Figure 6.1: Velocity contour plot and streamlines plotted for the flow of Casson fluid in a square cavity, at $Re = 100$ and $Bn = 0.01$.

and at walls. Two resolutions of the point cloud were evaluated. The time step used for both tested simulations was $\delta t = 10^{-3}$, and the average calculation time for a single time step was 12 ms on a modern GPU (RTX 3080). Ten seconds of physical time was simulated. The Reynolds number considered is $Re_{CA} = 100$ and the Bingham number $Bn = 0.01$, where the Reynolds number and Bingham number are defined respectively as:

$$Re = \frac{\rho U_{\infty} l}{\mu_{\infty}}, \quad (6.1)$$

$$Bn = \frac{\tau_y l}{\mu_{\infty} U_{\infty}}, \quad (6.2)$$

where ρ is the fluid density, U_{∞} is the velocity at infinite shear rate, l is the reference length, μ_{∞} is the dynamic viscosity at infinite shear rate.

Figure 6.1 illustrates the velocity magnitude and associated streamlines. The results obtained are in strong agreement with those reported by [38]. The streamline pattern that is plotted in Figure 6.1 shows that the centre of the primary vortex has been successfully simulated and predicted, while the secondary vortices were also simulated

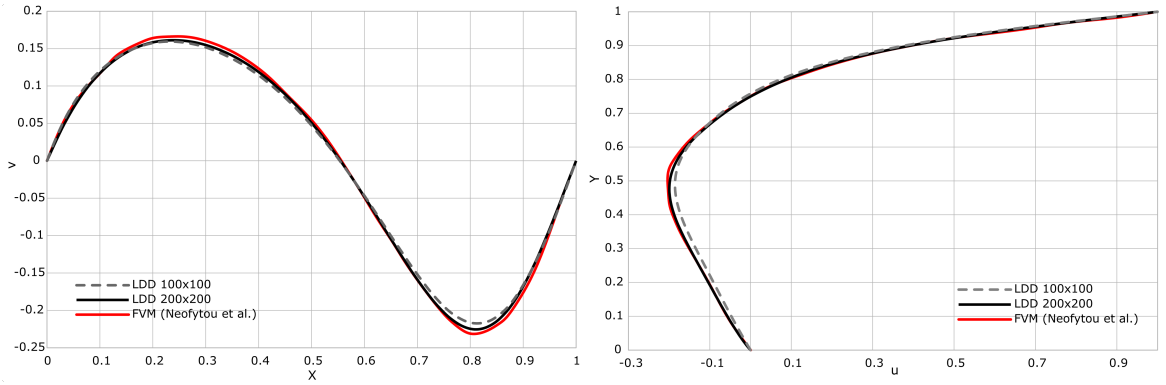


Figure 6.2: The velocity distribution along the horizontal and vertical centerlines of the square lid-driven cavity test.

in the bottom corners of the square cavity. Figure 6.2 illustrates the velocity profiles that are orientated perpendicular to both the vertical and horizontal centerlines of the cavity. Two simulations are conducted with varying initial resolutions of 100×100 and 200×200 , to demonstrate the convergence of the method. The horizontal velocity component for the finer resolution is in superb agreement with the results obtained by FEM. The coarser resolution has yielded somewhat underestimated values, but it demonstrates a general agreement with the reference results. The vertical velocity component that plotted along the horizontal centerline of the cavity for is in very good agreement with FEM, for both resolutions. The sole discrepancy is observed at the highest and lowest peaks, where the vertical component of the velocity exhibited marginally lower absolute values, despite demonstrating strong agreement within other regions.

6.1.2 Skewed lid-driven cavity flow

The Power Law viscosity model is tested for a fluid circulating in a lid-driven skewed cavity flow. [131] was the first to publish results for skewed angles $\alpha = 30^\circ$ and 45° for Newtonian fluids. [132] compared their results with the published results and extended the investigation to various skew angles. An experiment of the skewed cavity using the Power Law, reported by [132], is reproduced in this paper using the LDD method and the results are compared.

The circulation pattern and vortex formation exhibit a strong dependence on the Reynolds number across various rheological behaviours. Consequently, a Reynolds number of 500 was selected for simulation purposes to demonstrate the stability and robustness of the LDD method. The Power Law index was set to $n = 1.5$, the square 1×1 cavity was skewed by using angle of $\alpha = 60^\circ$. As in the previous test case, the lid is steadily moving with a dimensionless velocity of $u_{lid} = 1$. The no-slip wall-boundary condition is applied to the lid and wall boundaries. Two initial resolutions of 100×100

6 Verification and validation

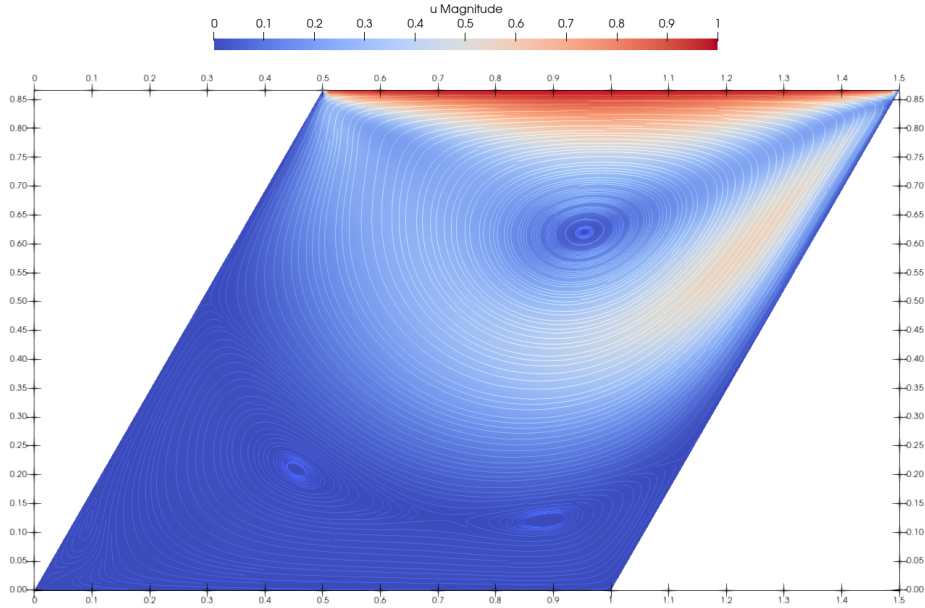


Figure 6.3: Velocity contour plot and streamlines plotted for the flow of Power law fluid in a skewed cavity, for $Re = 500$ and $n = 1.5$.

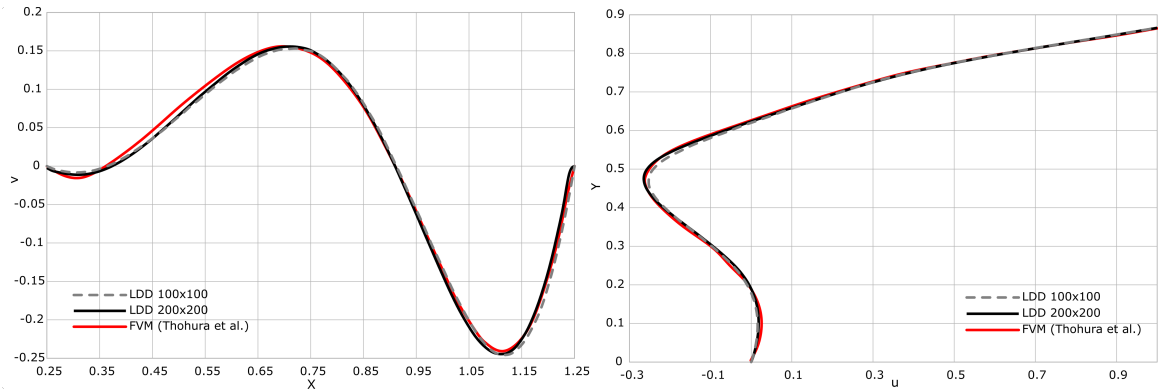


Figure 6.4: The velocity distribution along the horizontal and vertical centerlines of the skewed lid-driven cavity test.

and 200×200 points were tested. Like before, the time step used for simulations is $\delta t = 10^{-3}$, and calculation of a step took 26 ms in average. Twenty seconds of physical time were simulated until a steady state was achieved.

The streamlines depicted in Figure 6.3 align closely with the reference data provided by [132]. The vortices' positions are accurately represented, with the vortex in the lower-right corner being more distinctly illustrated in the LDD method compared to the FVM. Figure 6.4 presents a comparison of the simulated results for the u and v components of velocity along the vertical and horizontal centerlines of the cavity against the reference data. The plotted curves for the u -component of the velocity exhibit a high degree of alignment, whereas the v -component of the velocity shows minor discrepancies up to the height of $Y = 0.65$. The results obtained demonstrate a strong correlation, confirming the method's effectiveness in simulating viscoplastic,

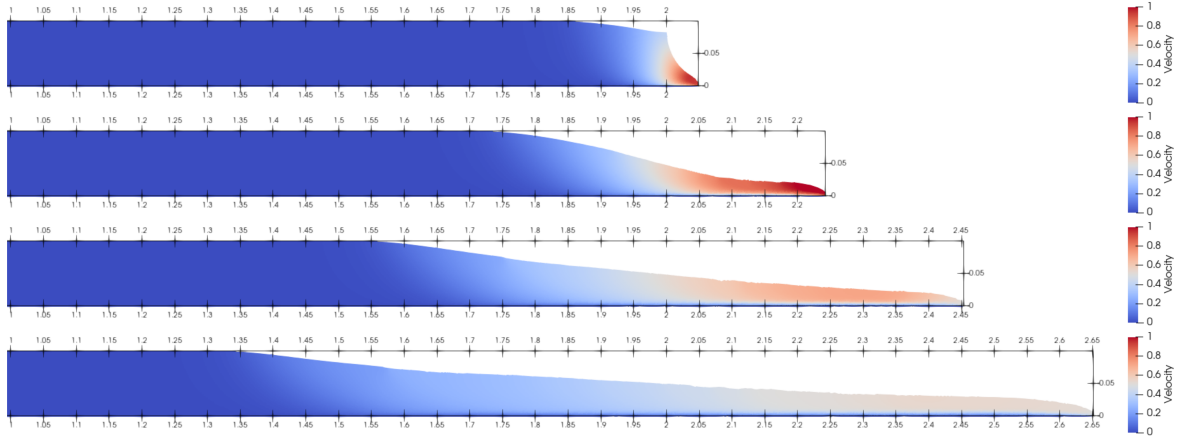


Figure 6.5: Dam break snapshots for time instances $t = 0.1, 0.3, 0.6, 1.0$ s, with the plotted velocity magnitude.

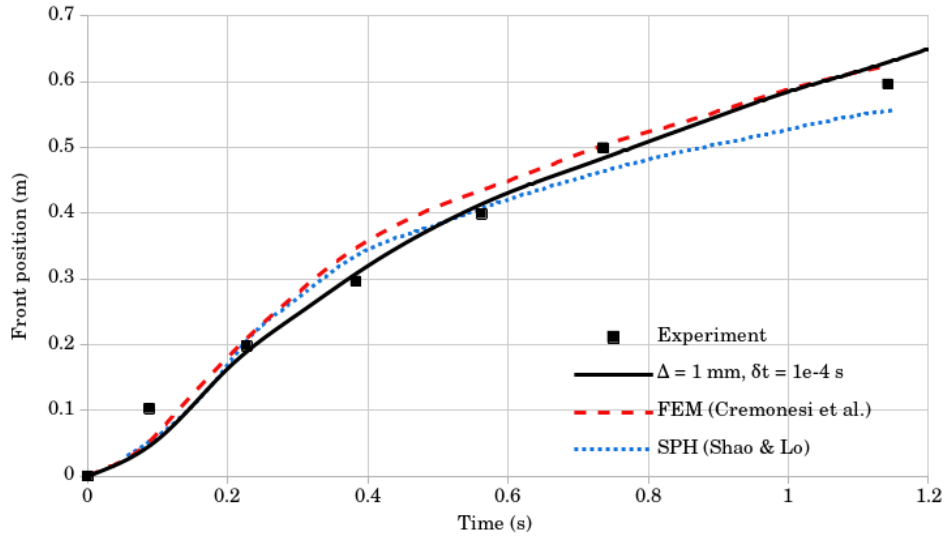


Figure 6.6: Results of dam-breaking front position; comparison of numerical simulations with experimental data.

non-Newtonian, Power Law fluids.

6.1.3 Dam break of a Bingham fluid

A dam break test is performed in accordance with the experimental parameters specified by [133]. A non-Newtonian fluid is characterised by a combination of water and clay, which is stored in a reservoir and subsequently released into a channel measuring 2 meters in length and 0.1 meters in height at the outset. The mixture density of water and mud is $\rho = 1200 \text{ kg/m}^3$, the Bingham yield stress is $\tau_B = 25.0 \text{ Pa}$ and the viscosity is $\mu_B = 25.0 \text{ Ns/m}^2$. The no-slip wall-boundary condition is imposed along the geometry of the channel walls. Snapshots of the point configuration are captured at time intervals of $t = 0.1, 0.3, 0.6,$ and 1.0 seconds, as illustrated in Figure 6.5.

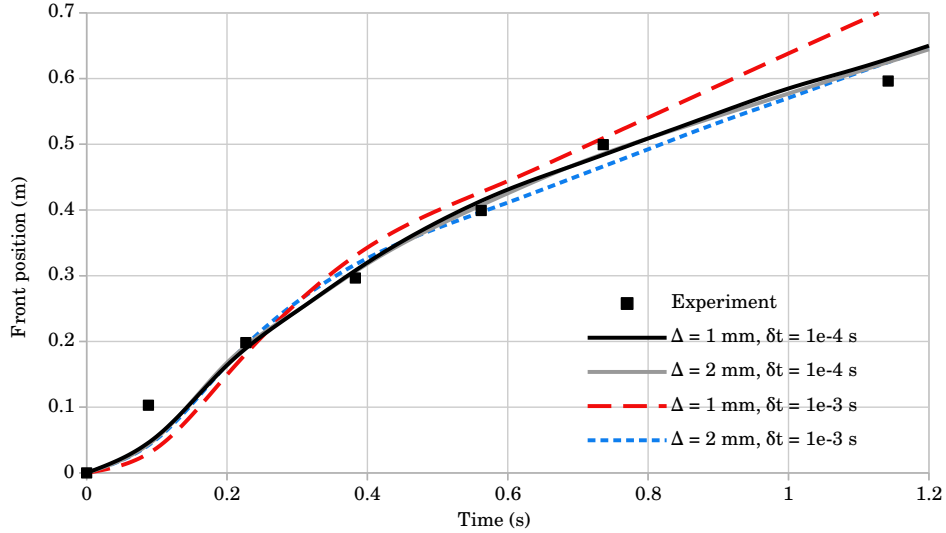


Figure 6.7: The evolution of mass front position for simulations with two points counts and time step sizes for the dam break test, compared to the experimental data.

The outcomes of the LDD method are juxtaposed with the experimental data and alternative numerical methods as illustrated in Figure 6.6. Shao et al. [66] performed the dam-break test using the Incompressible SPH (ISPH) method. In contrast, [46] evaluated a Lagrangian formulation for weakly compressible fluids through an explicit solver based on PFEM. The simulated flow aligns both visually and numerically with the experimental data. The unique features of the flow are identified. At the initiation of flow, the free-standing end of the fluid column commences movement, while the upper free corner begins to collapse. As the fluid flows, its height subsequently decreases, reaching peak velocity at the flow front. At the final stage, the flow exhibits characteristics of creeping flow, resulting in a surface profile that remains largely unchanged, aligning with experimental observations.

From time instance $t = 0.0 \div 0.2$ s, all the numerical methods exhibit discrepancies that can be attributed to not having vertical wall in a channel, which that releases the fluid to flow. The numerical results obtained from the LDD method demonstrate a closer alignment with experimental results in the time interval of $t = 0.2 \div 0.8$ s times compared to other numerical methods. From $t = 0.8 \div 1.2$ s, both the FEM method [46] and the LDD method both show a good fit with experimental data. The results obtained through the LDD method demonstrate the capability of this novel approach to effectively simulate Bingham-type flows and yield realistic outcomes.

A convergence study is conducted utilising two simulations characterized with varying resolutions and time step sizes. The first simulation utilised 200000 points ($\Delta = 1$ mm) and the second simulation utilised 50000 points ($\Delta = 2$ mm). For the both simulations, the size of the time steps were $\delta t = 10^{-3}$ and $\delta t = 10^{-4}$. The comparison of the

tracked mass front position, obtained through numerical and experimental methods, is presented in Table 6.1. The results are also displayed in Figure 6.7. In the case of a domain comprising 50000 points, the average calculation time for a single time step took 35 ms, while for the domain comprising 200000 points and it took 200 ms. The convergence study results indicate that a domain of 200000 points and a time step of $\delta t = 10^{-4}$ yield optimal outcomes, which are utilised for the dam break comparison.

Time (s)	Mass front (m), exp.	Mass front (m), $\Delta = 1mm$		Mass front (m), $\Delta = 2mm$	
		$\delta t = 10^{-3}$	$\delta t = 10^{-4}$	$\delta t = 10^{-3}$	$\delta t = 10^{-4}$
0.09	0.103	0.030	0.048	0.043	0.044
0.23	0.198	0.185	0.190	0.195	0.191
0.38	0.297	0.328	0.304	0.314	0.308
0.56	0.399	0.427	0.414	0.396	0.407
0.74	0.499	0.508	0.484	0.467	0.486
1.14	0.596	0.705	0.628	0.621	0.625

Table 6.1: Dam–break mass–front position determined through numerical and experimental methods at six distinct time instances.

6.1.4 Fresh concrete slump test

The slump test serves as a standard laboratory experiment for assessing the workability of fresh concrete. The slump test will be conducted again to validate the method in three dimensions. Franci and Zhang [48] presented a comprehensive analysis contrasting experimental data with corresponding numerical simulations.

The conical container is filled with concrete, and the subsequent evolution of the form is assessed following the removal of the container. The spread and slump of the evolving concrete are quantified, specifically the fluid height and diameter. The test concludes when there is an absence of fluid movement. The Abram’s test, as defined in the literature [134] is simulated using a single-phase Bingham model. The geometrical and material data are presented in Table 6.2. The computation was performed utilising 50000 points within the domain, with an average time step of 55 ms on the modern GPU. The time step value was established at $\delta t = 10^{-3}$ s, and 40s of simulating physical time was conducted. To evaluate the stability of the solver, the experiment was conducted with larger time steps, reaching $\delta t = 10^{-2}$ s, which demonstrated stability throughout the testing process.

H_0, m	D_0, m	d_0, m	$\rho, kg/m^3$	$\mu, Pa \cdot s$	τ_0, Pa
0.3	0.2	0.1	2200	255	32

Table 6.2: The data of the Abram’s slump test.

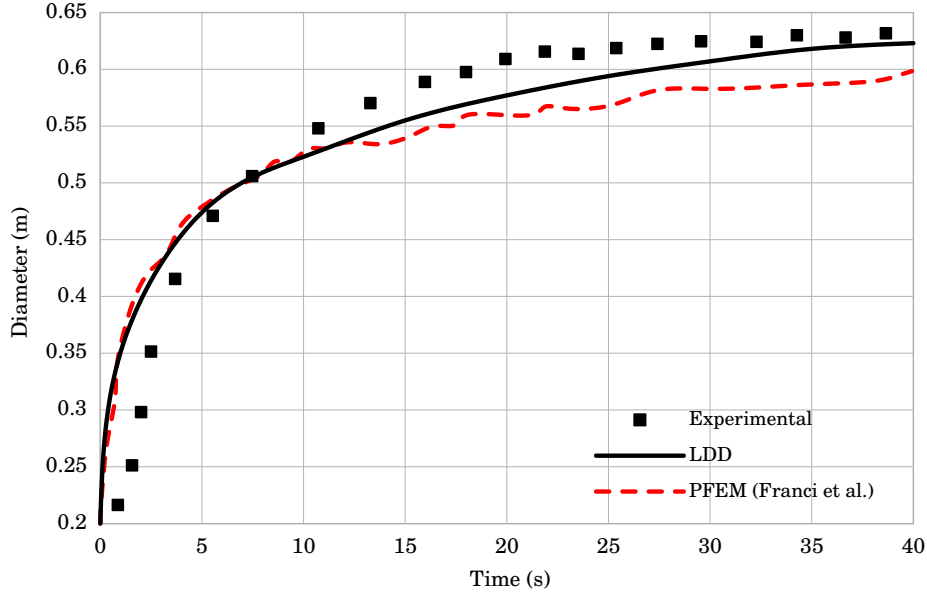


Figure 6.8: The progression of diameter in the Abram slump test; a comparison of numerical simulations with experimental data.

The calculation of cement spread is performed with high precision, as illustrated in Figure 6.8. Throughout the time interval $t = 0$ to 10 seconds, both PFEM and LDD numerical simulations exhibited a comparable progression of the diameter. The diameter values for those time instances exceed those observed in the experiment. At $t = 10.0$ s, the outcomes of the LDD and PFEM begin to diverge. The measurements obtained from both methods exhibit a smaller diameter compared to the experimental results; however, the LDD method is approaching the experimental outcomes asymptotically. At time instance $t = 40.0$ s, the LDD method achieves the experimentally obtained diameter, whereas the PFEM method continues to indicate a lower value. The simulation snapshots illustrated in Figure 6.9 depict the flow results for three specific instances, $t = 0.5$, 5.0 , 40.0 s. The axisymmetric flow exhibits maximum velocity at the apex of the free surface, occurring immediately following the removal of the container. As the top descends gradually, the diameter changes, resulting in a decrease in velocity. Upon the complete collapse of the cone, the diameter gradually expands until the final moment when the fluid exhibits negligible movement. The results align with those presented in [48].

6.1.5 Dam break with elastic gate

The coupling scheme allows for coupling arbitrary structural solvers, which expose an Application Programming Interface (API) that enables sharing structure deformation during solving, and imposing forces to structure elements or nodes. In this thesis, a validated open-source structural solver named *CalculiX* is employed, which is based

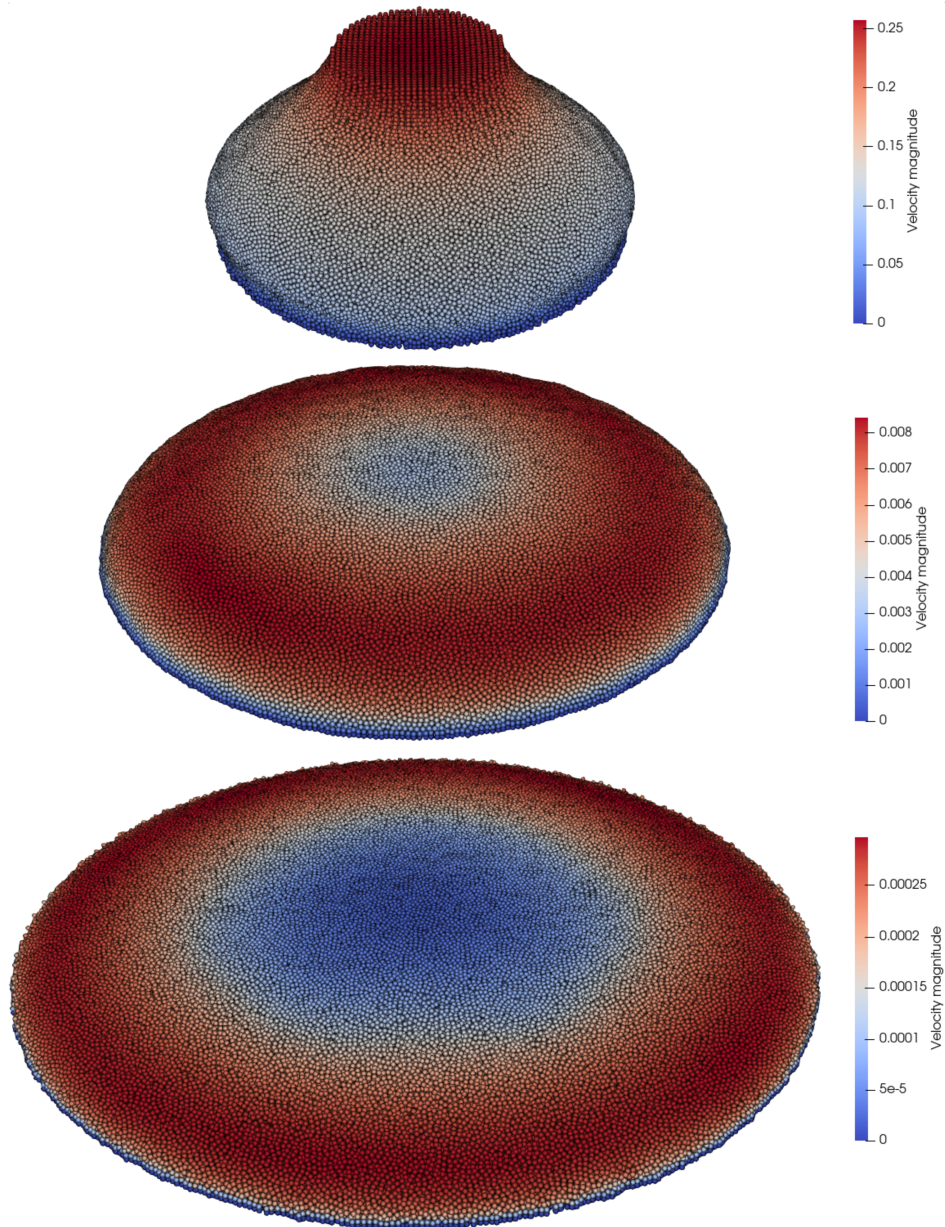


Figure 6.9: Simulation snapshots for three time instances $t = 0.5, 5.0, 40.0$ s with plotted velocity magnitudes.

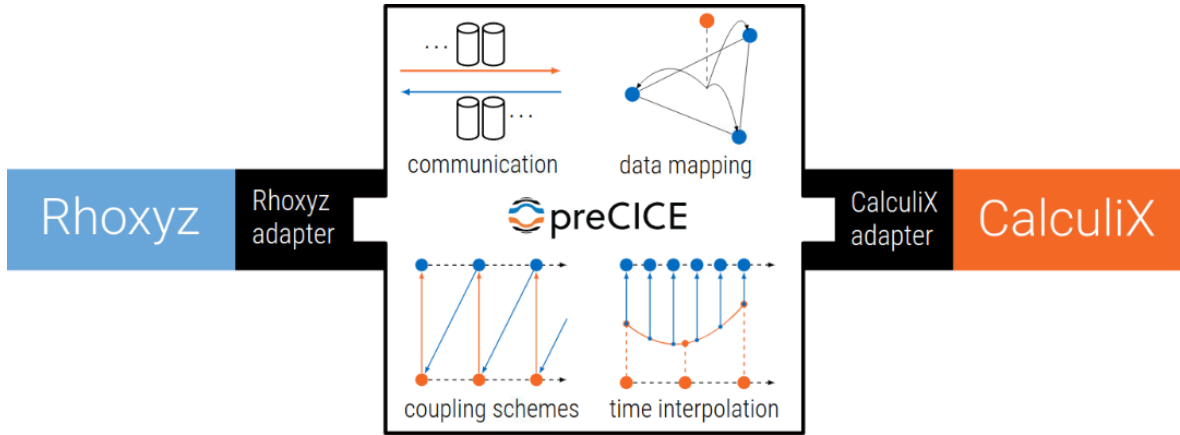


Figure 6.10: Peer-to-peer coupling with automatic temporal and spatial interpolation, for participant solvers *Rhoxyz* and *CalculiX*.

on the FEM [135]. Moreover, an open source coupling framework named *preCICE* (PREcise Code Interaction Coupling Environment) is used for bidirectional partitioned coupling of the structure and flow solvers [136]. The coupling scheme is schematically drawn in Figure 6.10, which renders how *preCICE* provides communication tools for multi-physics simulation. The important ingredients for enabling massively parallel coupled simulations are: mapping of data between non-matching grids, peer-to-peer communication between solver processes, iterative methods for solving interface equations. In this study, the serial and explicit coupling scheme is used. At the start of each time step the solvers synchronise (wait for each other to reach the same point), seeing that the peer-to-peer communication channel must exchange data between the coupled solvers. The flow solver obtains and sends fluid force for each node of the patch mesh, while the structural solver sends deformations of the structure nodes. As implied above, non-matching interface discretisations of two solvers do not pose any issues; forces are conservatively interpolated from one solver to another performed by *preCICE*. Therefore, during this exchange the fluid solver obtains deformations of the structure nodes, i.e. deflections and velocity vectors of moved nodes, which are used for imposing boundary conditions in the flow solver. Meanwhile, using the same communication channel the structural solver obtains fluid forces on each node of the structure mesh. This benchmark involves a structure composed of an elastic isotropic material, which is discretised utilising eight-node brick elements (C3D8). To facilitate coupling from the structural solver perspective, it is essential to establish a defined set of nodes that serve as an interface for the bidirectional transfer of information, such as nodes located on the gate surface.

In this section an experiment conducted by Antoci *et al.* [137] is reproduced. The experiment resembles to typical dam-breaking problem, but the gate is not rigid nor movable, but instead it is elastic and deformable. The rubber gate is clamped along

its upper side to the rigid wall, and it deforms when subjected to fluid forces behind it. The tank space is filled with fluid column of length $A = 100$ mm and height $H = 140$ mm, while the rubber gate is supported by an rigid obstacle and its lower end touches the floor. The gate has thickness of $s = 5$ mm and height of $L = 79$ mm. The rubber gate is modeled using an elastic isotropic material with density $\rho_{gate} = 1100$ kg/m³, and Young's modulus $E = 12$ MPa. Since some uncertainty occurs during estimation of the Young modulus for rubber, future work will include proper rubber hyper-elastic properties. For the validation, the tank was filled with water, $\rho = 1000$ kg/m³ and $\mu = 10^{-3}$ Pa·s, made of 56000 fluid points with initial point spacing 0.5 mm. The constant time-step was $\delta t = 2 \cdot 10^{-4}$ s, and the calculation of a time-step took 40 ms in average on a RTX 2080Ti GPU. The time-step reported in [137] for 6000 fluid SPH particles was $\delta t = 8 \cdot 10^{-6}$, which emphasises the robustness of the implicit solving. Moreover, larger stable time-step values are expected for the implicit partitioned type of coupling that is available in *preCICE* [136], which will be assessed in future work.

The obstacle that supports the rubber gate is suddenly removed, which allows the hydrostatic condition to initially deform the lower end of the elastic plate, and this allows the water to flow under it. The experimental analysis indicated that the resultant flow and plate deformation can be examined as a two-dimensional phenomenon. Therefore two-dimensional flow is simulated, while the fluid forces are imposed on the gate modeled by one column of 28 brick (C3D8) elements. The solution captured during the simulation is shown in Figure 6.11, and compared to the photographs taken during the experiment. The evolution of the gate deformation and water level change is similar between the compared images. Furthermore, the free-surface shape (local elevation) evolution due to pressure gradients from the concentrated outflow is also properly simulated. The results indicate that precise prediction of the displacement of the elastic structure under fluid pressure and the consequent fluid flow may be achieved utilising the LDD method in conjunction with a FEM solver. Further work is required to incorporate authentic rubber-like behaviour of the gate and to evaluate the drawbacks of the explicit coupling method.

In the second numerical experiment, the tank was filled with a Power Law fluid. The shear thickening effect of the flow was employed by setting the flow-behaviour index $n = 2$ and the flow-consistency index $k = 10$ Pa·s². The same initial spacing and time step was used, as defined in the text above. The solution captured during the simulation is shown in Figure 6.12, which renders the pressure field and effective-viscosity field as contour plots. Local maxima of the effective-viscosity scalar field are adequately reproduced at locations with high pressure gradient that generated significant velocity gradient. Some local deficiencies may be seen at the free surface, which will be assessed in future work.

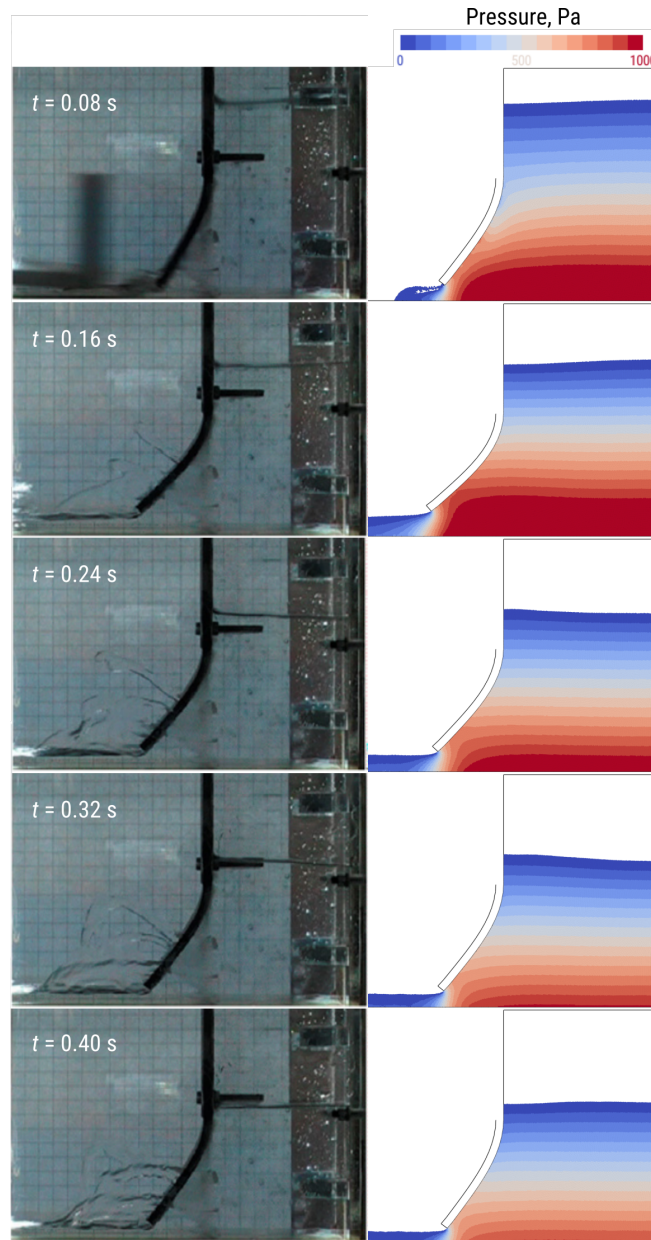


Figure 6.11: Simulation of a dam break for a rubber gate and water, where the numerical results are compared to the experiment photographs.

6.2 Viscoelastic fluids

6.2.1 Lid-driven cavity flow

The lid-driven cavity benchmark serves a critical role in the assessment of viscoelastic flows, demonstrating complex flow behaviours including non-linear velocity profiles, vortical structures, and the emergence of elastic instabilities [1, 138, 5, 139]. The lid-driven cavity configuration establishes an enclosed environment where intricate flow patterns can emerge, facilitating a comprehensive evaluation of the efficacy of a simulation method in representing these phenomena. Viscoelastic fluids often demonstrate

6 Verification and validation

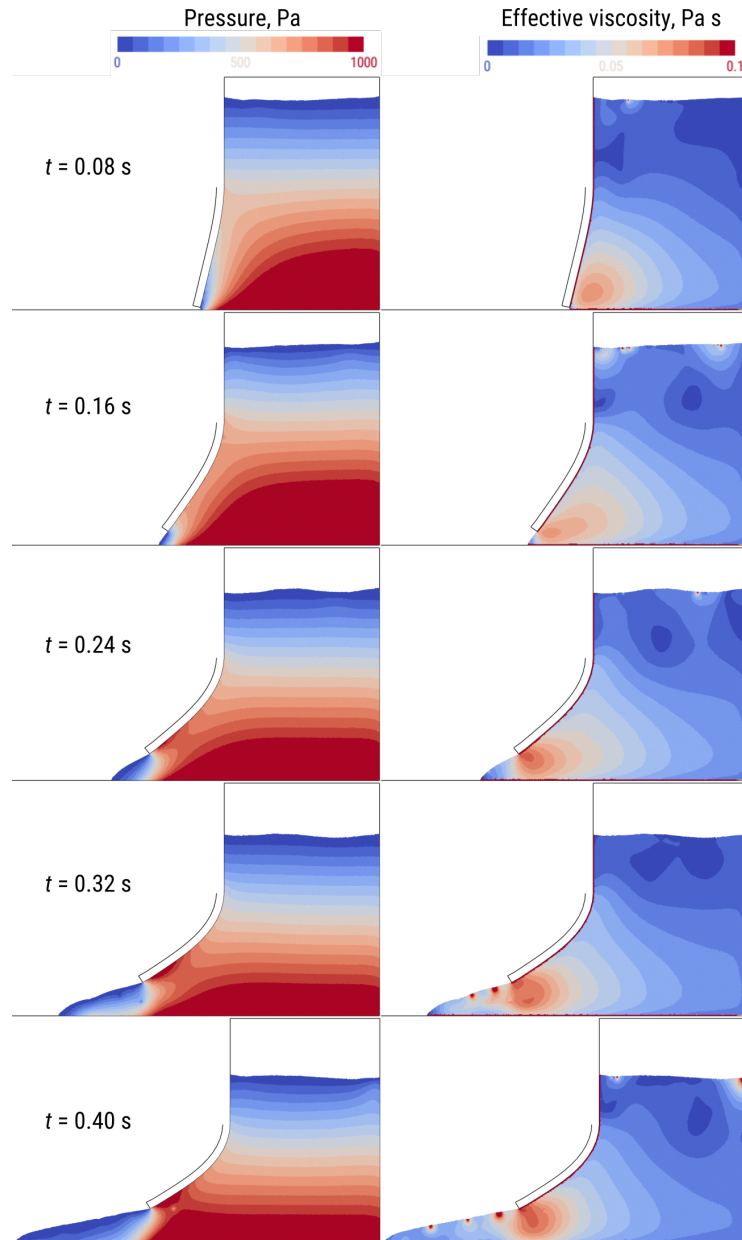


Figure 6.12: Simulation of a dam break for a rubber gate and Power Law fluid with $n = 2$ and $\mu_0 = 10$ Pa·s, where the numerical results show the pressure field and corresponding effective-viscosity field.

shear-thinning behaviour, characterised by a reduction in viscosity with an increase in shear rate. Variable shear rates within the lid-driven cavity facilitate the assessment of the accuracy of a simulation method in representing this non-Newtonian behaviour. The standard mandates recirculation zones where the flow direction is inverted. Due to its elasticity, viscoelastic fluids can exhibit modified or enhanced recirculation. Precisely simulating the dimensions, configuration, and dynamics of these zones is essential for evaluating the accuracy of a simulation technique in representing viscoelastic phenomena. Despite its uncomplicated geometry, this problem is considered very difficult to resolve, especially at elevated Weissenberg numbers, as the flow demonstrates dis-

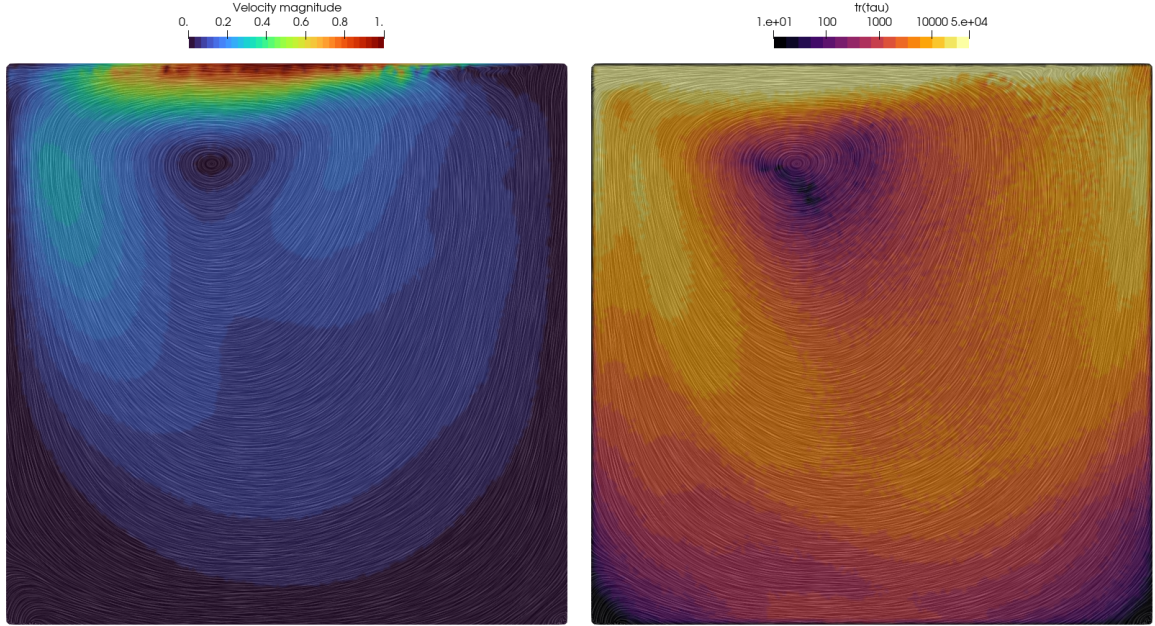


Figure 6.13: Contour plot of the instantaneous velocity magnitude with streamlines (left image) and the trace of the extra-stress tensor (right image), for the lid-driven cavity flow simulation, $Wi = 3$ and $Re = 5 \cdot 10^{-4}$.

tinct attributes that amalgamate shear and extensional deformations.

The LDD was used to solve a benchmark test, lid-driven cavity flow. A square geometry representing the cavity, with a unit length $L = 1$, is filled with fluid. The density of the fluid is set to $\rho = 1$, and the maximum velocity of the lid is $U = 1$. A relatively high Weissenberg number for the simulation [140] is chosen as $Wi = \lambda U/L = 3$, while a constant retardation ratio is applied $\beta = 1/2$. By setting the Reynolds number to a negligible value, $Re = \rho UL/\mu = 5 \cdot 10^{-4}$, the flow is conceptualized as a creeping flow. Near the sliding lid, the extensional rate reaches high values [141]. Because the cavity is a closed system without inlets and outlets, recirculating material accumulates the extra-stress quicker than it relaxes [16]. The flow may not achieve a steady-state solution, and thus show elastic instabilities. Numerically, the modeling of the viscoelastic lid-driven cavity flow at high Weissenberg numbers is as difficult as its Newtonian equivalent at high Reynolds numbers [138, 141]. The corner singularities may be treated by controlled amount of leakage [138] or by modifying the lid velocity profile [16]. Similar to [16], in this study the regularization is applied to the tangential velocity profile of the lid to eliminate the stress singularity at the corners. The profile of the lid's tangential velocity imposed as:

$$u_x(x, t) = 16x^2(1-x)^2 [0.5 + \tanh(8(t-0.5))/2] U, \quad x \in [0, 1],$$

where the hyperbolic tangent moderates the lid's acceleration, but the tangential velocity is exponentially scaled away from the corners. Consequently, the stagnation points

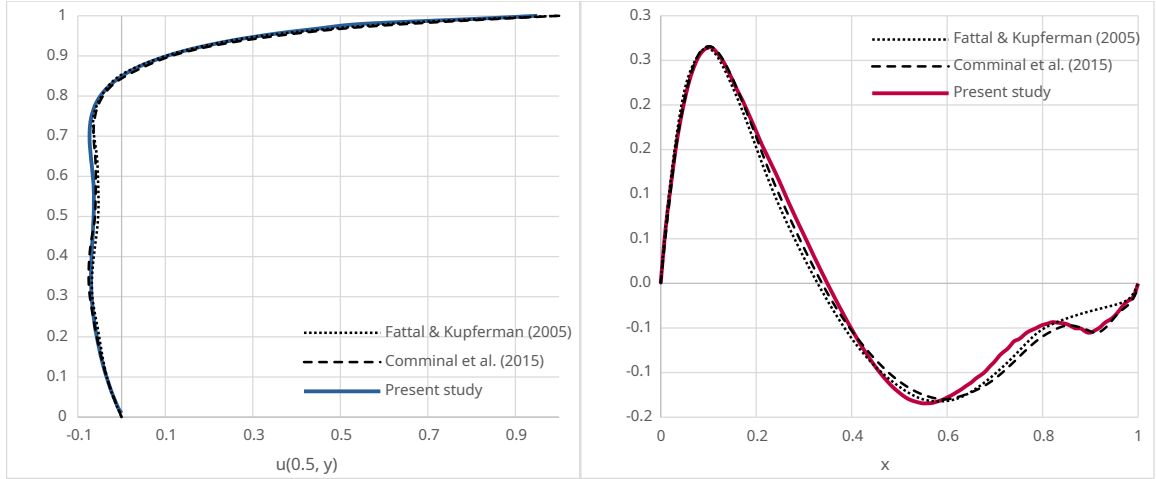


Figure 6.14: The horizontal velocity profile along $x = 0.5$, and vertical velocity profile along $y = 0.75$, for the lid-driven cavity flow simulation, $Wi = 3$ and $Re = 5 \cdot 10^{-4}$.

located at the corners remain impervious to any deformation rate, thereby preventing the development of stress gradients that could escalate rapidly.

In order to maintain consistency with the discretizations of the cited results [16, 77, 140], the initial point cloud was created as a 100×100 grid, resulting in an initial point spacing of $\Delta = 0.01$. The outcomes presented in Figure 6.13 are juxtaposed with the research [140] and [16], which proposed a stream-function derived from the log-conformation formulation [77] for incompressible viscoelastic flows, to guarantee the positive-definiteness of the conformation tensor and to tackle the challenges associated with high Weissenberg numbers. The simulation results effectively demonstrated the upstream displacement of the principal re-circulation vortex, indicating that viscoelasticity has disrupted the symmetry observed in investigations involving Newtonian creeping flow. The small corner eddies are also generated at the base of the cavity. In reality, at the bottom corners there is an infinite series of vortices, diminishing in size and strength as the corner is approached [138]. Comparing the velocity magnitude data depicted in Figure 6.13 with those in [140] reveals that the asymmetry of the velocity within the cavity is well predicted. A distinctive aspect of this benchmark is the upstream deformation of streamlines in the upper-right corner, namely the bent streamlines resulting from the pronounced gradient of the extra stress depicted in the right image of Figure 6.13. This region becomes unstable rapidly if the tangential velocity profile of the lid is not standardised. As a result, the velocity magnitude near the lid exhibits greater gradients at the downstream corner than in the upstream region. The precision of the vortex centre and the derived velocity field is illustrated in Figure 6.14, which presents the simulated velocity profiles for both horizontal and vertical sections, compared to those from [16, 77]. The results derived from the LDD approach indicate an increase in the vertical velocity profile adjacent to the right wall, a finding

corroborated by [16] but not in [16]. The increase in velocity magnitude is also evident from the contours of the velocity magnitude, attributed to the rise in excess stress, as illustrated in Figure 6.13. The peaks and general configuration of the graphs are well synchronised. The LDD solution demonstrates marginally sharper gradients in the vertical velocity profile, which will be examined next.

6.2.2 Droplet impact

This section analyses the impact of a three-dimensional viscoelastic fluid droplet striking a hard plate. Comprehending droplet impact dynamics is crucial across various domains, including inkjet printing, spray coating, and medicinal applications like drug delivery. Droplet impact entails complex interactions between a viscoelastic fluid and a solid substrate. Upon impact, viscoelastic fluids demonstrate deformation, elongation, and fragmentation, complicating the proper modelling of the fluid’s response to external forces through simulation approaches. The simulation commences with a fluid droplet represented as a sphere with a diameter of $D_0 = 20$ μm , situated 40 μm above the rigid plate. The droplet has an initial falling velocity $V_0 = 1$ m/s , and is let to fall down under the Earth gravity conditions $g = 9.81$ m/s^2 , resulting in Froude number at impact $Fn = 2.26$. The density of the fluid is $\rho = 1000$ kg/m^3 , and the Oldroyd-B parameters are chosen as $\mu = 4$ $\text{Pa}\cdot\text{s}$, $\lambda_1 = 0.02$ s and $\lambda_2 = 0.002$ s . This results in $Re = 5$, $\beta = 0.1$, and $Wi = 1$. The relaxation time governs the elastic reaction of the droplet upon impact, whereas viscosity influences the diffusion of advection and elasticity, as well as the droplet’s ultimate shape.

Two resolutions of the droplet were examined, with beginning point spacings of $\Delta = 0.4$ μm and $\Delta = 0.25$ μm , resulting in 60,000 and 250,000 fluid Lagrangian points, respectively. The progression of the coarser droplet simulation is depicted in Figure 6.15, where the hitting droplet is bisected to examine the viscoelastic effects. The velocity field’s magnitude may clarify the evolution of the droplet shape. Upon collision, the droplet experiences vertical compression and horizontal elongation, as illustrated in the initial three photos in Figure 6.15. Unlike Newtonian flows, at maximal compression and horizontal expansion of the droplet, the volume is concentrated near the outside of the droplet. The energy shift from the droplet’s centre is illustrated in the fourth and fifth images in Figure 6.15. Ultimately, the extended form of the droplet reverts to its final oval configuration. The progression of the droplet diameter is marked by quick oscillations, oscillating between local maxima and minima until it ultimately stabilises at an intermediate value. This is shown in Figure 6.16, and the results of two simulations performed using the proposed method are compared to numerical results by [11] and [142]. The results of this investigation corroborate the conclusions of [11, 142], so further validating the proposed methodology. The gradient and apex

6 Verification and validation

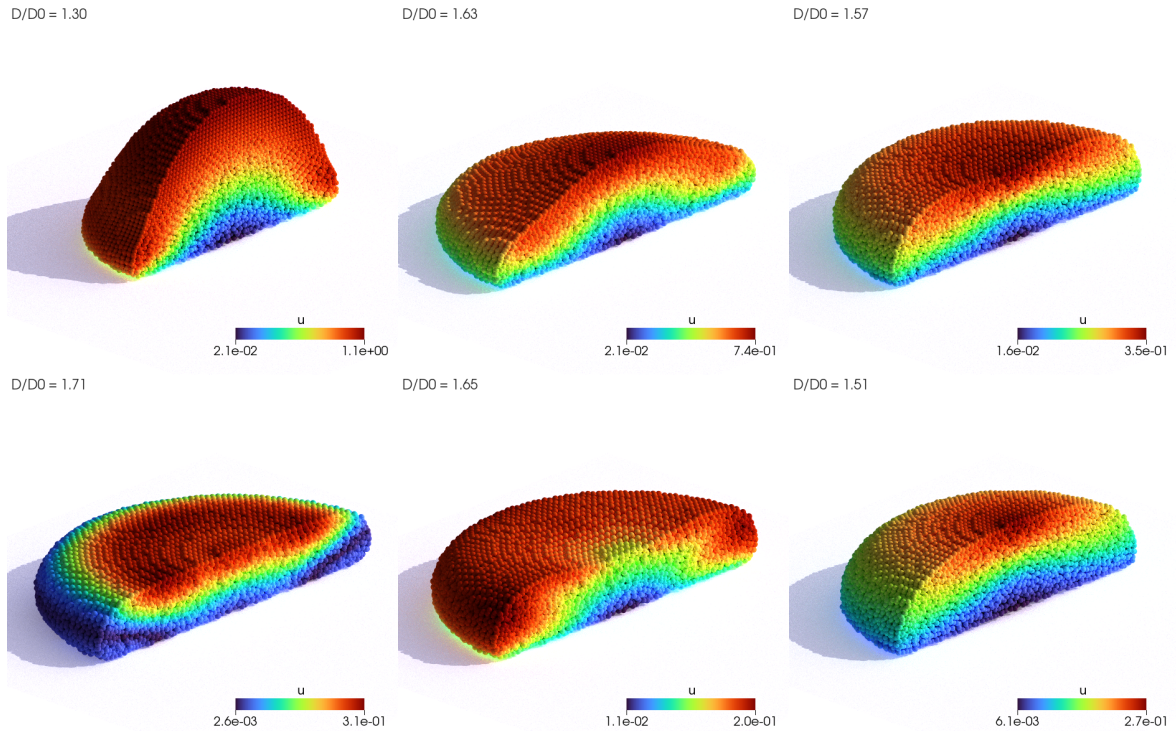


Figure 6.15: Evolution of droplet deformation during impact, illustrated with velocity magnitude. The simulation with point spacing $\Delta = 0.4$ mm demonstrates the solver’s ability to replicate viscoelastic effects at coarser point cloud resolutions.

of the diameter elongation closely resemble the findings in [142]. Nonetheless, one discrepancy is that the local minimum peak in the simulations is not as pronounced as those observed in the references. The discrepancy is presumably due to the application of the no-slip boundary condition for sliding free-surface locations along the plate, which impedes the droplet’s compression following elongation. Additional inquiry is required to validate this hypothesis. In contrast to [11] and other SPH methodologies, no tensile instabilities or fracture phenomena were observed.

6.2.3 4:1 Planar contraction

The ‘4:1 planar contraction’ problem serves as a critical benchmark for viscoelastic flow solvers in computational fluid dynamics, especially in the context of viscoelastic fluid dynamics. This design, characterised by an abrupt reduction of the flow channel from a broader to a narrower dimension, creates a complex flow scenario beneficial in polymer processing and inkjet printing [143]. This benchmark is crucial as it discusses and evaluates the solver’s capacity to accurately represent the detailed behavior of viscoelastic fluids during abrupt geometric alterations. Extrusion is a prevalent polymer fabrication technique for producing elongated, uniform components. A die melts and molds plastic into the specified cross-sectional form. Material extruded through the

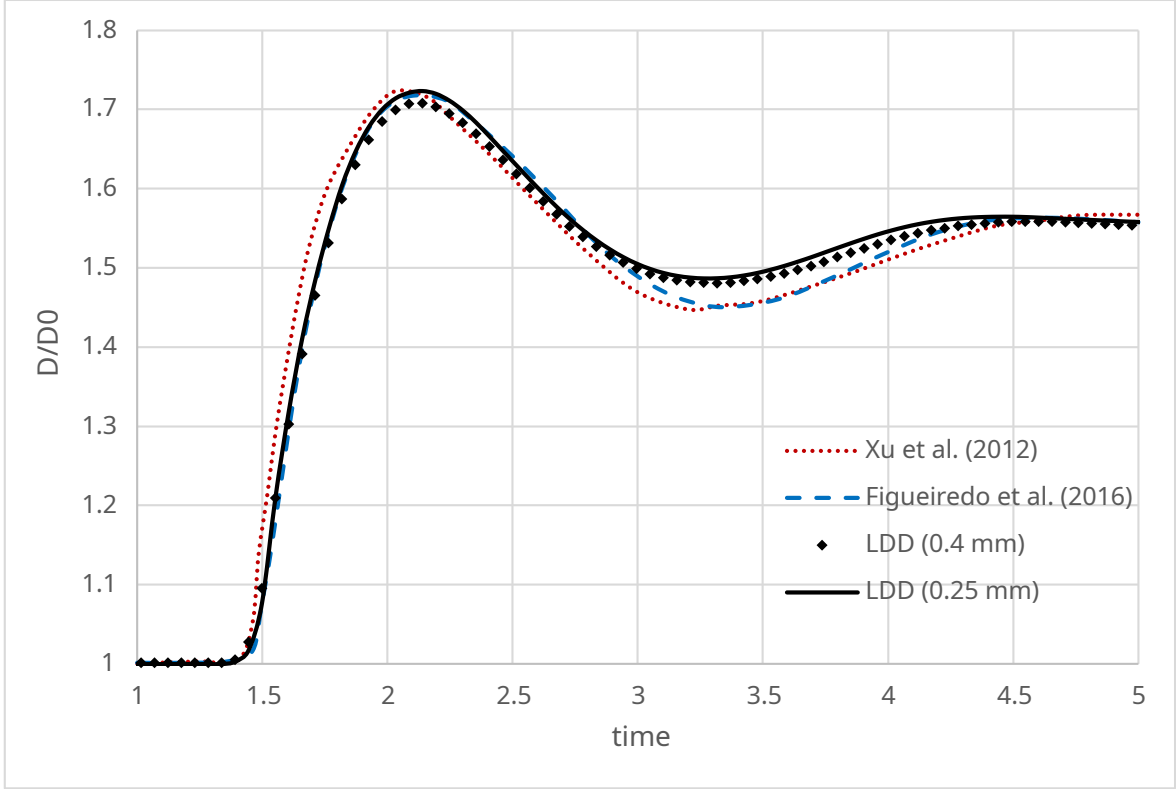


Figure 6.16: Analysis of the simulated evolution of viscoelastic–droplet diameter upon the impact.

die expands upon exit due to the reorganization of flow patterns. The flow shifts from parabolic profiles within the die, limited by the walls, to a uniform profile outside the die, where the free surfaces achieve equilibrium — a phenomenon known as ‘extrudate swelling’. Swelling may induce distortions in the extrudates, resulting in the formation of non-axisymmetric profiles. Flow disturbances impede the efficiency of polymer extrusion at elevated extrusion velocities. This benchmark test evaluates the solver’s numerical stability and robustness, as steep velocity gradients and high strain rates in the contraction zone may lead to convergence or numerical diffusion problems.

The velocity field findings for the two simulations, $Wi = 5$ and $Wi = 10$, are presented in Figure 6.18. In the simulated instance of $Wi = 5$, a complicated pattern featuring two merged recirculation zones is evident. The diminutive vortex is revolving around the contraction corner, but the larger vortex extends from the smaller vortex to the adjacent wall. The post-processing artifacts evident at the recirculation corner in Figure 6.18 arise from the Lagrangian character of the flow, making it challenging to record the streamlines of mesh-free points that are advecting at near-zero velocity. The corner–vortex length for the steady solution for $Wi = 5$ is measured to be around $X_R = 1.2h$, while for $Wi = 10$ the length measured as $X_R = 2.3h$. The corner–vortex lengths are corresponding to the values reported by [144] and [145]. [146] and [147] present the simulations in which the size of the lip vortex continuously increases as the

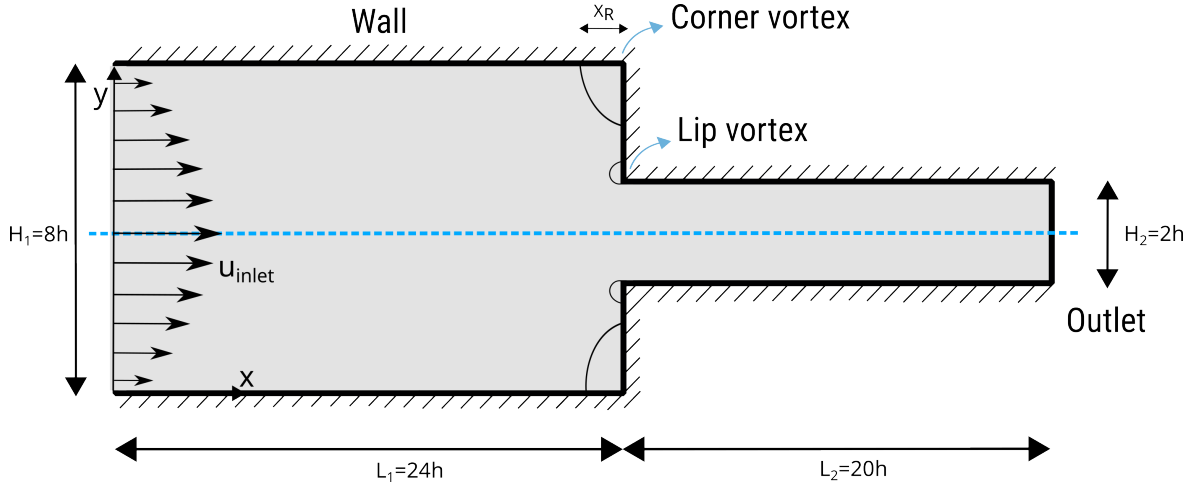


Figure 6.17: The geometry of the 4:1 planar contraction and the positions of the recirculation vortices are shown. X_R is the corner vortex's reattachment length.

Weissenberg number increases, while the corner vortex decreases in size. The findings are significantly contingent upon the mesh resolution. Mousavi et al. [148] illustrated that elastoviscoplastic (EVP) flows in a 4:1 planar contraction reveal unyielded zones that enlarge with heightened material elasticity and yield stress, whereas transient flow patterns arise when the Weissenberg and Bingham numbers surpass critical thresholds. In the instance of LDD, we have not seen any substantial alterations in the configurations of lip and corner vortices attributable to varying point-cloud resolutions. The reductions in size correspond to an increasing Weissenberg number up to $Wi \approx 3$. Subsequently, the vortex intensifies with an increase in the Weissenberg number. The change between the two regimes is located at smaller Weissenberg numbers when a coarser mesh is used [147]. For example, in [147] the corner vortex start to abruptly spread for $Wi > 10$, while in [144, 145] the corner vortex start to abruptly spread for $Wi > 4$. All references agree that the stress cannot be perfectly resolved in the small region near the re-entrant corner, which is not surprising because of the corner singularity exists regardless of the computational grid-resolution. Since the current implementation of the LDD method does not include adaptive refinement of the Lagrangian point cloud that is important in the boundary layer region, in this study the lip vortex for small Weissenberg numbers $Wi < 3$ could not be analyzed. Therefore, Figure 6.18 presents the case $Wi = 5$ in which the lip vortex has significant size compared to the point-cloud resolution, i.e. spacing between neighboring points. From the figure, it is also evident that the simulation with larger Weissenberg number produced larger corner vortices.

Figure 6.19 renders the principal stress difference (PSD) around the contraction for

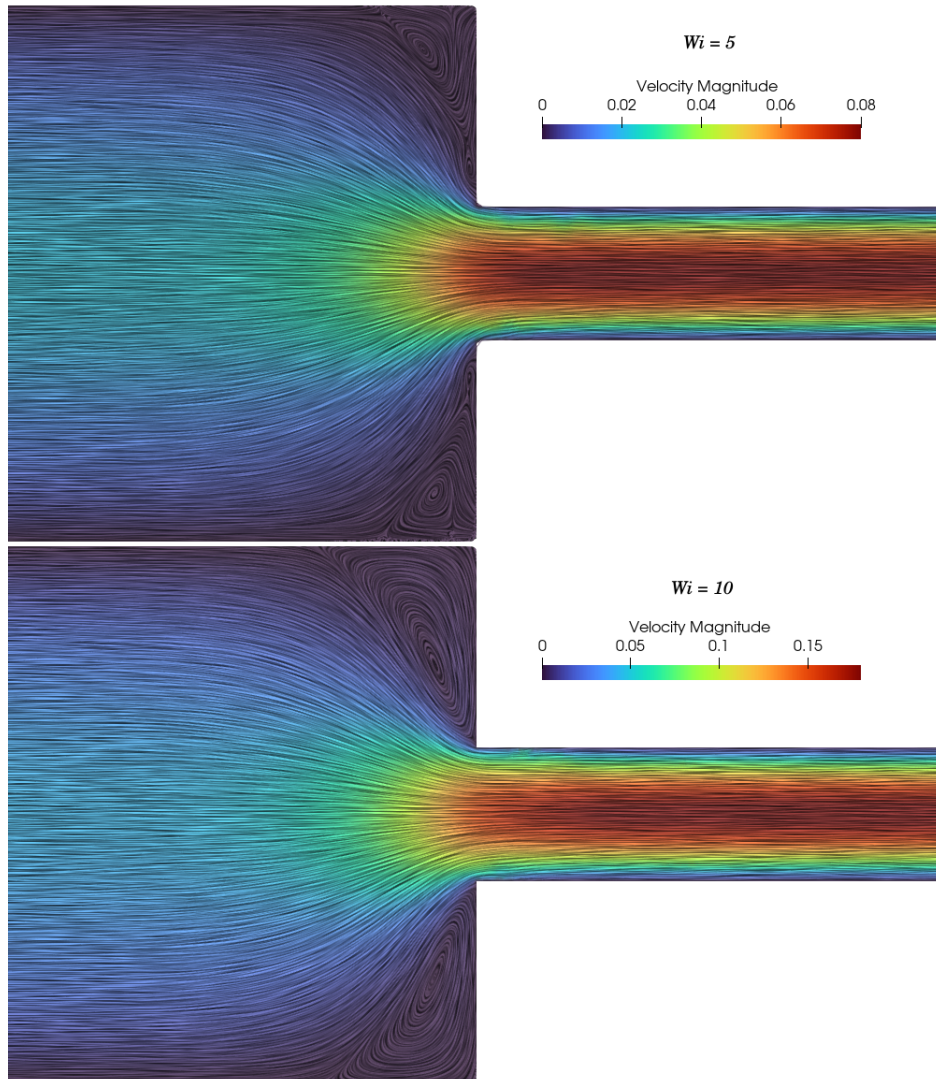


Figure 6.18: Contour plot of the velocity magnitude and streamlines for the 4:1 planar contraction, for $Wi = 5$ (top image) and $Wi = 10$ (bottom image).

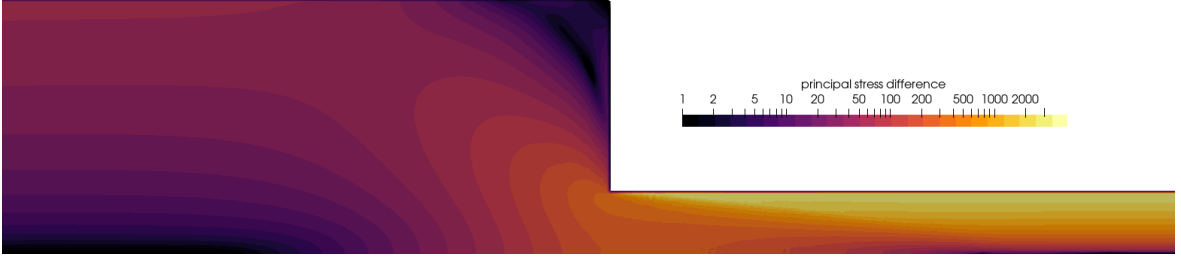


Figure 6.19: Contours of the principal stress difference (PSD) around the 4:1 planar contraction, simulated for $Wi = 5$.

$Wi = 5$, which is calculated based on the components of the extra-stress tensor as:

$$PSD = \sqrt{(\tau_{xx} - \tau_{yy})^2 + 4\tau_{xy}^2}.$$

The contour plot of the PSD, presented on a logarithmic scale, is discretized into 24 levels to facilitate the analysis and comparison of significant value transitions with experimental data from [143] and [78]. The numerical results indicate that the predicted PSD pattern aligns closely with the experimental data obtained from the flow induced birefringence (FIB) device. The critical details, namely the pattern within the vortex and the "butterfly pattern" of the PSD [143] are accurately predicted. The vortex contours are appropriately elongating, while the pattern around the acute angle symmetrically expands upstream and compresses downstream.

This work employs the standard Oldroyd-B formulation rather than log-conformation methods, which are typically regarded as more numerically stable [76, 144], so the simulation with parameters $Wi = 14$ and $Re = 0.01$ was undertaken to evaluate the stability of the numerical scheme for elevated Weissenberg numbers. Figure 6.20 displays the outcomes of the simulation, illustrating the magnitudes of the velocity field and the components of the extra-stress tensor. The streamlines generated by the LIC technique are superimposed on the contour plots to verify the accurately converged solution of the velocity field and vortex configuration. Afonso et al. [145] along with other comparable studies [76, 144, 146] indicate that high Weissenberg-number computations can solely be executed using the log-conformation method, while the conventional stress formulation consistently diverges. This study, grounded in the conventional methodology for the extra-stress tensor and aimed at proposing a Lagrangian reformulation for viscoelastic flows, does not yet elucidate the stability of simulations across diverse point-cloud resolutions and elevated Wi numbers. The Lagrangian CFL condition (5.30), governing adaptive time stepping, establishes a sufficient stability criterion ensuring that the PPE can produce a pressure field that maintains simulations as incompressible and stable.

The components of the extra-stress tensor $\boldsymbol{\tau}_p$ indicate that the viscoelastic stresses

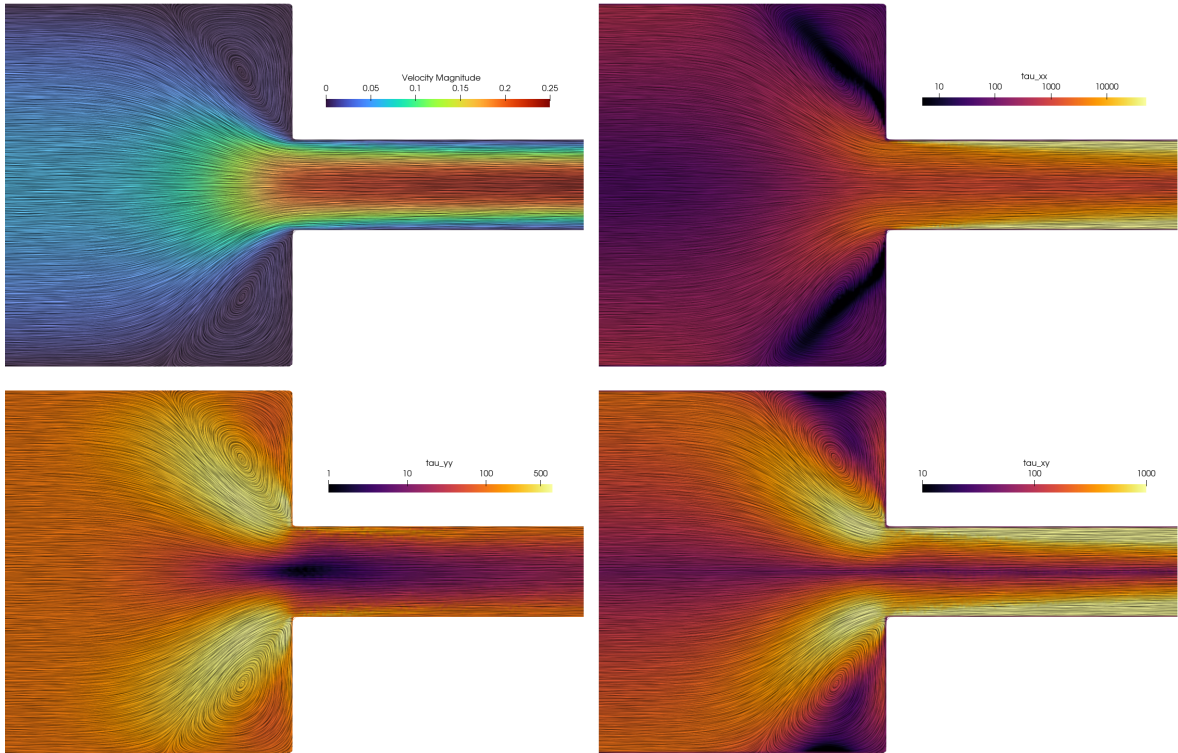


Figure 6.20: A contour plot illustrating the velocity magnitude (top left image) and the components of the extra-stress tensor for the 4:1 planar contraction simulation, $Wi = 14$ and $Re = 0.01$.

are significantly elevated in the horizontal direction, intensifying downstream within the narrow channel. At the acute corner, all tensor components exhibit comparable magnitudes, while the gradients of the component values near the contraction are pronounced. This intricate scenario is inducing significant viscoelastic accelerations in the fluid (through the term $\nabla \cdot \boldsymbol{\tau}_p$) as it is flowing around the corner. Thus, the pressure gradient is exceedingly high at the corner to maintain incompressible flow. A minor upstream curvature of streamlines is observable at the corner lip, attributable to these gradients. Complete lip vortices are formed for smaller Weissenberg numbers, as illustrated in Figure 6.18. Instabilities reported by certain other numerical methods have not been detected in the LDD simulations. Subsequent research should examine the impact of shear bands on vortices [149].

6.2.4 Die swelling

The phenomenon of die swell, or the post-extrusion expansion of a polymer melt, is significant in polymer processing as it serves as a critical benchmark for assessing the efficacy of viscoelastic flow solvers. The die swell problem serves as an effective measure of solver accuracy due to its heightened sensitivity to the constitutive modeling of viscoelastic properties. To accurately depict the material's behavior post-die exit,

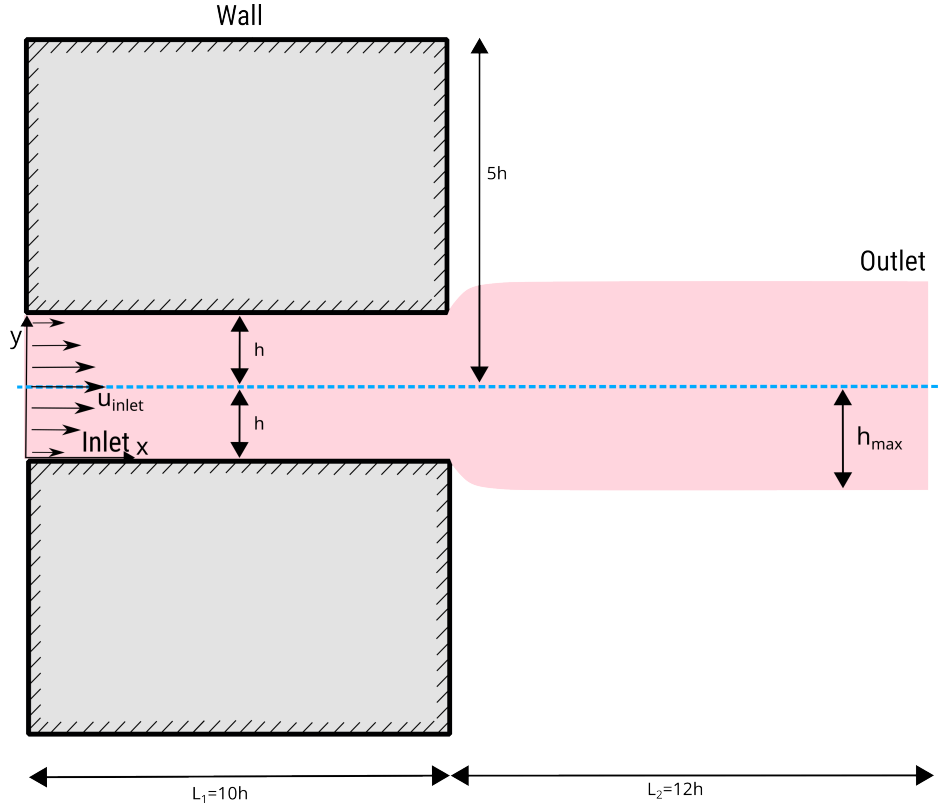


Figure 6.21: Schematic depiction of the computational domain and arrangement of the die-swell experiment.

the solver must integrate the complicated nature of the stress-strain relationship, addressing discontinuities in geometry and stress distributions. The die swell experiment is transient; however, the swell ratio progresses until a steady state is attained [150, 1]. Figure 6.21 presents a schematic illustration of the numerical domain for the experiment of die swelling in two dimensions. The fluid is simulated within a channel that has height of $2h$ and length of $10h$, while the expansion area is $12h$ long, meaning that the total domain length is $22h$. The swell domain is designed such that the boundary conditions at the inlet do not influence the flow near the channel exit.

The main dimension was taken $h = 0.01$ m, and two initial point-spacing values were tested, $\Delta = 0.0005$ and $\Delta = 0.0002$. The evolution of the free surface, captured during the first 16 seconds of the simulation for $Wi = 0.5$, is shown in Figure 6.22. The simulated swell is corresponding to the numerically obtained results by [1]. The simulations' results are compared to Tanner's theory, and data from [150] and [1], and the comparison is presented in Figure 6.23. The swell ratio is calculated for the simulation results as $S_r = h_{max}/h$, i.e. as the ratio of swell width measured away from the channel and the channel width. To obtain a comprehensive understanding of the cases and numerical methods, please refer to the corresponding studies. The study by [150] utilized an alternative definition of the Weissenberg number and swell ratio, which is acknowledged by [1] and thus also included in Figure 6.23. Comminal et al.

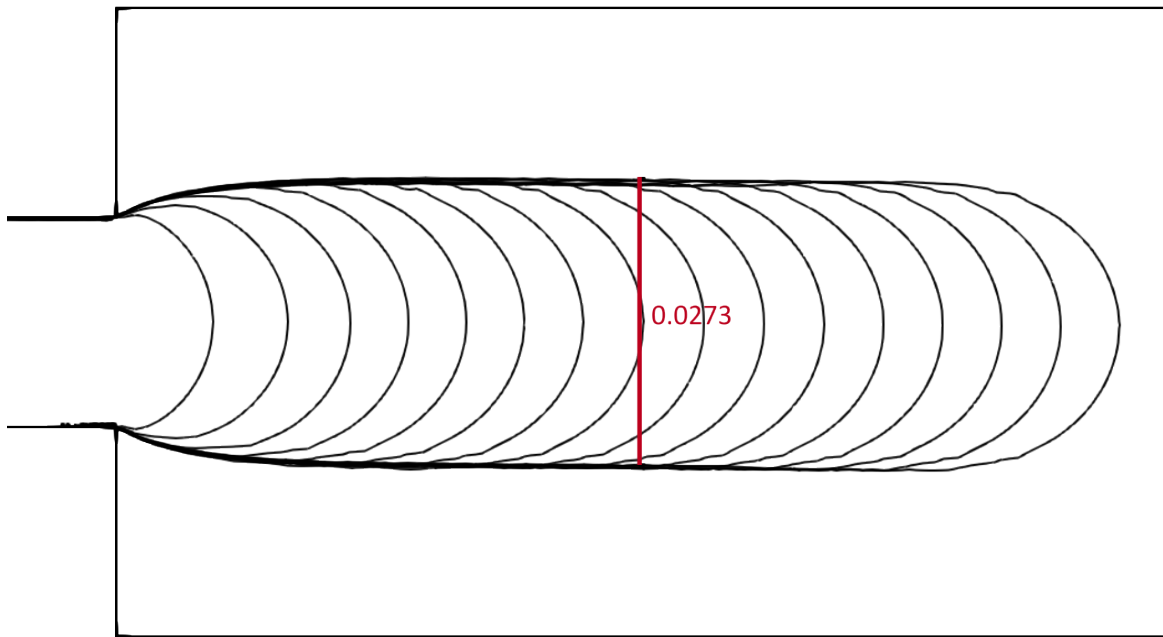


Figure 6.22: Images of the free surface from the die-swell simulation, using $Wi = 0.5$ and $Re = 0.5$. The progression of the free-surface (one contour per one simulation second) is juxtaposed with the swell ratio in [1].

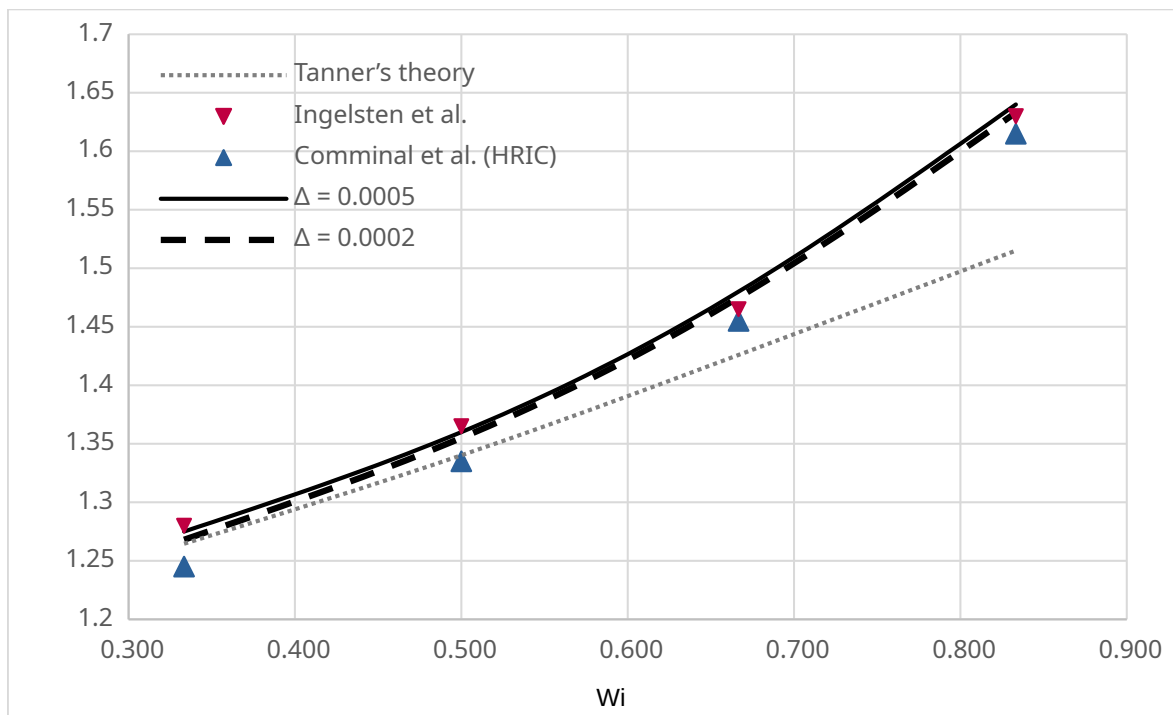


Figure 6.23: Comparison of the evolution of the die swelling, for several Weissenberg numbers ranging from 0.333 to 0.833.

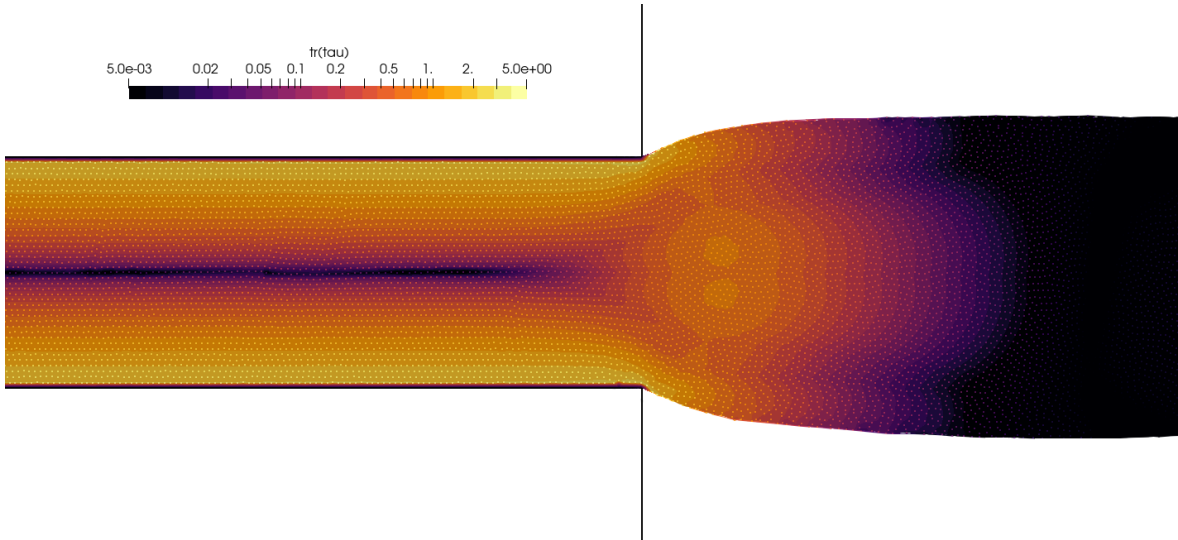


Figure 6.24: Contour plot of the instantaneous values of the trace of the extra-stress tensor, for the simulated die-swell experiment, using $Wi = 0.5$ and $Re = 0.5$. The points are also plotted to demonstrated convergence of the point-cloud incompressibility.

obtained disparate results when employing three subtly distinct numerical methods to simulate the identical flow. Nevertheless, the results of LDD simulations are in a very good agreement to the referent data, while slightly overpredicting compared numerical methods for $Wi > 0.5$. A contour plot of an instantaneous trace of the extra-stress tensor is given in Figure 6.24, where it can be seen that the concentration of the extra-stress is building up near the corners of the channel exit and in the center after the channel exit, while it diminishes after reaching steady state.

7 Conclusions and Future Work

7.1 Conclusions

In this thesis, a novel meshless and Lagrangian method for simulating incompressible non-Newtonian and viscoelastic flows with free surfaces was introduced. The method extends the baseline meshless and Lagrangian method, named Lagrangian Differencing Dynamics (LDD), which employs mesh-free spatial operators derived from finite differences, in order to discretize and solve the generalized Navier-Stokes equations in Lagrangian form. It allows simulating complex fluid properties and behavior, varying in space and time, without the need for a computational mesh. The fully Lagrangian nature of the approach, combined with implicit solving of the decoupled pressure and velocity equations, enables the use of relatively large time steps while maintaining accuracy, stability, and performance. The method was efficiently parallelized on both CPU and GPU architectures, ensuring computational efficiency for large-scale simulations.

The accuracy and robustness of the extended LDD method and its implementation were demonstrated through extensive validation against experimental and numerical benchmarks for both non-Newtonian viscoplastic, and viscoelastic flows. Non-Newtonian flow simulations were conducted using the Bingham, Casson, and Power Law models, with results showing strong agreement with reference data. Square and skewed cavity simulations accurately captured recirculation patterns and discontinuous velocity conditions at moving wall boundaries. The method effectively resolved free-surface flow behavior in dam-break and slump tests, confirming its ability to handle yield stress materials and complex transient flow phenomena.

For viscoelastic flows, the method was extended to incorporate the influence of the viscoelasticity tensor within the pressure-Poisson and momentum equations, therefore, enabling the simulation of polymeric and elastic fluid behavior. The Oldroyd-B model was used to assess viscoelastic effects such as stress relaxation, configurational memory, and elongational viscosity. The proposed viscoelastic extension of the extended LDD method accurately reproduced flow features in lid-driven cavity tests, droplet impact simulations, 4:1 sudden contraction flows, and die-swell problems, demonstrating its ability to capture viscoelastic stresses, flow separations, and elongational behavior. The results aligned well with experimental and theoretical expectations, confirming

7 Conclusions and Future Work

the method's effectiveness in predicting viscoelastic flow patterns across a range of complex geometries.

Overall, the LDD method has proven to be a powerful and versatile framework for modeling both non-Newtonian viscoplastic and viscoelastic fluids in a Lagrangian setting. Its ability to handle large deformations, complex interfaces, and free surfaces makes it a strong candidate for applications in industrial processing, biological fluid mechanics, and multiphase flow simulations. The successful validation of this method against a variety of benchmark problems confirms its accuracy, stability, and computational efficiency, paving the way for further advancements in the simulation of complex fluid phenomena.

The final conclusion of this thesis may be summarised as:

Lagrangian meshless modeling is a powerful approach for simulating complex rheological flows, capturing large deformations, free surfaces, and stress behaviors with stability and efficiency.

7.2 Future work

Stability

The solver successfully handled the natural viscoelastic stress tensor formulation within the proposed Lagrangian meshless method, ensuring accurate stress evolution without the need for additional stabilization techniques. However, to further enhance numerical stability at high Weissenberg numbers, future work will focus on extending the method to incorporate advanced stress representations such as the logarithmic conformation tensor approach and its square-root variants. These formulations transform the stress evolution equations in a manner that mitigates numerical singularities and reduces spurious oscillations, thereby improving robustness in highly elastic flows. It will enable more stable and accurate simulations of complex viscoelastic flows in regimes where standard formulations encounter numerical difficulties.

Surface tension forces

Surface tension effects should be incorporated into the methodology, enabling the simulation of primary and secondary atomization in spraying processes involving non-Newtonian liquids. By coupling surface tension forces with the existing viscoelastic stress formulation, the method will be able to capture droplet formation, filament thinning, and breakup dynamics with greater accuracy. This enhancement will be particularly useful in applications such as fuel injection systems, pharmaceutical spray drying, agricultural pesticide spraying, and additive manufacturing processes like inkjet and 3D bioprinting. The inclusion of surface tension will provide critical insights into how material properties influence breakup mechanisms, helping to optimize industrial and biomedical applications that rely on controlled liquid dispersion. This extension will allow for modeling of complex interfacial phenomena, i.e. competition between elasticity and capillary forces, leading to better predictive capabilities for real-world systems.

Advanced constitutive models

Recognizing the limitations of the Oldroyd-B model, particularly its inability to accurately capture shear-dependent viscosity and extensional flow properties in highly non-linear viscoelastic behavior, future research will focus on implementing more advanced constitutive models. These models, such as the Giesekus model (for shear-thinning effects) or the Finitely Extensible Nonlinear Elastic (FENE) models (for polymer chain extensibility), offer a more realistic representation of complex viscoelastic fluid behavior. These models introduce additional complexity, requiring careful numerical

implementation and potentially leading to increased computational cost and stability challenges, which will be addressed through advanced numerical techniques and adaptive solution strategies.

Biology flows

Future work will focus on extending the solver implementation to accommodate deforming boundaries, enabling the simulation of complex biological systems such as the heart, heart valves, and other soft tissues. This extension will involve incorporating boundary evolution in time and space, that seamlessly integrate with the Lagrangian meshless framework while preserving accuracy and stability in viscoelastic stress computations. By allowing for dynamically moving and deforming geometries, the enhanced solver will be well-suited for modeling physiologically relevant flows and tissue mechanics, opening the door to more realistic simulations of biological fluids, where viscoelasticity plays a crucial role.

Geology flows

Future work will extend the solver to simulate volcanic lava flows and mudslides by incorporating advanced viscoplastic and viscoelastic rheological models. To accurately capture the behavior of lava, temperature-dependent viscosity models and heat transfer mechanisms will be added to account for cooling and solidification. This will enable realistic simulations of lava flow fronts, crust formation, and the transition from fluid-like to solid-like behavior. Additionally, the solver will be enhanced to support fluid-structure interaction (FSI) by coupling to discrete element method (DEM), allowing us to model interactions with solid debris, rocks, and sediments in mudslides and pyroclastic flows. The framework could provide a powerful tool for studying hazard prediction, mitigation strategies, and the fundamental dynamics of geophysical mass flows.

Turbulence in viscoelastic flows

A fundamental study on turbulent viscoelastic flows may be conducted, particularly investigating drag reduction and elastic turbulence at high Weissenberg numbers. By extending the solver stability to handle highly elastic flow regimes, the interplay between inertia, elasticity, and turbulence may be explored in both canonical and complex geometries. The implementation will incorporate advanced constitutive models such as the FENE-P and Giesekus models to accurately capture polymer stretching and nonlinear stress effects. These studies will provide deeper insights into mechanisms of

7 Conclusions and Future Work

viscoelastic drag reduction, relevant to energy-efficient fluid transport in pipelines and aerospace applications, as well as the onset and characteristics of elastic turbulence in microfluidic and industrial processes. Ultimately, this research will contribute to a more comprehensive understanding of non-Newtonian turbulence and its potential applications in engineering and natural flow systems.

Bibliography

- [1] Simon Ingelsten, Andreas Mark, Roland Kádár, and Fredrik Edelvik. A Backwards-Tracking Lagrangian-Eulerian Method for Viscoelastic Two-Fluid Flows. *Applied Sciences*, 11(1):439, jan 2021. doi:[10.3390/app11010439](https://doi.org/10.3390/app11010439).
- [2] Eugene Cook Bingham. *Fluidity and plasticity*. New York McGraw-Hill Book Company, Inc., New York, New York, USA, 1922.
- [3] Hongna Zhang, Wenhua Zhang, Xinyi Wang, Yansong Li, Xiaobin Li, and Fengchen Li. On the role of tensor interpolation in solving high-WI viscoelastic fluid flow. *Physics of Fluids*, 35(3), mar 2023. URL: <https://pubs.aip.org/pof/article/35/3/031708/2881590/On-the-role-of-tensor-interpolation-in-solving>, doi: [10.1063/5.0141639](https://doi.org/10.1063/5.0141639).
- [4] Josip Bašić, Nastia Degiuli, Šime Malenica, and Dario Ban. Lagrangian finite-difference method for predicting green water loadings. *Ocean Engineering*, 209:107533, aug 2020. doi:[10.1016/j.oceaneng.2020.107533](https://doi.org/10.1016/j.oceaneng.2020.107533).
- [5] Martina Bašić, Branko Blagojević, Chong Peng, and Josip Bašić. Lagrangian Differencing Dynamics for Time-Independent Non-Newtonian Materials. *Materials*, 14(20):6210, oct 2021. doi:[10.3390/ma14206210](https://doi.org/10.3390/ma14206210).
- [6] Chong Peng, Martina Bašić, Branko Blagojević, Josip Bašić, and Wei Wu. A Lagrangian differencing dynamics method for granular flow modeling. *Computers and Geotechnics*, 137:104297, sep 2021. doi:[10.1016/j.compgeo.2021.104297](https://doi.org/10.1016/j.compgeo.2021.104297).
- [7] Josip Bašić, Nastia Degiuli, Branko Blagojević, and Dario Ban. Lagrangian differencing dynamics for incompressible flows. *Journal of Computational Physics*, 462:111198, aug 2022. doi:[10.1016/j.jcp.2022.111198](https://doi.org/10.1016/j.jcp.2022.111198).
- [8] Kanishka Bhattacharya, Tapan Kumar Jana, Amit Shaw, L S Ramachandra, and Vishal Mehera. An adaptive approach to remove tensile instability in SPH for weakly compressible fluids. *ArXiv*, abs/2307.0, 2023. URL: <https://api.semanticscholar.org/CorpusID:259837237>.
- [9] X J Fan, R I Tanner, and R Zheng. Smoothed particle hydrodynamics simulation of non-Newtonian moulding flow. *Journal of Non-Newtonian Fluid Mechanics*, 2010. doi:[10.1016/j.jnnfm.2009.12.004](https://doi.org/10.1016/j.jnnfm.2009.12.004).

Bibliography

- [10] Jiannong Fang, Robert G Owens, Laurent Tacher, and Aurèle Parriaux. A numerical study of the SPH method for simulating transient viscoelastic free surface flows. *Journal of Non-Newtonian Fluid Mechanics*, 2006. doi:10.1016/j.jnnfm.2006.07.004.
- [11] Xiaoyang Xu, Jie Ouyang, Binxin Yang, and Zhijun Liu. SPH simulations of three-dimensional non-Newtonian free surface flows. *Computer Methods in Applied Mechanics and Engineering*, 256:101–116, apr 2013. URL: <https://linkinghub.elsevier.com/retrieve/pii/S0045782512003878>, doi:10.1016/j.cma.2012.12.017.
- [12] Xiaoyang Xu and Peng Yu. A technique to remove the tensile instability in weakly compressible SPH. *Computational Mechanics*, 62(5):963–990, nov 2018. URL: <https://api.semanticscholar.org/CorpusID:125802492><http://link.springer.com/10.1007/s00466-018-1542-4>, doi:10.1007/s00466-018-1542-4.
- [13] Christophe Ancey. Plasticity and geophysical flows: A review. *Journal of Non-Newtonian Fluid Mechanics*, 142(1-3):4–35, mar 2007. URL: <https://linkinghub.elsevier.com/retrieve/pii/S037702570600108X>, doi:10.1016/j.jnnfm.2006.05.005.
- [14] Markus Reiner and R Schoenfeld-Reiner. Viskosimetrische Untersuchungen an Lösungen hochmolekularer Naturstoffe. I. Mitteilung. Kautschuk in Toluol. *Kolloid-Zeitschrift*, 1933. doi:10.1007/BF01428857.
- [15] N Casson. A Flow Equation for Pigment-Oil Suspensions of the Printing Ink Type. Rheology of Disperse System. In *Proceedings of a Conference Organized by the British Society of Rheology*, 1959.
- [16] Raphaël Comminal, Jon Spangenberg, and Jesper Henri Hattel. Robust simulations of viscoelastic flows at high Weissenberg numbers with the streamfunction/log-conformation formulation. *Journal of Non-Newtonian Fluid Mechanics*, 223:37–61, 2015. doi:10.1016/j.jnnfm.2015.05.003.
- [17] J H Snoeijer, A Pandey, M A Herrada, and J Eggers. The relationship between viscoelasticity and elasticity. *Proceedings of the Royal Society A: Mathematical, Physical and Engineering Sciences*, 476(2243):20200419, nov 2020. URL: <https://royalsocietypublishing.org/doi/10.1098/rspa.2020.0419>, doi:10.1098/rspa.2020.0419.
- [18] M.A. Alves, P.J. Oliveira, and F.T. Pinho. Numerical Methods for Viscoelastic Fluid Flows. *Annual Review of Fluid Mechanics*, 53(1):509–541, 2021. doi:10.1146/annurev-fluid-010719-060107.

Bibliography

- [19] J G Oldroyd. On the formulation of rheological equations of state. *Proceedings of the Royal Society of London. Series A. Mathematical and Physical Sciences*, 200(1063):523–541, feb 1950. URL: <https://royalsocietypublishing.org/doi/10.1098/rspa.1950.0035>, doi:10.1098/rspa.1950.0035.
- [20] Hugo A Castillo Sánchez, Mihailo R Jovanović, Satish Kumar, Alexander Morozov, V Shankar, Ganesh Subramanian, and Helen J Wilson. Understanding viscoelastic flow instabilities: Oldroyd-B and beyond. *Journal of Non-Newtonian Fluid Mechanics*, 302:104742, apr 2022. URL: <https://linkinghub.elsevier.com/retrieve/pii/S0377025722000015>, doi:10.1016/j.jnnfm.2022.104742.
- [21] Qinlong Ren. Investigation of pumping mechanism for non-Newtonian blood flow with AC electrothermal forces in a microchannel by hybrid boundary element method and immersed boundary-lattice Boltzmann method. *ELECTROPHORESIS*, 39(11):1329–1338, jun 2018. URL: <https://analyticalsciencejournals.onlinelibrary.wiley.com/doi/10.1002/elps.201700494>, doi:10.1002/elps.201700494.
- [22] R Jecl, L Skerget, and E Petresin. BEM for natural convection in non-Newtonian fluid saturated porous cavity. 2002.
- [23] R Jecl and L Skerget. Boundary element method for natural convection in non-Newtonian fluid saturated square porous cavity. *Engineering Analysis With Boundary Elements*, 27:963–975, 2003.
- [24] W Flórez, H Power, and F Chejne. Mult-domain DRM boundary element method for non-isothermal non-Newtonian Stokes flow with viscous dissipation. *International Journal of Numerical Methods for Heat & Fluid Flow*, 13:736–768, 2003.
- [25] M Giraldo, H Power, and W Flórez. Numerical simulation of the motion and deformation of a non-Newtonian shear-thinning drop suspended in a Newtonian circular Couette flow using DR-BEM. *Engineering Analysis With Boundary Elements*, 33:93–104, 2009.
- [26] N T Eldabe, A Ghaly, Raafat R Rizkallah, K M Ewis, and Ameen S Al-Bareda. Numerical Solution of MHD Boundary Layer Flow of Non-Newtonian Casson Fluid on a Moving Wedge with Heat and Mass Transfer and Induced Magnetic Field. *Journal of Applied Mathematics and Physics*, 03:649–663, 2015.
- [27] D Malkus and M F Webster. On the Accuracy of Finite Element and Finite Difference Predictions of Non-Newtonian Slot Pressures for a Maxwell Fluid. *Journal of Non-newtonian Fluid Mechanics*, 25:93–127, 1987.
- [28] D Sankar and U Lee. FDM analysis for MHD flow of a non-Newtonian fluid for blood flow in stenosed arteries. *Journal of Mechanical Science and Technology*, 25:2573–2581, 2011.

Bibliography

- [29] Hugo A Castillo-Sánchez, Leandro F de Souza, and Antonio Castelo. Numerical Simulation of Rheological Models for Complex Fluids Using Hierarchical Grids. *Polymers*, 14(22), 2022. URL: <https://www.mdpi.com/2073-4360/14/22/4958>, doi:10.3390/polym14224958.
- [30] Hugo Alberto Castillo Sánchez, Juliana Bertoco, Antonio Castelo, and Manoel Silvino Batalha de Araújo. Numerical Simulation of a Thixotropic-Viscoelastic Model in Expansion-Contraction Geometries. *SSRN Electronic Journal*, 2022. URL: <https://www.ssrn.com/abstract=4048814>, doi:10.2139/ssrn.4048814.
- [31] Antonio Castelo, Alexandre M Afonso, and Wesley De Souza Bezerra. A Hierarchical Grid Solver for Simulation of Flows of Complex Fluids. *Polymers*, 13(18), 2021. URL: <https://www.mdpi.com/2073-4360/13/18/3168>, doi:10.3390/polym13183168.
- [32] Michel Fortin and André Fortin. A new approach for the FEM simulation of viscoelastic flows. *Journal of Non-Newtonian Fluid Mechanics*, 1989. doi:10.1016/0377-0257(89)85012-8.
- [33] M J Szady, T R Salamon, A W Liu, D E Bornside, R C Armstrong, and R A Brown. A new mixed finite element method for viscoelastic flows governed by differential constitutive equations. *Journal of Non-Newtonian Fluid Mechanics*, 1995. doi:10.1016/0377-0257(95)01370-B.
- [34] Anne M Grillet, Bin Yang, Bamin Khomami, and Eric S G Shaqfeh. Modeling of viscoelastic lid driven cavity flow using finite element simulations. *Journal of Non-Newtonian Fluid Mechanics*, 1999. doi:10.1016/S0377-0257(99)00015-4.
- [35] Jiří Křen and Luděk Hynčák. Modelling of non-Newtonian fluids. *Mathematics and Computers in Simulation*, 2007. doi:10.1016/j.matcom.2007.01.006.
- [36] R R Huilgol and G H R Kefayati. Natural convection problem in a Bingham fluid using the operator-splitting method. *Journal of Non-Newtonian Fluid Mechanics*, 2015. doi:10.1016/j.jnnfm.2014.06.005.
- [37] A.T. Mackay and T.N. Phillips. Computational modelling of compressible non-isothermal viscoelastic fluids. *Computers & Fluids*, 272:106189, mar 2024. URL: <https://linkinghub.elsevier.com/retrieve/pii/S0045793024000215>, doi:10.1016/j.compfluid.2024.106189.
- [38] Panagiotis Neofytou. A 3rd order upwind finite volume method for generalised Newtonian fluid flows. *Advances in Engineering Software*, 36(10):664–680, oct 2005. URL: <https://linkinghub.elsevier.com/retrieve/pii/S0965997805000578>, doi:10.1016/j.advengsoft.2005.03.011.

Bibliography

- [39] Shun Zou, Xue Feng Yuan, Xuejun Yang, Wei Yi, and Xinhai Xu. An integrated lattice Boltzmann and finite volume method for the simulation of viscoelastic fluid flows. *Journal of Non-Newtonian Fluid Mechanics*, 2014. doi:10.1016/j.jnnfm.2014.07.003.
- [40] S. De, S. Das, J.A.M. A M Kuipers, E.A.J.F. A J F Peters, and J.T. T Padding. A coupled finite volume immersed boundary method for simulating 3D viscoelastic flows in complex geometries. *Journal of Non-Newtonian Fluid Mechanics*, 232:67–76, jun 2016. URL: <https://linkinghub.elsevier.com/retrieve/pii/S0377025716300374>, doi:10.1016/j.jnnfm.2016.04.002.
- [41] S De, J A M Kuipers, E A J F Peters, and J T Padding. Viscoelastic flow simulations in random porous media. *Journal of Non-Newtonian Fluid Mechanics*, 2017. doi:10.1016/j.jnnfm.2017.08.010.
- [42] Stefanie Meburger, Matthias Niethammer, Dieter Bothe, and Michael Schäfer. Numerical simulation of non-isothermal viscoelastic flows at high Weissenberg numbers using a finite volume method on general unstructured meshes. *Journal of Non-Newtonian Fluid Mechanics*, 287:104451, jan 2021. URL: <https://linkinghub.elsevier.com/retrieve/pii/S0377025720301932><https://www.sciencedirect.com/science/article/pii/S0377025720301932>, doi:10.1016/j.jnnfm.2020.104451.
- [43] Massimiliano Cremonesi, Alessandro Franci, Sergio Idelsohn, and Eugenio Oñate. A State of the Art Review of the Particle Finite Element Method (PFEM). *Archives of Computational Methods in Engineering*, 27(5):1709–1735, nov 2020. URL: <https://link.springer.com/10.1007/s11831-020-09468-4>, doi:10.1007/s11831-020-09468-4.
- [44] F Salazar, J Irazábal, A Larese, and E Oñate. Numerical modelling of landslide-generated waves with the particle finite element method (PFEM) and a non-Newtonian flow model. *International Journal for Numerical and Analytical Methods in Geomechanics*, 2016. doi:10.1002/nag.2428.
- [45] Miguel Angel Celigueta, Kedar M Deshpande, Salvador Latorre, and Eugenio Oñate. A FEM-DEM technique for studying the motion of particles in non-Newtonian fluids. Application to the transport of drill cuttings in wellbores. *Computational Particle Mechanics*, 2016. doi:10.1007/s40571-015-0090-3.
- [46] Massimiliano Cremonesi, Simone Meduri, Umberto Perego, and Attilio Frangi. An explicit Lagrangian finite element method for free-surface weakly compressible flows. *Computational Particle Mechanics*, 2017. doi:10.1007/s40571-016-0122-7.

Bibliography

- [47] A Laresse. A Lagrangian PFEM approach for non-Newtonian viscoplastic materials. *Revista Internacional de Metodos Numericos para Calculo y Diseno en Ingenieria*, 2017. doi:[10.1016/j.rimni.2016.07.002](https://doi.org/10.1016/j.rimni.2016.07.002).
- [48] Alessandro Franci and Xue Zhang. 3D numerical simulation of free-surface Bingham fluids interacting with structures using the PFEM. *Journal of Non-Newtonian Fluid Mechanics*, 259:1–15, sep 2018. URL: <https://linkinghub.elsevier.com/retrieve/pii/S0377025718300399>, doi:[10.1016/j.jnnfm.2018.05.001](https://doi.org/10.1016/j.jnnfm.2018.05.001).
- [49] Gabriele Della Vecchia, Massimiliano Cremonesi, and Federico Pisanò. On the rheological characterisation of liquefied sands through the dam-breaking test. *International Journal for Numerical and Analytical Methods in Geomechanics*, 2019. doi:[10.1002/nag.2905](https://doi.org/10.1002/nag.2905).
- [50] Giacomo Rizzieri, Liberato Ferrara, and Massimiliano Cremonesi. Simulation of viscoelastic free-surface flows with the Particle Finite Element Method. *Computational Particle Mechanics*, 11(5):2043–2067, oct 2024. URL: <https://link.springer.com/10.1007/s40571-024-00730-1>, doi:[10.1007/s40571-024-00730-1](https://doi.org/10.1007/s40571-024-00730-1).
- [51] F. Serafini, F. Battista, P. Gualtieri, and C.M. Casciola. The role of polymer parameters and configurations in drag-reduced turbulent wall-bounded flows: Comparison between FENE and FENE-P. *International Journal of Multiphase Flow*, 165:104471, aug 2023. URL: <https://linkinghub.elsevier.com/retrieve/pii/S0301932223000927>, doi:[10.1016/j.ijmultiphaseflow.2023.104471](https://doi.org/10.1016/j.ijmultiphaseflow.2023.104471).
- [52] Peter A. Gordon, Fushen Liu, Holger A. Meier, Rohan Panchadhara, and Vikas Srivastava. A material point method for simulation of viscoelastic flows. *Computational Particle Mechanics*, 6(3):311–325, jul 2019. URL: <http://link.springer.com/10.1007/s40571-018-0215-6>, doi:[10.1007/s40571-018-0215-6](https://doi.org/10.1007/s40571-018-0215-6).
- [53] Tianjie Zhang, Donglei Wang, and Yang Lu. A Navier–Stokes-Informed Neural Network for Simulating the Flow Behavior of Flowable Cement Paste in 3D Concrete Printing. *Buildings*, 15(2):275, jan 2025. URL: <https://www.mdpi.com/2075-5309/15/2/275>, doi:[10.3390/buildings15020275](https://doi.org/10.3390/buildings15020275).
- [54] Salah A Faroughi, Ana I Roriz, and Célio Fernandes. A Meta-Model to Predict the Drag Coefficient of a Particle Translating in Viscoelastic Fluids: A Machine Learning Approach. *Polymers*, 14(3), 2022. URL: <https://www.mdpi.com/2073-4360/14/3/430>, doi:[10.3390/polym14030430](https://doi.org/10.3390/polym14030430).
- [55] Xiaomin Zhou and Zheng Sun. Numerical investigation of non-Newtonian power law flows using B-spline material point method. *Journal of Non-Newtonian Fluid*

Bibliography

- Mechanics*, 298:104678, dec 2021. URL: <https://linkinghub.elsevier.com/retrieve/pii/S0377025721001622>, doi:10.1016/j.jnnfm.2021.104678.
- [56] Xiaomin Zhou, Yunjun Hua, and Zheng Sun. Application of Cross model for granular flow and impact analysis using three-dimensional B-spline material point method. *Journal of Non-Newtonian Fluid Mechanics*, 322:105145, dec 2023. URL: <https://linkinghub.elsevier.com/retrieve/pii/S037702572300157X>, doi:10.1016/j.jnnfm.2023.105145.
- [57] Haozhe Su, Tao Xue, Chengguizi Han, Chenfanfu Jiang, and Mridul Aanjaneya. A unified second-order accurate in time MPM formulation for simulating viscoelastic liquids with phase change. *ACM Transactions on Graphics*, 40(4):1–18, aug 2021. URL: <https://dl.acm.org/doi/10.1145/3476576.3476687>, doi:10.1145/3476576.3476687.
- [58] Xingyue Li, Betty Sovilla, Chenfanfu Jiang, and Johan Gaume. Three-dimensional and real-scale modeling of flow regimes in dense snow avalanches. *Landslides*, 18(10):3393–3406, oct 2021. URL: <https://link.springer.com/10.1007/s10346-021-01692-8>, doi:10.1007/s10346-021-01692-8.
- [59] Xinpo Li, Jun Yao, Yulian Sun, and Yong Wu. Material point method analysis of fluid–structure interaction in geohazards. *Natural Hazards*, 114(3):3425–3443, dec 2022. URL: <https://link.springer.com/10.1007/s11069-022-05526-1>, doi:10.1007/s11069-022-05526-1.
- [60] Francesca Ceccato, Alba Yerro, and Gaia Di Carluccio. Simulating landslides with the material point method: Best practices, potentialities, and challenges. *Engineering Geology*, 338:107614, aug 2024. URL: <https://linkinghub.elsevier.com/retrieve/pii/S001379522400214X>, doi:10.1016/j.enggeo.2024.107614.
- [61] Shyamini Kularathna, Weijian Liang, Tianchi Zhao, Bodhinanda Chandra, Jidong Zhao, and Kenichi Soga. A semi-implicit material point method based on fractional-step method for saturated soil. *International Journal for Numerical and Analytical Methods in Geomechanics*, 45(10):1405–1436, jul 2021. URL: <https://onlinelibrary.wiley.com/doi/10.1002/nag.3207>, doi:10.1002/nag.3207.
- [62] J J Monaghan. Smoothed particle hydrodynamics and its diverse applications. *Annual Review of Fluid Mechanics*, 2011. doi:10.1146/annurev-fluid-120710-101220.
- [63] R. a. Gingold and J. J. Monaghan. Smoothed particle hydrodynamics-theory and application to non-spherical stars. *Monthly Notices of the Royal Astronomical*

Bibliography

- Society*, 181:375–389, 1977. [arXiv:arXiv:1011.1669v3](#), [doi:10.1093/mnras/181.3.375](#).
- [64] L. B. Lucy. A numerical approach to the testing of the fission hypothesis. *The Astronomical Journal*, 82:1013, 1977. [arXiv:9809069v1](#), [doi:10.1086/112164](#).
- [65] A.M. Xenakis, S.J. Lind, P.K. Stansby, and B.D. Rogers. An incompressible SPH scheme with improved pressure predictions for free-surface generalised Newtonian flows. *Journal of Non-Newtonian Fluid Mechanics*, 218:1–15, 2015. [doi:10.1016/j.jnnfm.2015.01.006](#).
- [66] Songdong Shao and Edmond Y.M. Lo. Incompressible SPH method for simulating Newtonian and non-Newtonian flows with a free surface. *Advances in Water Resources*, 26(7):787–800, 2003. [doi:10.1016/S0309-1708\(03\)00030-7](#).
- [67] S M Hosseini, M T Manzari, and S K Hannani. A fully explicit three-step SPH algorithm for simulation of non-Newtonian fluid flow. *International Journal of Numerical Methods for Heat and Fluid Flow*, 2007. [doi:10.1108/09615530710777976](#).
- [68] Xiaojing Ma, Bowen Zhang, Jie Chen, Xinchao Zhou, and Wei Chen. The simulation of sediment transport and erosion caused by free-surface flow based on two-phase SPH model with the improved Shields criterion. *Ocean Dynamics*, 72(2):169–186, feb 2022. URL: <https://link.springer.com/10.1007/s10236-022-01497-w>, [doi:10.1007/s10236-022-01497-w](#).
- [69] J.R.C. King and S.J. Lind. High Weissenberg number simulations with incompressible Smoothed Particle Hydrodynamics and the log-conformation formulation. *Journal of Non-Newtonian Fluid Mechanics*, 293:104556, jul 2021. URL: <https://linkinghub.elsevier.com/retrieve/pii/S0377025721000690>, [doi:10.1016/j.jnnfm.2021.104556](#).
- [70] Huaning Zhu, Nicos S Martys, Chiara Ferraris, and Daniel De Kee. A numerical study of the flow of Bingham-like fluids in two-dimensional vane and cylinder rheometers using a smoothed particle hydrodynamics (SPH) based method. *Journal of Non-Newtonian Fluid Mechanics*, 2010. [doi:10.1016/j.jnnfm.2010.01.012](#).
- [71] Tasos C Papanastasiou. Flows of Materials with Yield. *Journal of Rheology*, 31(5):385–404, jul 1987. URL: <http://sor.scitation.org/doi/10.1122/1.549926>, [doi:10.1122/1.549926](#).
- [72] Raanan Fattal and Raz Kupferman. Constitutive laws for the matrix-logarithm of the conformation tensor. *Journal of Non-Newtonian Fluid Mechanics*, 123(2):281–285, 2004. URL: <https://www.sciencedirect.com/science/article/pii/S0377025704002630>, [doi:10.1016/j.jnnfm.2004.08.008](#).

Bibliography

- [73] Martien A Hulsen, Raanan Fattal, and Raz Kupferman. Flow of viscoelastic fluids past a cylinder at high Weissenberg number: Stabilized simulations using matrix logarithms. *Journal of Non-Newtonian Fluid Mechanics*, 127(1):27–39, 2005. URL: <https://www.sciencedirect.com/science/article/pii/S0377025705000455>, doi:10.1016/j.jnnfm.2005.01.002.
- [74] F Pimenta and M A Alves. Stabilization of an open-source finite-volume solver for viscoelastic fluid flows. *Journal of Non-Newtonian Fluid Mechanics*, 239:85–104, 2017. URL: <https://www.sciencedirect.com/science/article/pii/S0377025716303329>, doi:10.1016/j.jnnfm.2016.12.002.
- [75] Florian Habla, Ming Wei Tan, Johannes Haßlberger, and Olaf Hinrichsen. Numerical simulation of the viscoelastic flow in a three-dimensional lid-driven cavity using the log-conformation reformulation in OpenFOAM®. *Journal of Non-Newtonian Fluid Mechanics*, 2014. doi:10.1016/j.jnnfm.2014.08.005.
- [76] Célio Fernandes. A Fully Implicit Log-Conformation Tensor Coupled Algorithm for the Solution of Incompressible Non-Isothermal Viscoelastic Flows. *Polymers*, 14(19):4099, sep 2022. URL: <https://www.mdpi.com/2073-4360/14/19/4099>, doi:10.3390/polym14194099.
- [77] Raanan Fattal and Raz Kupferman. Time-dependent simulation of viscoelastic flows at high Weissenberg number using the log-conformation representation. *Journal of Non-Newtonian Fluid Mechanics*, 126(1):23–37, feb 2005. URL: <https://linkinghub.elsevier.com/retrieve/pii/S0377025705000042>, doi:10.1016/j.jnnfm.2004.12.003.
- [78] Wilco M.H. Verbeeten, Gerrit W.M. Peters, and Frank P.T. Baaijens. Numerical simulations of the planar contraction flow for a polyethylene melt using the XPP model. *Journal of Non-Newtonian Fluid Mechanics*, 117(2-3):73–84, feb 2004. URL: <https://linkinghub.elsevier.com/retrieve/pii/S0377025704000047>, doi:10.1016/j.jnnfm.2003.12.003.
- [79] Lingjie Ke and Qikun Wang. Numerical Simulation of the Stability of Low Viscosity Ratio Viscoelastic Lid-Driven Cavity Flow Based on the Log-Conformation Representation (LCR) Algorithm. *Mathematics*, 12(3):430, jan 2024. URL: <https://www.mdpi.com/2227-7390/12/3/430>, doi:10.3390/math12030430.
- [80] C Fernandes, M S B Araujo, L L Ferrás, and J Miguel Nóbrega. Improved both sides diffusion (iBSD): A new and straightforward stabilization approach for viscoelastic fluid flows. *Journal of Non-Newtonian Fluid Mechanics*, 249:63–78, nov 2017. URL: <https://linkinghub.elsevier.com/retrieve/pii/S0377025717301003>, doi:10.1016/j.jnnfm.2017.09.008.
- [81] Claudio Giorgi and Angelo Morro. Nonlinear Models of Thermo-Viscoelastic

Bibliography

- Materials. *Materials*, 14(24), 2021. URL: <https://www.mdpi.com/1996-1944/14/24/7617>, doi:10.3390/ma14247617.
- [82] Patrick Westervof, Stefan Turek, Hogenrich Damanik, and Abderrahim Ouazzi. The Tensor Diffusion approach for simulating viscoelastic fluids. *Journal of Non-Newtonian Fluid Mechanics*, 286:104431, dec 2020. URL: <https://linkinghub.elsevier.com/retrieve/pii/S0377025720301816>, doi:10.1016/j.jnnfm.2020.104431.
- [83] Chandi Sasmal. Electro-Elastic Instability and Turbulence in Electro-osmotic Flows of Viscoelastic Fluids: Current Status and Future Directions. *Micromachines*, 16(2):187, feb 2025. URL: <https://www.mdpi.com/2072-666X/16/2/187>, doi:10.3390/mi16020187.
- [84] S. Gupta and C. Sasmal. Effect of cavity aspect ratio on mixed convective heat transfer phenomenon inside a lid-driven cavity due to elastic turbulence. *Physics of Fluids*, 35(3), mar 2023. URL: <https://pubs.aip.org/pof/article/35/3/033114/2881958/Effect-of-cavity-aspect-ratio-on-mixed-convective>, doi:10.1063/5.0143472.
- [85] A C Brandi, M T Mendonça, and L F Souza. DNS and LST stability analysis of Oldroyd-B fluid in a flow between two parallel plates. *Journal of Non-Newtonian Fluid Mechanics*, 267:14–27, 2019. URL: <https://www.sciencedirect.com/science/article/pii/S0377025718301344>, doi:10.1016/j.jnnfm.2019.03.003.
- [86] Zheng-Gang Su, Tian-Fu Li, Kang Luo, and Hong-Liang Yi. Nonlinear behavior of electrohydrodynamic flow in viscoelastic fluids. *Physical Review Fluids*, 6(9):093701, sep 2021. URL: <https://link.aps.org/doi/10.1103/PhysRevFluids.6.093701>, doi:10.1103/PhysRevFluids.6.093701.
- [87] M. Andrun, D. Ban, J. Bašić, and B. Ljubenkov. TSHD ship opening simulation by discrete element method. *Applied Ocean Research*, 94:102001, jan 2020. URL: <https://linkinghub.elsevier.com/retrieve/pii/S0141118719303396>, doi:10.1016/j.apor.2019.102001.
- [88] T N Phillips and A J Williams. Viscoelastic flow through a planar contraction using a semi-Lagrangian finite volume method. *Journal of Non-Newtonian Fluid Mechanics*, 87(2-3):215–246, nov 1999. URL: <https://linkinghub.elsevier.com/retrieve/pii/S0377025799000658>, doi:10.1016/S0377-0257(99)00065-8.
- [89] Yue Mu, Guoqun Zhao, Xianghong Wu, and Jiqiang Zhai. Modeling and simulation of three-dimensional planar contraction flow of viscoelastic fluids with PTT,

Bibliography

- Giesekus and FENE-P constitutive models. *Appl. Math. Comput.*, 218:8429–8443, 2012.
- [90] Mohammad Hemmat Esfe and Mohammad Reza Sarlak. Experimental investigation of switchable behavior of CuO-MWCNT (85%–15%)/10W-40 hybrid nanolubricants for applications in internal combustion engines. *Journal of Molecular Liquids*, 2017. doi:10.1016/j.molliq.2017.06.075.
- [91] Josip Basic, Nastia Degiuli, and Dario Ban. A class of renormalised meshless Laplacians for boundary value problems. *Journal of Computational Physics*, 354:269–287, feb 2018. URL: <https://linkinghub.elsevier.com/retrieve/pii/S0021999117308306>, doi:10.1016/j.jcp.2017.11.003.
- [92] Angiolo Farina and Lorenzo Fusi. Viscoplastic Fluids: Mathematical Modeling and Applications. pages 229–298. 2018. URL: http://link.springer.com/10.1007/978-3-319-74796-5_5https://link.springer.com/chapter/10.1007/978-3-319-74796-5_5#citeas, doi:10.1007/978-3-319-74796-5_5.
- [93] Pradeep P. Phulé. Magnetorheological (MR) fluids: Principles and applications. *Smart Materials Bulletin*, 2001(2):7–10, feb 2001. URL: <https://linkinghub.elsevier.com/retrieve/pii/S147139180180040X>, doi:10.1016/S1471-3918(01)80040-X.
- [94] Bong Jun Park, Fei Fei Fang, and Hyoung Jin Choi. Magnetorheology: materials and application. *Soft Matter*, 6(21):5246, 2010. URL: <https://xlink.rsc.org/?DOI=c0sm00014k>, doi:10.1039/c0sm00014k.
- [95] Peter J. Rankin, Andrew T. Horvath, and Daniel J. Klingenberg. Magnetorheology in viscoplastic media. *Rheologica Acta*, 38(5):471–477, nov 1999. URL: <http://link.springer.com/10.1007/s003970050198>, doi:10.1007/s003970050198.
- [96] Norman J. Wagner and John F. Brady. Shear thickening in colloidal dispersions. *Physics Today*, 62(10):27–32, oct 2009. URL: <https://pubs.aip.org/physicstoday/article/62/10/27/1017218/Shear-thickening-in-colloidal-dispersionsShampoos>, doi:10.1063/1.3248476.
- [97] Verónica L. Mucci, María E. V. Hormaiztegui, Javier I. Amalvy, and Mirta I. Aranguren. Formulation, structure and properties of waterborne polyurethane coatings: a brief review. *Journal of Adhesion Science and Technology*, 38(4):489–516, feb 2024. URL: <https://www.tandfonline.com/doi/full/10.1080/01694243.2023.2240587>, doi:10.1080/01694243.2023.2240587.

Bibliography

- [98] Chiara F. Ferraris. Measurement of the rheological properties of high performance concrete: State of the art report. *Journal of Research of the National Institute of Standards and Technology*, 104(5):461, sep 1999. URL: <https://nvlpubs.nist.gov/nistpubs/jres/104/5/j45fer.pdf>, doi:10.6028/jres.104.028.
- [99] Kennedy C. Onyelowe and Denise-Penelope N. Kontoni. A critical review of rheological models in self-compacting concrete for sustainable structures. *Scientific Reports*, 13(1):21296, dec 2023. URL: <https://www.nature.com/articles/s41598-023-48673-6>, doi:10.1038/s41598-023-48673-6.
- [100] Yan Peng, Bing Hai Lv, Ju Long Yuan, Hong Bo Ji, Lei Sun, and Chen Chen Dong. Application and Prospect of the Non-Newtonian Fluid in Industrial Field. *Materials Science Forum*, 770:396–401, oct 2013. URL: <https://www.scientific.net/MSF.770.396>, doi:10.4028/www.scientific.net/MSF.770.396.
- [101] M. Kawata, A. Okamoto, T. Endo, and Y. Tsukamoto. Viscoelasticity of synovial fluids and additive effect of hyaluronate. In *Hydrocolloids*, pages 343–348. Elsevier, 2000. URL: <https://linkinghub.elsevier.com/retrieve/pii/B9780444501783501049>, doi:10.1016/B978-044450178-3/50104-9.
- [102] Markus Brillinger and Kevin Ayrton Pendl. Non Newtonian material behaviour in extrusion-based 3D printing: Investigation of critical process parameters. aug 2020. URL: https://avestia.com/MCM2020{}_Proceedings/files/paper/MMME/MMME{}_117.pdf, doi:10.11159/mmme20.117.
- [103] Ming Yan and Hani A. Awad. Optimizing rheological properties for printability: low-temperature extrusion 3D printing of hydroxyapatite-polycaprolactone mixture inks for bone tissue engineering. *Frontiers in Materials*, 10, aug 2023. URL: <https://www.frontiersin.org/articles/10.3389/fmats.2023.1239692/full>, doi:10.3389/fmats.2023.1239692.
- [104] Raúl Sánchez-Sánchez, Jesús M. Rodríguez-Rego, Antonio Macías-García, Laura Mendoza-Cerezo, and Antonio Díaz-Parralejo. Relationship between shear-thinning rheological properties of bioinks and bioprinting parameters. *International Journal of Bioprinting*, 9(2):687, feb 2023. URL: <https://accscience.com/journal/IJB/9/2/10.18063/ijb.687>, doi:10.18063/ijb.687.
- [105] Mohammadreza Mahmoudi, Scott R. Burlison, Salvador Moreno, and Majid Minary-Jolandan. Additive-Free and Support-Free 3D Printing of Thermosetting Polymers with Isotropic Mechanical Properties. *ACS Applied Materials & Interfaces*, 13(4):5529–5538, feb 2021. URL: <https://pubs.acs.org/doi/10.1021/acsmi.0c19608>, doi:10.1021/acsmi.0c19608.
- [106] Abbas Tcharkhtchi, Reza Eslami Farsani, and Hamid Reza Vanaei. Printing

Bibliography

- Optimization: Importance of Rheological Evaluation in 3D Printing. In *Industrial Strategies and Solutions for 3D Printing*, pages 171–192. Wiley, may 2024. URL: <https://onlinelibrary.wiley.com/doi/10.1002/9781394150335.ch9>, doi:10.1002/9781394150335.ch9.
- [107] Berk Uysal, Ujith S. K. Madduma-Bandarage, Hasani G. Jayasinghe, and Sundar Madihally. 3D-Printed Hydrogels from Natural Polymers for Biomedical Applications: Conventional Fabrication Methods, Current Developments, Advantages, and Challenges. *Gels*, 11(3):192, mar 2025. URL: <https://www.mdpi.com/2310-2861/11/3/192>, doi:10.3390/gels11030192.
- [108] Nickolas D. Polychronopoulos and Angeliki Brouzgou. Direct Ink Writing for Electrochemical Device Fabrication: A Review of 3D-Printed Electrodes and Ink Rheology. *Catalysts*, 14(2):110, jan 2024. URL: <https://www.mdpi.com/2073-4344/14/2/110>, doi:10.3390/catal14020110.
- [109] Mohammad Hassan Amiri, Ahmad Keshavarzi, Arash Karimipour, Mehdi Bahiraei, Marjan Goodarzi, and J A Esfahani. A 3-D numerical simulation of non-Newtonian blood flow through femoral artery bifurcation with a moderate arteriosclerosis: investigating Newtonian/non-Newtonian flow and its effects on elastic vessel walls. *Heat and Mass Transfer*, 55(7):2037–2047, 2019. doi:10.1007/s00231-019-02583-4.
- [110] Antony N. Beris, Jeffrey S. Horner, Soham Jariwala, Matthew J. Armstrong, and Norman J. Wagner. Recent advances in blood rheology: a review. *Soft Matter*, 17(47):10591–10613, 2021. URL: <https://xlink.rsc.org/?DOI=D1SM01212F>, doi:10.1039/D1SM01212F.
- [111] Konstantinos Giannokostas, Pantelis Moschopoulos, Stylianos Varchanis, Yannis Dimakopoulos, and John Tsamopoulos. Advanced Constitutive Modeling of the Thixotropic Elasto-Visco-Plastic Behavior of Blood: Description of the Model and Rheological Predictions. *Materials*, 13(18):4184, sep 2020. URL: <https://www.mdpi.com/1996-1944/13/18/4184>, doi:10.3390/ma13184184.
- [112] A Abbas Nejad, Z Talebi, D Cheraghali, A Shahbani-Zahiri, and M Norouzi. Pulsatile flow of non-Newtonian blood fluid inside stenosed arteries: Investigating the effects of viscoelastic and elastic walls, arteriosclerosis, and polycythemia diseases. *Computer Methods and Programs in Biomedicine*, 154:109–122, 2018. URL: <https://www.sciencedirect.com/science/article/pii/S0169260716313888>, doi:10.1016/j.cmpb.2017.11.016.
- [113] Yonghui Qiao, Yujie Zeng, Ying Ding, Jianren Fan, Kun Luo, and Ting Zhu. Numerical simulation of two-phase non-Newtonian blood flow with fluid-structure

Bibliography

- interaction in aortic dissection. *Computer Methods in Biomechanics and Biomedical Engineering*, 22:620–630, 2019.
- [114] Alexander Y. Hui, William J. McCarty, Koichi Masuda, Gary S. Firestein, and Robert L. Sah. A systems biology approach to synovial joint lubrication in health, injury, and disease. *WIREs Systems Biology and Medicine*, 4(1):15–37, jan 2012. URL: <https://wires.onlinelibrary.wiley.com/doi/10.1002/wsbm.157>, doi:10.1002/wsbm.157.
- [115] Haiqing Liu, Kunkun Fu, Xiaoyu Cui, Huixin Zhu, and Bin Yang. Shear Thickening Fluid and Its Application in Impact Protection: A Review. *Polymers*, 15(10):2238, may 2023. URL: <https://www.mdpi.com/2073-4360/15/10/2238>, doi:10.3390/polym15102238.
- [116] James A. Richards, Daniel J. M. Hodgson, Rory E. O’Neill, Michael E. DeRosa, and Wilson C. K. Poon. Optimizing non-Newtonian fluids for impact protection of laminates. *Proceedings of the National Academy of Sciences*, 121(10), mar 2024. URL: <https://pnas.org/doi/10.1073/pnas.2317832121>, doi:10.1073/pnas.2317832121.
- [117] Juan de Vicente, Daniel J. Klingenberg, and Roque Hidalgo-Alvarez. Magnetorheological fluids: a review. *Soft Matter*, 7(8):3701, 2011. URL: <https://xlink.rsc.org/?DOI=c0sm01221a>, doi:10.1039/c0sm01221a.
- [118] Jong-Seok Oh, Jung Woo Sohn, and Seung-Bok Choi. Applications of Magnetorheological Fluid Actuator to Multi-DOF Systems: State-of-the-Art from 2015 to 2021. *Actuators*, 11(2):44, feb 2022. URL: <https://www.mdpi.com/2076-0825/11/2/44>, doi:10.3390/act11020044.
- [119] Laurent Chupin. Global Strong Solutions for Some Differential Viscoelastic Models. *SIAM Journal on Applied Mathematics*, 78(6):2919–2949, jan 2018. doi:10.1137/18M1186873.
- [120] Marshall J Leitman and George M C Fisher. The linear theory of viscoelasticity(Constitutive equations, creep laws, stress functions, variational principles and differential operators in dynamic and static linear viscoelasticity theory). *Solid-state mechanics 3.(A 73-45495 24-32) Berlin, Springer-Verlag, 1973,*, pages 1–123, 1973.
- [121] T C B McLeish and R G Larson. Molecular constitutive equations for a class of branched polymers: The pom-pom polymer. *Journal of Rheology*, 42(1):81, 1998.
- [122] N J Inkson, T G B McLeish, O G Harlen, and D J Groves. Predicting low density polyethylene melt rheology in elongational and shear flows

Bibliography

- with pom-pom constitutive equations. *Journal of Rheology*, 43(4):873–896, 1999. URL: <https://www.scopus.com/inward/record.uri?eid=2-s2.0-0000759154&doi=10.1122/1.551036&partnerID=40&md5=8b539195d73e37d9ae0950a056a75192>, doi:10.1122/1.551036.
- [123] William D. Henshaw and N. Anders Petersson. A Split-Step Scheme for the Incompressible Navier-Stokes Equations. In *Numerical Simulations of Incompressible Flows*, pages 108–125. WORLD SCIENTIFIC, Half Moon Bay, CA, jan 2003. doi:10.1142/9789812796837_0007.
- [124] A.W. Vreman. The projection method for the incompressible Navier-Stokes equations: The pressure near a no-slip wall. *Journal of Computational Physics*, 263:353–374, apr 2014. doi:10.1016/j.jcp.2014.01.035.
- [125] Douglas R. Q. Pacheco and Ernesto Castillo. Consistent splitting schemes for incompressible viscoelastic flow problems. *International Journal for Numerical Methods in Engineering*, 124(8):1908–1927, apr 2023. URL: <https://onlinelibrary.wiley.com/doi/10.1002/nme.7192>, doi:10.1002/nme.7192.
- [126] Manish Kumar, Jeffrey S. Guasto, and Arezoo M. Ardekani. Lagrangian stretching reveals stress topology in viscoelastic flows. *Proceedings of the National Academy of Sciences*, 120(5), jan 2023. URL: <https://pnas.org/doi/10.1073/pnas.2211347120>, doi:10.1073/pnas.2211347120.
- [127] Pratik Suchde and Joerg Kuhnert. Point Cloud Movement For Fully Lagrangian Meshfree Methods. *arXiv*, 1704.00618:12, apr 2017. arXiv:1704.00618, doi:10.1016/j.cam.2018.02.020.
- [128] Miles Macklin and Matthias Müller. Position based fluids. *ACM Transactions on Graphics*, 32(4):1, 2013. doi:10.1145/2461912.2461984.
- [129] Jean Paul Vila. On Particle Weighted Methods and Smooth Particle Hydrodynamics. *Mathematical Models and Methods in Applied Sciences*, 09(02):161–209, 1999. doi:10.1142/S0218202599000117.
- [130] Odus R Burggraf. Analytical and numerical studies of the structure of steady separated flows. *Journal of Fluid Mechanics*, 24(1):113–151, jan 1966. URL: https://www.cambridge.org/core/product/identifier/S0022112066000545/type/journal_article, doi:10.1017/S0022112066000545.
- [131] I Demirdžić, Lilek, and M Perić. Fluid flow and heat transfer test problems for non-orthogonal grids: Bench-mark solutions. *International Journal for Numerical Methods in Fluids*, 1992. doi:10.1002/flid.1650150306.
- [132] Sharaban Thohura, Md. Mamun Molla, and Md. Manirul Alam Sarker. Numerical Simulation of Non-Newtonian Power-Law Fluid Flow in a Lid-Driven

Bibliography

- Skewed Cavity. *International Journal of Applied and Computational Mathematics*, 5(1):14, feb 2019. URL: <http://link.springer.com/10.1007/s40819-018-0590-y>, doi:10.1007/s40819-018-0590-y.
- [133] D Komatina and M Jovanović. Experimental study of steady and unsteady free surface flows with water-clay mixtures. *Journal of Hydraulic Research*, 1997. doi:10.1080/00221689709498395.
- [134] N Roussel and P Coussot. “Fifty-cent rheometer” for yield stress measurements: From slump to spreading flow. *Journal of Rheology*, 49(3):705–718, may 2005. URL: <http://sor.scitation.org/doi/10.1122/1.1879041>, doi:10.1122/1.1879041.
- [135] Guido Dhondt. *The Finite Element Method for Three-Dimensional Thermomechanical Applications*. John Wiley & Sons, Ltd, Chichester, UK, may 2004. URL: <http://doi.wiley.com/10.1002/0470021217>, doi:10.1002/0470021217.
- [136] Hans-Joachim Joachim Bungartz, Florian Lindner, Bernhard Gatzhammer, Miriam Mehl, Klaudius Scheufele, Alexander Shukaev, and Benjamin Uekermann. preCICE – A fully parallel library for multi-physics surface coupling. *Computers & Fluids*, 141:250–258, dec 2016. URL: <https://linkinghub.elsevier.com/retrieve/pii/S0045793016300974>, arXiv:0402594v3, doi:10.1016/j.compfluid.2016.04.003.
- [137] Carla Antoci, Mario Gallati, and Stefano Sibilla. Numerical simulation of fluid–structure interaction by SPH. *Computers & Structures*, 85(11-14):879–890, jun 2007. URL: <https://linkinghub.elsevier.com/retrieve/pii/S0045794907000132>, doi:10.1016/j.compstruc.2007.01.002.
- [138] R. G. Sousa, R. J. Poole, A. M. Afonso, F. T. Pinho, P. J. Oliveira, A. Morozov, and M. A. Alves. Lid-driven cavity flow of viscoelastic liquids. *Journal of Non-Newtonian Fluid Mechanics*, 234:129–138, aug 2016. doi:10.1016/j.jnnfm.2016.03.001.
- [139] Cuong Mai Bui, Anh-Ngoc Tran Ho, and Xuan Bao Nguyen. Flow Behaviors of Polymer Solution in a Lid-Driven Cavity. *Polymers*, 14(12), 2022. URL: <https://www.mdpi.com/2073-4360/14/12/2330>, doi:10.3390/polym14122330.
- [140] Omar Mokhtari, Yohan Davit, Jean-Claude Latché, and Michel Quintard. A staggered projection scheme for viscoelastic flows. *ESAIM: Mathematical Modelling and Numerical Analysis*, 57(3):1747–1793, may 2023. doi:10.1051/m2an/2023020.
- [141] Michael Renardy. A comment on smoothness of viscoelastic stresses. *Journal of Non-Newtonian Fluid Mechanics*, 138(2-3):204–205, oct 2006. doi:10.1016/j.jnnfm.2006.05.006.

Bibliography

- [142] R A Figueiredo, C M Oishi, A M Afonso, I V M Tasso, and J A Cuminato. A two-phase solver for complex fluids: Studies of the Weissenberg effect. *International Journal of Multiphase Flow*, 84:98–115, 2016. URL: <http://dx.doi.org/10.1016/j.ijmultiphaseflow.2016.04.014>, doi:10.1016/j.ijmultiphaseflow.2016.04.014.
- [143] Wei Wang and Linlin Wang. An Experimental Investigation of Viscoelastic Flow in a Contraction Channel. *Polymers*, 13(11):1876, jun 2021. URL: <https://www.mdpi.com/2073-4360/13/11/1876>, doi:10.3390/polym13111876.
- [144] Laura Moreno, Ramon Codina, Joan Baiges, and Ernesto Castillo. Logarithmic conformation reformulation in viscoelastic flow problems approximated by a VMS-type stabilized finite element formulation. *Computer Methods in Applied Mechanics and Engineering*, 354:706–731, sep 2019. URL: <https://linkinghub.elsevier.com/retrieve/pii/S0045782519303330>, doi:10.1016/j.cma.2019.06.001.
- [145] A. M. Afonso, P. J. Oliveira, F. T. Pinho, and M. A. Alves. Dynamics of high-Deborah-number entry flows: a numerical study. *Journal of Fluid Mechanics*, 677:272–304, jun 2011. doi:10.1017/jfm.2011.84.
- [146] Stefan Wittschieber, Leszek Demkowicz, and Marek Behr. Stabilized finite element methods for a fully-implicit logarithmic reformulation of the Oldroyd-B constitutive law. *Journal of Non-Newtonian Fluid Mechanics*, 306:104838, aug 2022. URL: <https://linkinghub.elsevier.com/retrieve/pii/S0377025722000763>, doi:10.1016/j.jnnfm.2022.104838.
- [147] M. Niethammer, H. Marschall, C. Kunkelmann, and D. Bothe. A numerical stabilization framework for viscoelastic fluid flow using the finite volume method on general unstructured meshes. *International Journal for Numerical Methods in Fluids*, 86(2):131–166, jan 2018. URL: <https://onlinelibrary.wiley.com/doi/10.1002/fld.4411>, doi:10.1002/fld.4411.
- [148] Milad Mousavi, Yannis Dimakopoulos, and John Tsamopoulos. Elasto-visco-plastic flows in benchmark geometries: I. 4 to 1 planar contraction. *Journal of Non-Newtonian Fluid Mechanics*, 327:105218, may 2024. URL: <https://linkinghub.elsevier.com/retrieve/pii/S037702572400034X>, doi:10.1016/j.jnnfm.2024.105218.
- [149] Soroush Hooshyar and Natalie Germann. Shear Banding in 4:1 Planar Contraction. *Polymers*, 11(3):417, mar 2019. URL: <https://www.mdpi.com/2073-4360/11/3/417>, doi:10.3390/polym11030417.
- [150] Raphaël Comminal, Francisco Pimenta, Jesper H. Hattel, Manuel A. Alves, and Jon Spangenberg. Numerical simulation of the planar extrudate

Bibliography

swell of pseudoplastic and viscoelastic fluids with the streamfunction and the VOF methods. *Journal of Non-Newtonian Fluid Mechanics*, 252:1–18, feb 2018. URL: <https://linkinghub.elsevier.com/retrieve/pii/S0377025717304883>, doi:10.1016/j.jnnfm.2017.12.005.

Životopis

Martina Bašić je zaposlena kao asistentica na Zavodu za strojarstvo i brodogradnju FESB-a, Sveučilišta u Splitu, gdje uz edukaciju studenata, aktivno sudjeluje na znanstveno-istraživačkim projektima i konferencijama.

Nakon stjecanja diplome prvostupnice (2012.–2016.) i magisterija inženjerke brodogradnje (2016.–2018.) na FESB-u, 2019. upisuje doktorski studij strojarstva. Tijekom dokorskog studija sudjelovala je u niz projekata: kao istraživačica na ERDF projektu „IRA 3 – Inovativno rješenje vodomlaznog propulzora“ (2020.–2023.), bila je koordinatorica Interreg projekta „Tradicionalna brodogradnja Tkona“ (2021.), te sudjeluje u Institucionalnom projektu o hidrodinamičkoj izvedbi autonomnih SWATH plovila. Također je suradnica u Centru kompetencija za naprednu mobilnost.

Posebno je aktivna na međunarodnim konferencijama: 2018. je izabrana za predavačicu na NUMECA User Meeting, a sudjeluje i na ISOPE 2019 (Honolulu, Hawaii), na kojem je prezentirala rad “An Analysis of the Ventilated Flow on a Rudder”. Godine 2021. autorica je rada “Coupling of non-Newtonian Meshless Flow with Structural Solvers” na VII International Conference on Particle-Based Methods u Hamburgu. Na PARTICLES 2023 konferenciji ponavlja suradnju u CFD-DEM studiji viskozni tokova. Pored znanstvenih radova, aktivno je sudjelovala u organizaciji stručnih skupova, primjerice kao suorganizatorica 23. simpozija „Teorija i praksa brodogradnje“ (SORTA2018). Članica je Društva inženjera brodogradnje Split od 2018. godine.

Curriculum Vitae

Martina Bašić is employed as a teaching and research assistant at the Department of Mechanical Engineering and Naval Architecture at the University of Split, Faculty of Electrical Engineering, Mechanical Engineering and Naval Architecture (FESB). In addition to her involvement in student education, she actively participates in scientific research projects and international conferences.

After completing her undergraduate studies in naval architecture (2012–2016) and obtaining a master’s degree in the same field (2016–2018) at FESB, she enrolled in the doctoral program in Mechanical Engineering in 2019. During her doctoral studies, she was involved in several projects, including work as a researcher on the ERDF-funded project “IRA 3 – Innovative Solution for a Water Jet Propulsor” (2020–2023), and served as coordinator of the Interreg project “Traditional Shipbuilding of Tkon” (2021). She is also participating in the institutional project focused on the hydrodynamic performance of autonomous SWATH vessels, and is a collaborator in the Competence Center for Advanced Mobility.

She is particularly active at international scientific conferences. In 2018, she was selected as an invited speaker at the NUMECA User Meeting, and in 2019 she participated in the ISOPE Conference in Honolulu, Hawaii, where she presented the paper “An Analysis of the Ventilated Flow on a Rudder.” In 2021, she presented “Coupling of Non-Newtonian Meshless Flow with Structural Solvers” at the VII International Conference on Particle-Based Methods in Hamburg. In 2023, she continued her work in CFD-DEM simulation of viscous flows at the PARTICLES 2023 conference. In addition to scientific work, she has contributed to the organization of professional events, including co-organization of the 23rd Symposium on Theory and Practice of Shipbuilding (SORTA2018). She has been a member of the Association of Naval Architects Split since 2018.